Numerical Examination of Non-Equilibrium Condensation in Supersonic Micronozzles

Angelos Karagiannis

Master of Science Thesis 2020

TECHNISCHE UNIVERSITEIT DELFT

FACULTEIT LUCHTVAART- EN RUIMTEVAART TECHNIEK

PAGE LEFT BLANK

Numerical Examination of Non-Equilibrium Condensation in Supersonic Micronozzles

by

Angelos Karagiannis

in partial fulfillment of the requirements for obtaining the degree of
Master of Science in Aerospace Engineering (Space Flight)
at the Delft University of Technology,
to be defended publicly on July 21, 2020 at 09:30.

Student number	4280164	
Thesis committee:	Assoc. Prof. dr. J. Guo	TU Delft, Committee chair
	Asst. Prof. dr. A. Cervone	TU Delft, Daily supervisor
	Asst. Prof. dr. M. Pini	TU Delft, External examiner

An electronic version of this thesis is available at: http://repository.tudelft.nl/.

TU Delft

Summary

The Micropropulsion Group of the department of Space Systems Engineering of the Delft University of Technology is developing resistojet thrusters for small satellites operating on the vapourisation of liquid water via an electric heater and its subsequent expansion via a nozzle into vacuum for the generation of thrust. As the water vapour expands in the nozzle, its pressure and temperature drop, leading it to cross the saturation limit of water and raising questions on whether the vapour will transition back to liquid in the nozzle's divergent section. The spontaneous condensation of flowing steam in supersonic nozzles is a well-known phenomenon that results in the release of heat, in turn downgrading the nozzle's performance and efficiency.

This has motivated the present numerical study to assess the likelihood of the phenomenon's occurence inside the resistojet micronozzles. To that end, a condensation model is implented in the open-source platform OpenFOAM, by heavily modifying an existing compressible solver to account for the mild degrees of rarefaction in the nozzle, the real-gas thermodynamics of water and the phase-change phenomenon itself. The condensation is modelled as a two-step process, whereby liquid clusters first nucleate out of the vapour and then proceed to grow by gathering further vapor molecules. A baseline micronozzle case is defined as one with a 100 µm-depth nozzle with an expansion angle of 30 deg and stagnation pressure and temperature of 3 bar and 473 K. The simulations are run for three stagnation pressures (1, 3 and 5 bar), three stagnation temperatures (473, 573 and 673 K), three expander angles (15, 30, 45 degrees) and two nozzle depths (100 and 200 µm). The outputs are in each case compared to the baseline case, to extract conclusions on the effect of nozzle geometric and flow topological features on the occurence of condensation.

The results show that the onset of condensation is in most instances a likely scenario, but not necessarily a consequential one. The extremely fast cooling rates (10^8-10^9 K s^{-1}) drive the vapour to unusual degrees of supersaturation (10^3 or more) before condensation occurs. When the birth of droplets eventually takes place, it does so in impulsive fashion, with large numbers of miniscule liquid clusters (radii in the order of 10^{-10} m) appearing simultaneously in mass fractions in the vicinity of 2%. Even so, the macroscopic result is typically small, with the thrust and specific impulse changing only by 1-2% at most. This holds true for the variation of all above design parameters except for the nozzle depth: it is shown that doubling the depth decreases the wall's heat influence and leaves room for substantial condensation to occur, that degrades the thrust output by more than 5%.

The general conclusion to be drawn is that assessing the impact of condensation on this type of nozzles is not as straightforward as in their conventional-scale counterparts and it is difficult to note consistent trends. If it does occur, the condensation process will enter a complex interaction mechanism with the heat supplied from the walls, the viscous layers developing on these walls and the degree to which the expansion can overcome either or both. While in conventional scale nozzles the occurence of the phenomenon typically guarantees a reduction in thrust and efficiency, here there is no general tendency and the nature of the influence depends on the extent to which the release of latent heat and its by-products can match in severity the rest of the phenomena inside the micronozzles. Overall, the analysis indicated that the geometric configuration of a 100 µm-deep thruster with a 30-deg expander angle strikes a good balance in generally avoiding the occurence of substantial phase change (that would cause a $\geq 2\%$ change in macroscopic performance metrics) and also containing other contributing effects, such as the growth of viscous layers and expansion losses. The choice of stagnation conditions is mission-dependent and no recommendation can be given, but some suggestions are provided on approximate methods to select them such that condensation is avoided.

Acknowledgements

A number of people have offered much appreciated help during the compilation of this work and owe to be acknowledged.

First and foremost, I extend my gratitude to my direct supervisor, Assistant professor Dr. Angelo Cervone, for allowing me full freedom in the selection of the thesis topic and the realisation of this work, which gave me the room to explore various aspects of the subject and extend my knowledge in the field. I appreciate his maintaining a watchful eye over this work, promptly and eagerly providing me with resources whenever needed and offering his feedback and thorough examination on this document.

Special thanks go to the following scientists for providing me with valuable validation-relevant data that I would not otherwise have been able to access: Dr. Matteo Pini, researcher at the department of Flight Performance and Propulsion at the University of Delft in the Netherlands; Dr. Barbara Wyzlousil, Professor in physical chemistry at the Ohio State University in the United States; and Dr. Alexandra Manka, formerly at the University of Cologne in Germany.

The following individuals generously provided me with computational tools of their making, at the early stages of this work. While these tools have not eventually found implementation here, they provided me with useful insights into sound practices of numerical analysis, programming in the C++ language and on development in the OpenFOAM software, at a time when I was a complete beginner in these aspects: Dr. Davide Modesti, at the time a researcher in the Sapienza University of Rome; Dr. Giuseppe LaSpina, at the time a researcher at the University of Pisa; and Associate Professor Kokou Dadzie of the Heriot-Watt University.

Returning to TU Delft, I would further like to acknowledge Assistant professor Dr. Ferdinand Schrijer and lecturer Barry Zandbergen for discussions on experimental techniques and other related matters in the early stages of this work, that helped decide to focus it exclusively on numerical investigations instead. In a private communication, former student Luca Denies suggested a useful partial solution for resolving numerical difficulties with the single-phase model of this work. And current PhD candidate Ms. Fiona Leveronne has kindly accommodated me in her working space for an extended period of time. Lastly, I thank my fellow students Bas Krijnen, Stijn Koehler, Peter van der Berg, Jorgis Theodoulou and Julius Weinmiller for occasional, but useful discussions.

On a more personal tone, I owe my gratitude to my partner Michaela for offering love and bearing with me through countless moments of frustration during the realisation of this work. And, of course, I am forever indebted to my parents, Panagiotis and Eleni, whose continuous sacrifices and unwavering support during the last few years have made it possible for me to study the subject that is my passion in such a quality university. To them I owe everything.

Angelos Karagiannis
Delft, the Netherlands
July 2020

Contents

Summary i

List of Symbols iv

List of Abbreviations iv

List of Figures iv

List of Tables iv

1 Introduction 1

2 The problem in context 2
2.1 General . . . 2
2.2 Micropropulsion research at TU Delft . . . 2
2.3 Brief review of gas dynamics in low density micronozzles . . . 3
2.4 Two-phase flow in VLM nozzles . . . 4
2.5 Water vapour condensation in supersonic nozzles . . . 5
2.6 Scope of this work . . . 10

I Single-phase model 12

3 Single-phase model 13
3.1 Modelling approach . . . 13
3.2 The governing equations . . . 14
3.3 The numerical solver . . . 16
3.4 Short-comings of the governing equations in rarefied flows . . . 16
3.5 Validation of the single-phase model . . . 20

II Thermodynamics of water 26

4 Thermodynamic properties of (supercooled) steam and water 27
4.1 Preliminary remarks . . . 27
4.2 Basic equation of state . . . 28
4.3 Vapour thermodynamic properties . . . 30
4.4 Vapour transport properties . . . 32
4.5 Saturation properties . . . 34
4.6 Liquid phase properties . . . 36
4.7 Interim recap . . . 37
4.8 Thermophysical properties below 273 Kelvin . . . 38
4.9 Numerical implementation . . . 45
4.10 Freezing of droplets . . . 45
4.11 Summary of the thermodynamic model . . . 46

III Two-phase model **48**

5 Two-phase model **49**
5.1 Basic principles . . . 49
5.2 Assumptions . . . 51
5.3 Droplet nucleation model . . . 52
5.4 Droplet growth model . . . 59
5.5 Inertial influence of the droplets on the flow . . . 62
5.6 Inclusion of the second phase in the conservation equations . . . 63
5.7 Numerical implementation . . . 64
5.8 Algorithmic summary of the model . . . 66
5.9 Validation of the two-phase model . . . 67

IV Numerical setup and results **74**

6 Preparation of the simulations **75**
6.1 Geometry . . . 75
6.2 Control variables and baseline configuration . . . 77
6.3 Estimates of macroscopic performance . . . 78
6.4 Numerical setup . . . 80
6.5 Initialisation of the solution . . . 83

7 Results and discussion **85**
7.1 Effect of stagnation pressure . . . 86
7.2 Effect of stagnation temperature . . . 92
7.3 Effect of expander angle . . . 99
7.4 Effect of nozzle depth . . . 103
7.5 Summary of macroscopic performance . . . 108

V Conclusions and Recommendations **109**

8 Conclusions **110**

9 Recommendations for future work **113**

Bibliography **115**

List of Figures

2.1 Samples of microthrusters fabricated at the Delft University of Technology . . . 3
2.2 Schlieren visualisation of the shock-like structure of the condensation front in a supersonic wind-tunnel nozzle . . . 7
2.3 Schematic of a typical condensation process in a supersonic nozzle . . . 7
2.4 Phase diagram of water . . . 8

3.1 Infinitesimal control volume for the derivation of the Navier-Stokes equations . . . 15
3.2 Visual interpretation of the Navier slip length . . . 18
3.3 Geometry of the nozzle of Rothe (1971) . . . 22
3.4 Computational mesh of the nozzle of Rothe (1971) . . . 22
3.5 Comparison of the single-phase model against the experiments of Rothe (1971) . . . 23
3.6 Geometry and computational mesh of the nozzle of Cen and Xu (2010) . . . 24

4.1 Variation of the the ideal water vapour specific heat with temperature . . . 39
4.2 Vapour viscosity model for temperatures below the triple point . . . 40
4.3 Variation of latent heat of supercooled water with temperature . . . 43
4.4 Comparison of common models for the surface tension of supercooled liquid water with selected experimental datasets . . . 44

5.1 Variation of ΔG with droplet radius for supersaturated vapour . . . 53
5.2 Example of the temporal evolution of the transient nucleation phase . . . 56
5.3 Schematic of neighbouring control volumes in the computational domain. . . . 64
5.4 Geometries of the nozzles of Moore et al. (1973), as shown in the original publication . . . 68
5.5 Validation of the two-phase model against the experiments of Moore et al. (1973) . . . 70
5.6 Evolution of condensation parameters along the centerline for Nozzle B of Moore et al. (1973) . . . 72
5.7 Evolution of flow parameters along the centerline for Nozzle B of Moore et al. (1973) . . . 73

6.1 Geometric features of the micronozzles treated in this work . . . 75
6.2 Overview of the computational domain . . . 76
6.3 Overview of the computational domain boundaries . . . 76
6.4 Comparison of Knudsen number fields between the nozzle of Rothe (1971) and one of the micronozzle flow cases . . . 79

7.1 Comparison of the flowfield for the 5 bar case with and without the effect of condensation . . . 87
7.2 Horizontal velocity isolines for the 5 bar case . . . 88
7.3 Isolines of Mach number and temperature at pressures of 1-5 bar . . . 89
7.4 Isolines of supersaturation ratios and nucleation rates at pressures of 1-5 bar . . . 90
7.5 Isolines of liquid mass fractions and droplet radii at pressures of 1-5 bar . . . 91
7.6 Variation of the water vapour saturation pressure with the local temperature, for $T \leq 273\,\mathrm{K}$ . . . 93
7.7 Variation with exit Mach number of the minimum stagnation temperature required to avoid supersaturation in the nozzle . . . 95
7.8 Isolines of Mach number and temperature at stagnation temperatures of 473-673 K . . . 97
7.9 Isolines of supersaturation ratios and nucleation rates at stagnation temperatures of 473-673 K . 98
7.10 Isolines of liquid mass fractions and droplet radii at stagnation temperatures of 473-673 K . . . 98
7.11 Isolines of Mach number and temperature at expander angles of 15-45 deg . . . 100
7.12 Isolines of supersaturation ratios and nucleation rates at expander angles of 15-45 deg . . . 101
7.13 Isolines of liquid mass fractions and droplet radii at expander angles of 15-45 deg . . . 102
7.14 Isolines of liquid mass fractions and droplet radii at nozzle depths of 100-200 µm . . . 105
7.15 Isolines of liquid mass fractions and droplet radii at nozzle depths of 100-200 µm . . . 105

7.16 Comparison of a selection of properties between the cases with and without condensation along the nozzle exit cross-section of the 200 µm-deep micronozzle 106
7.17 Flow properties for the 200 µm-deep nozzle along the centerline 107

List of Symbols

Latin characters

Symbol	Description	Unit
A	Surface area	m^2
	Accommodation factor	[–]
A_s	Sutherland viscosity	$Pa \cdot s$
B	Reynolds number based on stagnation conditions	[–]
B_x	Virial coefficient	[–]
C_g	Speed of sound in gas	m/s
C_p	Isobaric specific heat capacity	J/kg
C_v	Isochoric specific heat capacity	J/kg
E	Total energy	J
F	Force	N
G	Gibbs free energy	J
	Empirical Virial constant	[–]
H	Total enthalpy	[–]
I	Identity matrix	[–]
I_{sp}	Specific impulse	[s]
J	Number of droplets nucleated per unit volume of gas per second	$[\#/(m^3 \cdot s)]$
Kn	Knudsen number	[–]
L	Characteristic length of the flow	m
	Latent heat	J/kg
M	Mach number	[–]
M_{molar}	Molar mass	[kg/mol]
N	Number of droplets per unit mass of gas	[#/kg]
P	Pressure	Pa
Pr	Prandtl number	[–]
R	Specific gas constant	$J/(kg \cdot K)$
$\mathbf{S}$	Tensorial operator	[–]
S	Entropy	J/K
	Saturation ratio	[–]
S_X	Source term in a conservation equation	[–]
T	Temperature	K
T_s	Sutherland temperature	K
U	Velocity magnitude	m/s
	Internal energy	J
V	Volume	m^3
$\mathbf{v}$	Velocity vector	m/s
Y	Liquid-to-gas mass fraction	[–]
Z	Compressibility factor	[–]
b	Empirical Virial constant	[–]
d	Diameter	m
e	Internal energy	J
	Empirical Virial constant	[–]
f_g	Concentration of liquid clusters consisting of g molecules	$\#/m^3$
g	Number of molecules in liquid cluster	[–]
h	Specific enthalpy	J/kg

k	Thermal conductivity	$\mathrm{W}/(\mathrm{m}\cdot\mathrm{K})$
k_B	Boltzmann constant	$\mathrm{m}^2\mathrm{kgs}^{-2}\mathrm{K}^{-1}$
ln	Natural logarithm	$[-]$
m	Molecular mass	kg
	Mass	kg
m_x	Empirical Virial constant	$[-]$
$\dot{m}$	Mass flow	kg/s
$\mathbf{n}$	Normal vector	$[-]$
n	Concentration of liquid clusters	$\#/\mathrm{m}^3$
$n_{I_{sp}}$	Specific impulse efficiency	$[-]$
p	Pressure	Pa
q_c	Condensation coefficient	$[-]$
q_e	Evaporation coefficient	$[-]$
r	Radius	m
r_c	Critical radius	m
t	Time	s
$tanh$	Hyperbolic tangent of	$[-]$
u	Velocity	s
v	Specific volume	m^3/kg
w_x	Empirical Virial constant	s

Greek characters

Symbol	Description	Unit
Δ	Difference in	$[-]$
α	Thermal diffusivity	$[\mathrm{m}^2/\mathrm{s}]$
α	Empirical coefficient	$[-]$
γ	Ratio of specific heats	$[-]$
η	Kantrowitz correction factor on the nucleation rate	m
λ	Mean free path of gas molecules	m
	Bulk/second/dilational viscosity	$\mathrm{Pa}\cdot\mathrm{s}$
λ_g	Coefficient of convective heat transfer between the gas and a droplet	$\mathrm{W}/(\mathrm{m}^2\cdot\mathrm{K})$
μ	Dynamic viscosity	$\mathrm{Pa}\cdot\mathrm{s}$
π	3.14159...	$-$
ρ	Density	kg/m^3
σ	Accommodation coefficient	$[-]$
	Surface tension	$[\mathrm{N}/\mathrm{m}]$
τ	Shear stress	Pa
	Relaxation time	s
ϕ_x	Empirical Virial constant	$[-]$
x	Coordinate on a right-hand xyz system	m

Subscripts

Symbol	Description
0	Total/stagnation value
M	Momentum
T	Thermal
	Thrust
c	Value at thermodynamic critical point
fg	Difference in value between the gas and the liquid
g	Gas
n	Normal direction
p	Particle/droplet
s	Value at saturation
ss	Value at steady state phase
t	Nozzle throat
tr	Value at transient phase
w	Wall

Superscripts

Symbol	Description
$*$	Nozzle throat condition
	Reference value
0	Determined from old timestep values
	Value at dillute-gas limit
$'$	Linearised term

Special characters

Symbol	Description	Unit
∇	Nabla operator	$[-]$
∂	Partial differential	$[-]$
$\mathcal{R}$	Universal gas constant	$\mathrm{J}/(\mathrm{mol}\cdot\mathrm{K})$
$\mathcal{N}_a$	Avogadro constant	mol^{-1}

List of Abbreviations

Abbreviation	Description
2D/3D	Two-/Three-dimensional
BC	Boundary Condition
CFD	Computational Fluid Dynamics
DRIE	Deep Reactive Ion Etching
DSMC	Direct Simulation Monte Carlo
EoS	Equation of State
FVM	Finite Volume Modelling
IAPWS	International Association for the Properties of Water and Steam
IRT	Ideal Rocket Theory
JANNAF	Joint Army Navy NASA Air Force (of the United States of America)
LPM	Low Pressure Microthruster (or Microresistojet)
MEMS	Micro-Electro-Mechanical Systems
NIST	National Institute of Standards and Technology (of the United States of America)
RQ	Research Question
RQS	Secondary Research Question
TU	Technical University of
VLM	Vapourising Liquid Microthruster (or Microresistojet)

CHAPTER 1

Introduction

The advent of novel fabrication techniques in the world of electronics at the latter stages of the 20th century enabled the production of electronic devices at unprecedentedly minute sizes, with repercussions in virtually every scientific and technological field. In the space engineering sector, it allowed for the production of spacecraft spanning just centimetres along their largest dimension. In doing so, it facilitated progress in concepts long envisioned, that would have conventional spacecraft replaced by fleets of miniaturised architectures, offering the capacity for standardisation, flexibility in performance and reduction in cost. The new size standards have introduced intensive efforts for the reduction of the spacecraft subsystems' sizes to the micro-scale and it is in this context that this work has been carried out.

The focus here is placed on the analysis of the micro-propulsion sub-system, in the framework of ongoing research at the department of Space Systems Engineering at the Technical University of Delft. Among the concepts currently explored is that of a water-fed microresistojet, which vapourises a small quantity of water and subsequently expands it into the ambience to produce thrust. Various aspects of the device's operation have been explored in recent years, but one topic that has received limited attention is the prospect of two-phase flow in the nozzle and its impact on the thruster's performance. In particular, this work centers on the mechanisms by which the expanding steam may condense into liquid water and aims to numerically assess whether this is a likely scenario and, if so, what its influence on the nozzle's performance is. This little-explored issue must be settled before fully informed design decisions on the design of these micronozzles can be made.

The document is structured as follows. Ch. 2 places the problem in context and makes clear why this phenomenon is one worth attention. The mechanisms by which two-phase flow can occur in the nozzle are briefly described and past work on the topic, as found in literature, is reviewed. The basic physics of condensation are presented, along with argumentation on the phenomenon's relevance to the design of micronozzles. In this introductory chapter's last section, the scope of this work is framed, stating the research objective and associated research questions.

From there on, the subsequent three chapters are where the numerical model is developed. Ch. 3 outlines the single phase solver upon which the condensation model is built. Ch. 4 compiles a thermodynamic model capable of estimating the thermophysical properties of water in gaseous and liquid form, as well as in equilibrium and non-equilibrium states. Ch. 5 treats the implementation of the condensation model itself and Ch. 6 explains how the numerical simulations have been set up. Finally, in Ch. 7, the prospect and consequences of condensation is explored for selected represantive points across the operational envelope of the micronozzle, before conclusions on the results are drawn and recommendations are made for future work.

CHAPTER 2

The problem in context

2.1 General

In the context of this work, terms such as ”micropropulsion”, ”microthruster”, ”micronozzle” are used to describe systems aimed at producing thrust in the order-of-magnitude range of 10^{-6}-10^{-3} N. Such devices typically feature minute geometric dimensions in the the order-of-magnitude range of 10^{-6}-10^{-3} m and are built to serve spacecraft of the nano- and pico-satellite scale, commonly featuring masses of 1-10 kg and 0.1-1 kg, respectively (Silva et al., 2018a). The propulsion systems of interest here are of the electrothermal type, in that they use electrically generated heat to initiate the propulsion process. Extensive overviews of these and other types of micropropulsion systems can be found in works such as those of Leomanni et al. (2017), Lemmer (2017), Silva et al. (2018a) and Levchenko et al. (2018).

2.2 Micropropulsion research at TU Delft

Ongoing work on miniaturised propulsion systems at TU Delft's Department of Space Systems Engineering treats the development of MEMS- (Micro-ElectroMechanical Systems) based electro-thermal propulsion modules functioning on environmentally-friendly, non-toxic propellants. Particular emphasis is placed on water in ice/liquid form, owing to such advantages as high mass density and low molecular mass, availability, environmental friendliness and benign chemical nature (Guerrieri et al., 2017a). In that regard, two concepts are of primary focus (Cervone et al., 2017):

- Vaporising Liquid Microresistojet (VLM): Water is evaporated by a heating element in a dedicated chamber and then expanded through a conventionally shaped nozzle for the generation of thrust (see Fig. 2.1a). For input heat powers of 1.87-9.01 W, the process typically establishes temperatures of 373-773 K and pressures of 100-500 kPa in the chamber, leading to thrusts and specific impulses in the approximate ranges of 0.75-3.86 mN and 105-115 s, respectively. The exact operating conditions depend on the efficiency of the vaporisation process, the nozzle configuration, etc. (Silva et al., 2017, 2018a)
- Low Pressure Free Molecular Microresistojet (LPM): A quantity of ice is sublimated in the tank by a heating element such that the pressure is maintained at the water vapour pressure. The gaseous molecules are fed via a feed system into a plenum and are then expelled via one or more heated slots for the generation of thrust (see Fig. 2.1b). Chamber temperatures and pressures are typically in the order of 300-700 K and 50-300 Pa, respectively, yielding typical thrust values as 0.39-3.59 mN (Guerrieri et al., 2017a). Evidently, the most relevant differences from the VLM concept are the allowable operating pressures/temperatures and the lack of a nozzle as an expansion element (Cervone et al., 2015).

The thruster modules are designed with a view to modularity and ease of integration, such that multiple configurations of the sub-components may be installed and assessed, but also the thrusters

themselves may be assembled into arrays. Besides the obvious gains in mass and volume, the development process aims for high reliability at fast-response rates. To that end, the main development challenges include the characterisation/enhancement of the vaporisation/sublimation process, storage of propellants and containment of leaks, commercial valve integration and actuation, optimisation of the expansion geometries, quantification of flow rarefaction effects, etc. (Guerrieri et al., 2017a,b; Silva et al., 2018b).

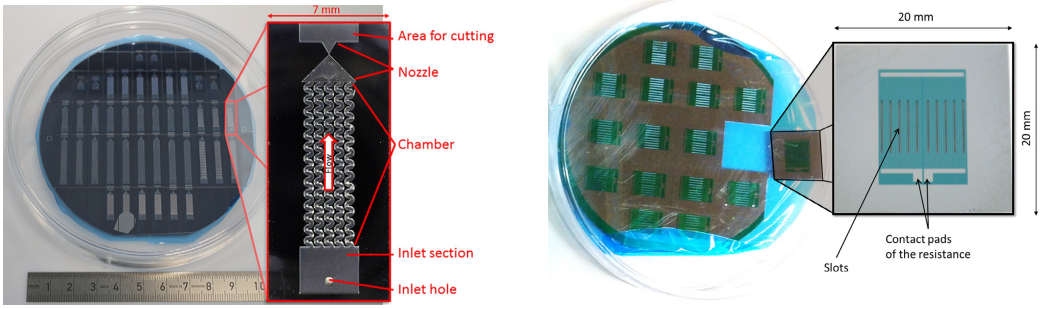

(a) Vaporising Liquid Microresistojet. Extracted from Silva et al. (2017).

(b) Low Pressure Microresistojet. Extracted from Guerrieri et al. (2017a).

FIGURE 2.1: Samples of microthrusters fabricated at the Delft University of Technology.

The present work focuses on the VLM concept and, in particular, its nozzle component. The nozzle is of the planar convergent-divergent type, in which a pair of straight flat walls seal the nozzle on the sides. These nozzles typically feature throat widths and nozzle depths in the order of 10^{-2} mm and 10^{-1} mm, respectively. This causes their flow behaviour to depart markedly from that of conventional-scale, axisymmetric nozzles, as is briefly explained in the following section.

2.3 Brief review of gas dynamics in low density micronozzles

The convergent-divergent nozzle concept is inherent to virtually every rocket/spacecraft chemical propulsion system in use, as an efficient means of extracting momentum from the acceleration of gaseous combustion products. In conventional-scale nozzles, stagnation pressures originating from combustion processes in the chamber are in the order of 100 bar, resulting in nozzle Reynolds numbers typically in the range of millions (Sutton and Biblarz, 2017). These flow conditions confine the diffusive phenomena of viscosity and heat conduction to only very thin boundary layers at the wall. The bulk mass flow is orders of magnitudes larger than the portion of the flow moving adjacent to the walls, allowing - as a first approximation - for viscous effects to be neglected and for the flow to be assumed a continuous uniform medium. This enables fairly accurate approximations of performance via simple analytical expressions and fairly accurate deduction of highly-performant nozzle shapes by simple numerical techniques. The nozzle shape design is primarily driven by the need for rapid alignment of the nozzle flow prior to its exit into a design ambient pressure, for minimum loss of momentum. The miniaturisation of nozzle geometries introduces flow phenomena that nullify these assumptions.

When the nozzle dimensions are reduced to the milli-/micro-meter scale, the relative size of boundary layers developing at the walls is enough to occupy a large - and, under certain conditions, complete - portion of the nozzle cross section. A peculiar situation is established in which the supersonic core of the flow is traversing the nozzle parallel to comparably sized subsonic regions. The subsonic layers reduce the effective nozzle area and often provide a path for the exit conditions to communicate upstream into the convergent section. Flow alignment is no longer the sole primary concern and a trade-off with the desire to minimise viscous losses is imposed. The minute dimensions further imply a stark increase in the surface to volume ratio, amplifying the impact of any heat transfer phenomena to/from the flow

and rendering their control a key performance driver. Lastly, at sufficiently low densities, the individual gas molecules traverse paths between collisions comparable to the nozzle dimensions. The flow can then no longer be treated as continuous or uniform and fundamentally different theoretical treatments are needed for meaningful estimations of performance. An overview on some of these mechanisms can be found in Louisos et al. (2008), although the reader is encouraged also to explore more recent literature, as a lot of new insights have been produced over the past decade or so [1].

The combination of the above factors complicates micronozzle shape design beyond the capacity of existing numerical/experimental techniques and the search for consistently well-performing design methodologies is currently feeding a dedicated research field, which this work aims to contribute to.

2.4 Two-phase flow in VLM nozzles

Two-phase flow in the nozzle of the VLM will generally manifest in any or both of two manners:

- droplets originating from insufficient vapourisation in the chamber
- condensation of vapour due to expansion as it traverses the nozzle

In other thruster concepts a third scenario exists, in which the hot gas may impinge on the colder walls of the nozzle and condense on the spot or expel heat that will eventually encourage this process. But, it is explained later that neither of these factors is applicable in typical VLM nozzle conditions, hence this mechanism is here ignored. A brief discussion on the other two follows below.

2.4.1 Two phase flow due to insufficient vapourisation

Concerning the first of the above points, Silva et al. (2018a) performed an approximate volumetric experimental measurement on some of the TU Delft VLM geometries and found it is likely that a finite amount of droplets may find their way from the heater into the nozzle. To the author's knowledge, there is no detailed experimental investigation of this phenomenon in literature and even numerical studies are extremely limited. The most notable works are those of Bhattacharya et al. (2013), Greenfield et al. (2018) and Kudryavtsev et al. (2018), who extracted basic conclusions on the response of micronozzle flows to the seeding of minuscule solid particles, under a variety of flow configurations. There is still room for work in this area to be done. For instance, none of these investigations treated a 3D geometry (such that the effect of the planar wall is included), nor included effects such as the buildup/evaporation of the droplets as they traverse the nozzle or the interactions between the droplets themselves. They also did not investigate other related interesting phenomena, such as potential transient instabilities that the droplets would induce in the nozzle flow either upon their formation or as they traverse the nozzle.

A related numerical investigation of these effects was explored in the early stages of the present work, but it was eventually decided that there is so much uncertainty involved, that it is not realistic to expect physically representative results without resorting to extraordinarily complex simulations that would have required unavailable computational resources. For instance, for a physically realistic analysis, one cannot simply assume solid particles of extremely minute and uniform size. Incomplete vapourisation, especially in a heater of geometry as complex as the one used in TU Delft thrusters (Cervone et al., 2015), is a rather unpredictable phenomenon, that may as well result in droplets sizeable enough to

[1] Indicatively, the reader is referred to the works of Morinigo and Quesada (2010) and Louisos and Hitt (2012) for the influences of temperature and heat transfer mechanisms; of Darbandi and Roohi (2011) and Torre et al. (2011) on the importance of accounting for the influence of rarefaction effects; Louisos and Hitt (2011a) on transient phases of operation; and Louisos and Hitt (2014), Pearl et al. (2014) and Stein and Alexeenko (2011) for the performance of alternative nozzle concepts.

be deformable or droplets that come at a size distribution too diverse to be uniformly modelled. That is before even considering other aspects of the process, such as the interaction mechanisms between the droplets and the nozzle walls, which is not necessarily a purely specular impingement/reflection, the evaporation of the droplets, etc. What is more, the present author believes that if the nozzle's performance is impacted by the heater's under-performance, any optimisation efforts should focus on the heater itself, rather than the nozzle. In view of these points, it was decided to instead focus this work on the prospect of condensation due to expansion.

2.4.2 Two phase flow due to expansion-induced condensation

This matter too, has received very limited attention in existing micronozzle studies. It has briefly been touched upon in the experimental studies of water-fed microthrusters by Cen and Xu (2010) and Nishii et al. (2019), both of whom noted that no condensation was observed in the flow. However, their instrument of observation was the naked eye, which is admittedly not particularly sensitive, especially since (as is explained later) the droplet sizes involved in such cases are below what is resolvable by the human eye. In a later work, Giorgi and Fontanarosa (2019a) also noted the issue in passing, but stepped on the aforementioned analysis of Cen and Xu (2010) to reason that for their purposes the phenomenon could be ignored. Haris and Ramesh (2014) examined the matter in more detail, outlining stagnation temperature ranges such that condensation in the expander could be avoided. However, their work implicitly assumed that the steam will condense immediately once it reaches saturation, while (it is explained later that) it is a fundamental characteristic of supersonic nozzle condensation that the vapour far exceeds its saturation point before any meaningful condensation ensues.

Perhaps the most detailed treatment so far has been given by Louisos and Hitt (2010). They briefly discussed some of the basic physics behind condensation and went on to perform numerical simulations to assess its likelihood in nozzle flows of their interest. The authors sought to avoid entering complex investigations of the issue, so their work inadvertently contains multiple blunt simplifications. Most notably, they do not actually model the condensation process itself, but instead provide some "a posteriori" rough estimates of the impact that the condensation could have had on the flow, based on the purely gaseous flow solution. Indicatively, the noted that the flow in the expander of their nozzle could experience a temperature increase as a result of condensation of up to almost 400 K. Approximate as it may be, their work is notable as perhaps the only to have highlighted the issue in a detailed manner and - most relevantly for our purposes - for giving some first indications that the prospect of condensation is, in fact, a realistic scenario for micronozzles.

The following section explores the underlying physics in a bit more detail and discusses further whether the matter of condensation is worth exploring, before finally specifying the scope of this work.

2.5 Water vapour condensation in supersonic nozzles

The entirety of the work presented in this document has originated from the simple consideration that as the water vapour expands towards the outlet of the resistojet's micronozzle, its temperature and pressure drop and hence it may reach conditions to transition back to liquid form. The phenomenon of water vapour condensation in nozzles was first observed by the early gas dynamics pioneers Ludwig Prandtl and Adolf Busemann in the 1930s and plagued the design of supersonic/hypersonic wind-tunnels for much of the 20th century (Wegener, 1954, 1975). In the more recent past few decades, it has drawn extensive research from the energy sector, due to its relevance to industrial applications such as the use of nozzles to actuate turbines in nuclear reactors. That research forms the backbone of the analysis in this work. This section outlines the general physics of the phenomenon and explains

why it is of relevance to water-fed micronozzle research and how it has motivated this work.

2.5.1 General overview

The transition of vapour into liquid water requires that it is first brought to saturation conditions, such that it can overcome the energy barrier associated with the intermolecular bonds for the formation of the first liquid surface. The initial process by which vapour molecules bond to form a liquid cluster is called nucleation. Nucleation may take place either homogeneously, in which case vapour molecules will spontaneously coalesce between themselves to form droplets or heterogeneously by instead coalescing on already available foreign particles, such as dust. The energy that has to be expended in the former case is generally multiple times higher than in the latter and hence the heterogeneous mechanism prevails in most processes in nature.

Most condensation phenomena typically observed in everyday life take place under equilibrium conditions. In the troposphere, for instance, when atmospheric conditions are suitable to drive a quantity of vapour to saturation, it will condense on existing solid particles (dust, salts, etc) and form minuscule droplets, in an exothermic reaction that releases heat to the atmosphere. If conditions are right, the vapour molecules will keep coalescing onto the surface of the newly formed droplets and continue to release heat, in a sequence that may eventually lead to the formation of clouds. This is a slowly developing process, during which the vapour continually shifts from one position of thermodynamic equilibrium to another (Put, 2003). That is, the timescale of the phenomenon is slow enough to allow for thermodynamic phenomena to reach equilibrium practically instantly. In the conditions found in many industrial processes involving the flow of steam, including those in supersonic nozzles, this ceases to be the case.

The rapid expansion in conventional supersonic nozzles results in cooling rates typically in the order of 10^5-10^6 K s^{-1} (Wegener and Wu, 1977; Abraham, 1981). Under such conditions, the timescale is too short for sufficiently frequent intermolecular collisions to take place or for the molecules to form bonds and clusters as they do under equilibrium. The gas reaches its saturation point and goes on to far exceed it without condensation occurring, remaining in vapour state under thermodynamic conditions that would have normally caused it to transition phase. The local pressure becomes multiple times higher than vapor's saturation pressure at the local temperature and this "supersaturated" vapour is said to be in a "non-equilibrium" or "metastable" state. These types of nozzle flows generally involve either pure superheated steam or steam transferred by a carrier gas (air, argon, etc). The presence of foreign nuclei such as dust is typically very limited or non-existent and the timescale needed for heterogeneous condensation far exceeds that of the supersonic flow. As a result, it is never observed in practice and homogeneous nucleation instead now becomes the driving mechanism (Bakhtar et al., 2005).

In the metastable state, the vapour experiences statistical fluctuations that lead to a continuous agglomeration and collapse of molecular clusters, a microscopic process during which no macroscopic disturbance is noted in the flowfield (Ford, 2004). Eventually, however, the degree of supersaturation becomes extreme enough for the energy barrier of homogeneous condensation to be exceeded and the vapour spontaneously starts collapsing into minute liquid clusters. Nuclei with radii commonly in the order of 10^{-10}-10^{-9} m will grow several orders of magnitude within a fraction of a second and reach sizes of 10^{-6}-10^{-5} m by the time they have exited the nozzle. This is a strongly exothermic phenomenon that may drastically alter the flow topology inside the nozzle, raising the pressure and temperature in the expander markedly above what it would have been in the nominal isentropic expansion. The entropic changes resulting from the release of latent heat also impact the efficiency of the nozzle.

Instructive visualisations of the phenomenon are offered in Figs. 2.2 and 2.3 (note the figures are not related). It can be seen that the droplets grow rapidly within a narrow condensation zone and the

corresponding sharp increase in pressure establishes a shock-like disturbance that heavily upsets the flow. The latent heat released during the process raises the temperature, quickly driving the vapour back to its equilibrium state. Eventually, the growth is quenched and the region near the nozzle exit exhibits a two-phase flowfield in equilibrium, with a quasi-steady number of droplets that no longer grow.

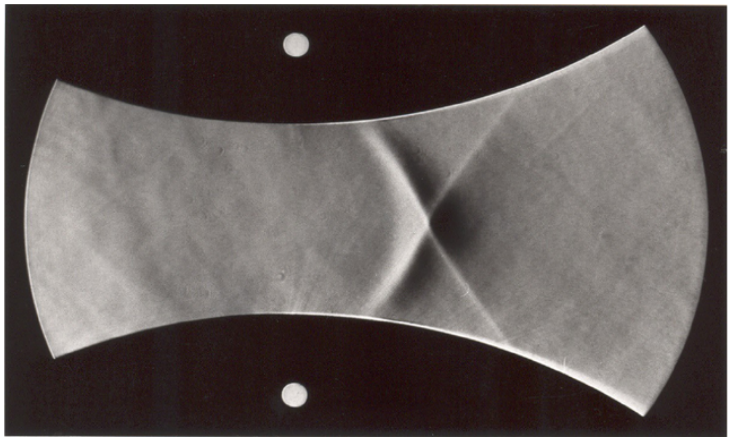

FIGURE 2.2: Schlieren visualisation (i.e., density gredients; here, whiter means denser) of the shock-like structure of the condensation front in a supersonic wind-tunnel nozzle. In this case, atmospheric (i.e., moist) air was used. The steam in the carrier gas, supersaturated due to the supersonic expansion, eventually collapses to a narrow condensation zone. The resulting sudden release of latent heat causes a sharp increase in pressure that establishes a shock-like disturbance. The condensation fronts form along expansion fans that emanate from each nozzle wall and they interfere at the centerline, resulting in the X-shaped pattern. The image is courtesy of Prof. Gunther H. Schnerr of the Technical University of Munich.

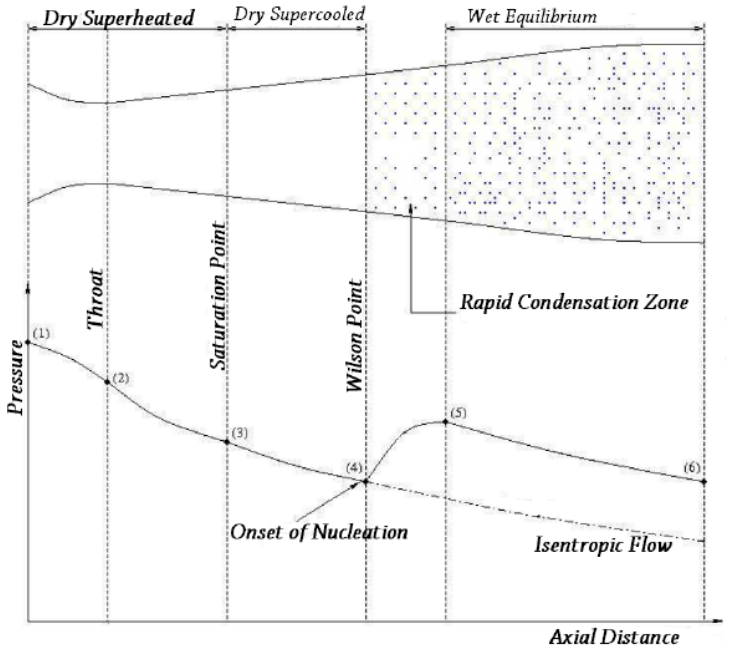

FIGURE 2.3: Schematic of a typical condensation process in a supersonic nozzle. The release of heat that follows the onset of condensation increases the flow pressure markedly above what it would have been in the isentropic case. Extracted from Hasini et al. (2012).

While Fig. 2.3 is drawn qualitatively, it is not exaggerated and realistically depicts the degree to which condensation can impact the flow pressure and hence the nozzle performance. This is what has

prompted the careful examination of whether this can happen inside the micronozzles designed at TU Delft and what has motivated this work.

2.5.2 The prospect of condensation in micronozzles

To offer the reader some insight into what thermodynamic space the operation of the VLMs of interest here occupy relative to the thermodynamics of water, a phase diagram of H2O has been plotted in Fig. 2.4 according to the relations given in Daucik (2011) and an indicative operational range for VLMs has been imposed on it. The region is bounded by assuming a maximum stagnation temperature of 673 K (400 °C) and a maximum stagnation pressure of 5 bar. It has been assumed that the expansion in the nozzle divergent will not drive the vapour below 0.02 bar (2000 Pa). These values are typical of the VLMs examined in this work (shown in Ch. 7), but otherwise generally arbitrary and only indicative, as one may as well choose stagnation pressures of 7 bar or higher or temperatures of 773 K or higher, as long as material properties and other design considerations allow or require this. What can be seen is that, depending on the chosen stagnation conditions and nozzle geometry, the flow in the nozzle may cross the saturation line and dive well into the liquid and even solid regions, so the thermodynamic space for the prospect of condensation to be conceivable is certainly present. These aspects are revisited in the following chapters.

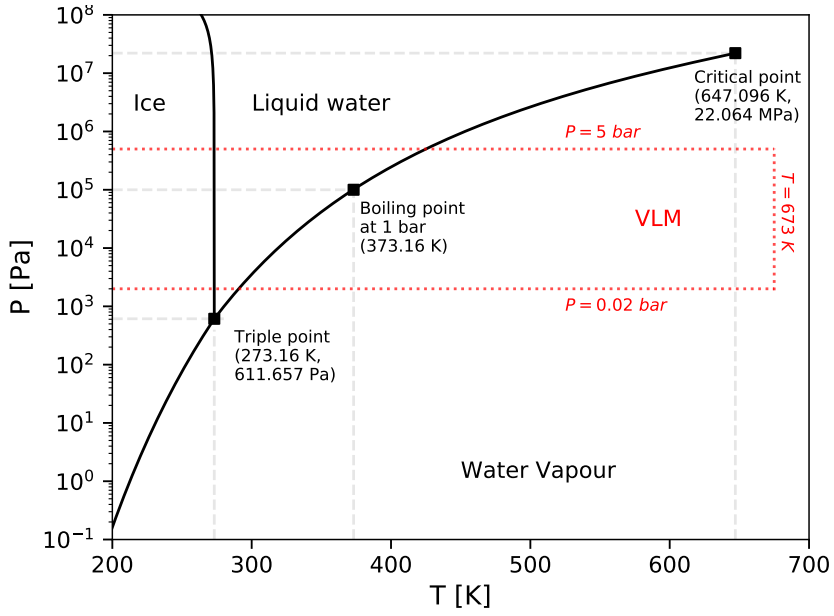

FIGURE 2.4: Basic phase diagram of water. The curves have been plotted according to the relations in Daucik (2011). The dotted box annotates the rough region of operation of the micronozzles examined in this work, for the vapour phase. The region is drawn as a rectangle for clarity, but it should be understood that the vapour will expand in the nozzle. Therefore, it is unlikely that the lowest temperatures will be reached at the highest pressures and only the flow expanded to a few kPa will reach the low-temperature end. The temperature axis has been truncated at 200 K, but the nozzle flow temperature may drop below that value, depending on the operating conditions. The 0.02 bar threshold in only indicative of a typical value in steady-state operating conditions and the pressure in the nozzle may drop below it under lower stagnation pressures or during transient operation. It can be seen and will be shown again in Ch. 7 that as the vapor expands in the nozzle divergent, it moves well into the liquid and solid phase space, which it would have transitioned to under equilibrium conditions.

In determining whether condensation really is a matter of concern in micronozzles, one must take into account the fact that the difference in scale with conventional nozzles plays a dominant role here as well. It was stated in the previous section that cooling rates in large-scale nozzles are in the range

10^5-10^6 K s^{-1}. Micronozzles such as the one depicted in Fig. 2.1a are typically 2-3 mm in length and the expander occupies roughly 1/3rd-1/2nd of that. If, for the sake of the discussion, it is assumed that the superheated vapour enters the nozzle at 473 K (200 °C), it is quite probable its temperature will have dropped by more than 200 K by the time it exits the nozzle (this is shown in Ch. 7). If it is also roughly assumed that the flow traverses the expander at an average velocity of 700 m s^{-1} (about Mach 2 for typical nozzle conditions), then the resulting cooling rate is in the order of 10^8-10^9 K s^{-1}. The cooling rate is therefore roughly 3 orders of magnitude higher than in conventional nozzles, which is the result of the fact that the flow experiences about the same degree of expansion in both types of nozzes, but in the micronozzle the spatial distance over which this takes place is orders of magnitude smaller. The resulting cooling rates are extreme and this is important to note, because it is known that the faster the vapour cools, the more it is driven out of equilibrium and the deeper into the supersaturated state it delves before condensation ensues (Moses and Stein, 1978a). Condensation is hence delayed and it may then be that the time the flow spends in the nozzle is too short for the vapour to condense or that even if condensation does occur, it is of limited extent and of little consequence.

On the other hand, it is explained in Ch. 5 that in these particular flowcases the water vapour is expected to be supercooled to extraordinary levels, below the freezing point of liquid water itself (273 K). In that region, the saturation pressure drops quite rapidly with temperature and this implies that the extreme level of supersaturation needed to trigger nucleation may be reached rather quickly. In literature, the present author has been able to trace only two past works that experimentally touched upon the matter of condensation in nozzles of somewhat comparable geometry; those of Abraham (1981) and Bobbert et al. (2002)[2]. Indeed, they both noted the occurrence of condensation. In a later work, exploratory DSMC simulations by Jansen et al. (2009) on the nozzle of Bobbert et al. (2002) found that the condensation is likely to have sensibly affected the flow, causing a temperature rise of 20 K and a velocity increase of about 30 m/s.

On these grounds, it has been decided that the prospect of condensation inside the micronozzles produced in TU Delft is both plausible and potentially impactful enough to warrant a detailed investigation. This has produced the analysis presented in this document, the scope of which is framed in the following section.

[2]It must be clarified that the nozzle of Abraham (1981) is formally too large to be considered a micronozzle and also operated on a different propellant (sulphur-hexafluoride or SF6), but its characteristic dimensions are still only a fraction of 1 mm and similar principles of operation apply. The nozzle of Bobbert et al. (2002) is in fact a micronozzle operating on water, but an axisymmetric one that is not influenced by the dominant presence of the heated planar wall.

2.6 Scope of this work

Following the above discussions, the scope of this work is framed by the formulation of a research objective, this is realised by answering a series of associated research questions. These are given below.

RESEARCH OBJECTIVE:

to implement a numerical model for the investigation of non-equilibrium water vapour condensation in vaporising liquid microthruster supersonic nozzles at near-vacuum ambient conditions, by coupling the effects of wall heat transfer and vapour phase change inside three-dimensional geometries, with the aim of identifying whether the phenomenon should be a design consideration in the future and formulating associated design directives

PRIMARY RESEARCH QUESTIONS:

1. RQ1: Does condensation occur in common operating conditions (to be defined later) of these micronozzles?
2. RQ2: How is the potential onset of condensation affected by the stagnation conditions (pressure and temperature) in the nozzle?
3. RQ3: How is the potential onset of condensation affected by the nozzles' geometry, in terms of their expander opening angle and their depth?
4. RQ4: If condensation does ensue, does it have a substantial (to be quantified at the end of this section) impact on the nozzles' macroscopic performance (thrust and specific impulse)? And if so, what is that impact?

SECONDARY RESEARCH QUESTIONS:

- RQS: Eventually, should the prospect of condensation be a design consideration in the future? If so, what design choices are recommended?

A quantification is needed for what is considered a "substantial" impact on the performance of the nozzle, as formulated under RQ4. This is heavily mission dependent and there is no strict threshold for it. For instance, a CubeSat with a main mission goal to perform technology demonstration of onboard sub-systems such as a novel onboard computer, is unlikely to be affected by a 1% offset in thrust. In contrast, the same threshold may be unacceptable for a spacecraft carrying a sensitive optical payload with strict pointing requirements. Here, somewhat arbitrarily, this threshold is set at 2% on the assumption that even for benign mission requirements, a propulsion system deviating more than that from predicted performance would likely be a matter of some concern, especially when integrated over a long impulse maneouvre.

2.6.1 The methodology in brief

To address these questions a numerical model capable of capturing the physics of condensation is implemented in the open-source computational platform OpenFOAM. An existing numerical solver for general compressible flows is adopted from that platform and is heavily modified, to make it suitable for capturing the effects of mild rarefaction inside the micronozzle and the physics of condensation in supersonic conditions. The choice of OpenFOAM has been motivated at the early stages of this work by the following considerations:

- As will become clear in the following chapters, a myriad of considerations are involved in the modelling of condensation. Since micronozzles exhibit quite particular flow physics, at the beginning there was no clear overview of the precise phenomena the model would have to account for. As such, there was the preference to have a fully configurable numerical tool that could be modified at will and without restrictions, such that the model could be tailored optimally to the case at hand.
- OpenFOAM is open-source and therefore freely accessible without limits, which eliminated any restrictions that come with using commercial software. Besides the obvious practical advantages, it also implies the principle of the research being easily available to everyone.
- A more personal reason to the author was also involved: this thesis is an educational activity in the end and the author wished to take this opportunity to familiarise himself with numerical simulations, a field he initially had no affinity to. It was deemed that there was far more educational value involved in implementing the model from start, rather than simply using an already existing commercial framework.

Following the choice of the tool, the work was then segmented into four main ”work packages”:

- The assembly of a single-phase (pure vapour) model that can satisfactorily reproduce relevant micronozzle flow physics in the absence of any phase change, such as it could be used as the basis for the development of the two-phase model.
- The compilation of a real-gas thermophysical model that allows for the accurate estimation of the properties of water in vapour and liquid form, as well as along the saturation line.
- The implementation of the condensation model, to capture the processes of droplet birth and growth.
- The application of the model on the numerical simulations of selected micronozzle cases, such that the research questions can be addressed.

The rest of this document treats each of these steps sequentially in the following chapters.

Part I

Single-phase model

CHAPTER 3

Single-phase model

Before implementing the condensation model, it is necessary to ensure that a numerical tool is available which can satisfactorily simulate supersonic nozzle flows under purely gaseous conditions. This single-phase model is outlined in this chapter.

3.1 Modelling approach

The Loschmidt constant - a measure of the number of particles of an ideal gas per unit volume for given ambient conditions (Vincenti and Kruger, 1967) - measures approximately 2.67×10^{25} of an ideal gas's particles per cubic metre under standard atmospheric conditions, implying there are roughly 3×10^{10} particles in just one millionth of a cubic millimetre. This justifies the assumption that the properties of any flow whose characteristic scale is larger than, for instance, 1 mm - such as those most commonly encountered in practice - are macroscopically continuous and independent of the molecular topology of the gas (Shen, 2005). The flow properties can be defined at the infinitesimal scale and their variation may be assumed continuous in space and time. This allows for the description of the flow with a relatively compact set of equations, that may be expressed both at the infinitesimal and integral scale, typically given in the form of the Navier-Stokes equations or some variation (Sec. 3.2).

The continuum assumption breaks down when the characteristic scale of the gradients of the macroscopic properties becomes comparable to the average length of a molecule's path between two collisions, as predicted by kinetic theory, fittingly termed the "mean molecular path length". This average is statistically determined over the multitude of molecules in the gas and serves as input to a commonly used qualitative measure of a flow's degree of rarefaction, the Knudsen number, defined as:

$$Kn = \frac{\lambda}{L} \tag{3.1}$$

where λ is the mean molecular path and L is the chosen characteristic length of the flow. The mean free path is typically approximated via the classical kinetic theory of gases as (Vincenti and Kruger, 1967):

$$\lambda = \frac{\mu}{p}\sqrt{\frac{\pi k_B T}{2m}} \tag{3.2}$$

where p, T and μ are the gas pressure, temperature and viscosity, respectively, m = 2.988 $\times$ 10^{-26} kg is the molecular mass of water vapour, k_B =1.38 $\times$ 10^{-23} $m^2 kgs^{-2} K^{-1}$ is the Boltzmann constant and $\pi \approx 3.14$ is the well known mathematical constant. The precise values of Kn that define the flow regimes intermediate between continuum and vacuum is often a basis for debate, but a conventional adaptation of Tsien's (Tsien, 1946) original division is the following:

- $Kn < 0.001 \rightarrow$ Continuum
- $0.001 < Kn \leq 0.1 \rightarrow$ Slip-flow
- $0.1 < Kn \leq 10 \rightarrow$ Transitional

- $Kn \geq 10 \rightarrow$ Free molecular

and is the one used for the rest of this document. Note that a given flow may exhibit varying degrees of rarefaction at different locations. Therefore, if one chooses a characteristic length representing the entire flow in an attempt to define a single Knudsen number, the above definitions are obscured. It is thus common to define a "local Knudsen number" by choosing the characteristic length to be the scale length of the flow gradients (Bird, 1994):

$$L = \frac{\rho}{d\rho/dx} \tag{3.3}$$

In this work, however, we stick with the definition of Eqn. 3.1 and the nozzle throat width is used as the reference length for the rest of the discussions in this chapter.

In a typical micronozzle, the throat width is in the order of micrometers and the length spans only a couple of millimetres. At the same time, the flow will expand from a relatively low stagnation value (usually between 1-5 bar) into vacuum, therefore it undergoes a rapid expansion within a short geometric distance. Under these conditions, the characteristic geometric scale of the flow tends to that of the nozzle geometry and the corresponding Knudsen number veers into the slip and transitional regimes. It is then common to use kinetic methods based on statistical techniques, that do not depend on averaged macroscopic properties and instead track the motion and collisions of individual particles for the description of the flow. Characteristic examples are the widely used Direct Simulation Monte Carlo method (Bird, 1994) and the recently emerging Lattice Boltzmann Method (Mohamad, 2011).

However, the fact that these methods track individual particles make them very computationally expensive for all but the most highly rarefied cases. They certainly bear a computational cost far too prohibitive for the means the author has had in his disposal. As a result, the numerical analysis here is based on the Navier-Stokes approach, accepting any potential inherent loss in the realisticity of the solution if the Knudsen number exceeds the continuum range.

3.2 The governing equations

The continuum description, here as in the majority of literature, is mathematically implemented via the Navier-Stokes (NS) equations, which have become the cornerstone of modern fluid mechanics and computational fluid dynamics in the examination of most ordinary phenomena of fluid motion (Versteeg and Malalasekera, 2007). The equations are derived on the principles of conservation of mass, momentum and energy across a control volume in the flow (an example is given in Fig. 3.1). A multitude of forms can be derived for various applications, but the form most relevant to this work is the following:

Conservation of mass:

$$\underbrace{\frac{\partial \rho}{\partial t}}_{\substack{\text{time rate of change} \\ \text{of mass accumulation}}} + \underbrace{\nabla \cdot (\rho \vec{\mathrm{V}})}_{\substack{\text{mass transport} \\ \text{by convection}}} = 0 \tag{3.4}$$

Conservation of momentum:

$$\underbrace{\frac{\partial}{\partial t}(\rho \vec{\mathrm{V}})}_{\substack{\text{time rate of change} \\ \text{of momentum accumulation}}} + \underbrace{\nabla \cdot (\rho \vec{\mathrm{V}} \vec{\mathrm{V}})}_{\substack{\text{momentum transport} \\ \text{by convection}}} = - \underbrace{\nabla p}_{\substack{\text{pressure forces}}} + \underbrace{\nabla \cdot \vec{\tau}}_{\substack{\text{viscous forces}}} \tag{3.5}$$

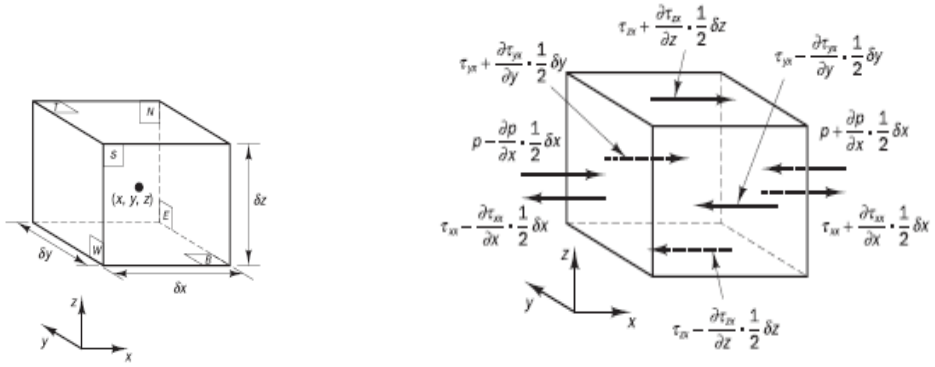

(a) Infinitesimal control volume

(b) Stress components in the x-direction

FIGURE 3.1: Infinitesimal control volume for the derivation of the Navier-Stokes equations. The stress state is given on the left as an example of the factors accounted for when setting up the conservation laws. Extracted from Versteeg and Malalasekera (2007).

Conservation of energy:

$$\underbrace{\frac{\partial}{\partial t}(\rho E)}_{\substack{\text{time rate of change}\\ \text{of energy accumulation}}} + \underbrace{\nabla\cdot(\vec{\mathrm{V}}(\rho E+p))}_{\substack{\text{energy convection +}\\ \text{pressure work}}} = \underbrace{\nabla\cdot(k\nabla T+(\vec{\tau}\cdot\vec{\mathrm{V}}))}_{\substack{\text{heat conduction +}\\ \text{viscous dissipation}}} \tag{3.6}$$

where p, ρ and T are the flow pressure, density and temperature, $\vec{V}$ and $\vec{\tau}$ denote velocity and surface shear stress vectors, E is total energy contained in the flow and k expresses the fluid's thermal conductivity. The above treatment describes fluid motion via 5 partial differential equations (1 $\times$ continuity, 3 $\times$ momentum and 1 $\times$ energy), but contains 10 variables (ρ, p, T, E, $\vec{V}$, $\vec{\tau}$). Additional relations are needed to close the system.

In the Newtonian fluid description, the shear (viscous) stress is assumed to be linearly proportional to the rate of deformation of the control volume and related to it via two constants of proportionality as

$$\tau=\mu(\nabla\vec{\mathrm{V}}+\nabla\vec{\mathrm{V}}^{T})-\lambda\nabla\cdot\vec{\mathrm{V}}I \tag{3.7}$$

The dynamic viscosity μ and second viscosity λ are physical parameters relating the stresses to linear and volumetric deformations, respectively. The dynamic viscosity typically follows from empirical expressions. Little is known about the precise nature of λ, but Schlichting (1979) showed that a good approximation may be obtained as $\lambda=\frac{2}{3}\mu$ and this is by far the most common implementation in modern NS schemes.

The total energy is expressed as the sum of the gas's enthalpy and kinetic energy as:

$$E=h-\frac{p}{\rho}+\frac{|V|^2}{2} \tag{3.8}$$

In turn, the enthalpy h is expressed $h=e+\frac{p}{\rho}$ and describes the energy enclosed in a stationary system as the sum of the internal (vibrational, translational, rotational, etc) energy of the molecules and the work that had to be exerted on the system's surroundings to make room for its presence. The system of equations can be closed with the use of an equation of state, usually the simple ideal gas law:

$$p=\rho RT \quad \& \quad e=C_vT \tag{3.9}$$

However, the thermodynamic behaviour of water vapour generally deviates from that of an ideal gas and a real-gas equation of state is needed. That is the subject of Ch. 4.

3.3 The numerical solver

The standard distribution of OpenFOAM currently provides two solvers capable of resolving the features of supersonic flow: a density-based ”rhoCentralFoam” solver and a pressure-based ”soniFoam” one. In the former case, the density is determined via the solution of the continuity equation and the pressure follows from the equation of state; in the latter, a pressure predictor-corrector equation is instead solved first for the determination of the pressure field (Versteeg and Malalasekera, 2007). Both solvers are transient, i.e., the temporal evolution of the flow is resolved.

A micronozzle exhibits flow that starts at low Mach numbers at the inlet, reaches supersonic speeds at the outlet and retreats to subsonic or stagnant values downstream of the outlet. This is somewhat inconvenient from a numerical perspective, because neither of these types of solvers is efficient across the full range of Mach numbers. The solution propagation is bounded by a timestep that is determined at the local sonic velocity, therefore it becomes rather inefficient at those regions where the flow is subsonic. In any case, these are the only options available and given that rhoCentralFoam is typically found to outperform sonicFoam in terms of resolution accuracy and numerical performance (Marcantonia et al., 2012; Bondarev and Kuvshinnikov, 2018), as well as that it implements a fairly straightforward numerical scheme that makes the implementation of the condensation model simple, it has been the choice for this work.

The mathematical details are described in detail in Greenshields et al. (2009) and will not be repeated here. Some aspects are visited in Ch. 5, to explain the numerical implementation of the two-phase model. Briefly, the solver is based on the central-upwind discretisation schemes of Kurganov and Petrova (2007), essentially employing the local sonic velocities at the computational domain’s cell interfaces to deduce weight factors for the computation of the fluxes of flow properties between the cells. It is an explicit solver, meaning the properties are computed based on the values of the previous timesteps only and the governing equations are solved in a sequential and segregated manner. This numerical setup introduces some limited numerical diffusion that may impact the resolution of high-gradient features such as shockwaves (Modesti and Pirozzoli, 2017), but has been shown to be suitable for most common compressible aerodynamic applications (Greenshields et al., 2009).

3.4 Short-comings of the governing equations in rarefied flows

The inability of the Navier-Stokes equations to accurately reproduce flow cases exhibiting even mild degrees of rarefaction typically comes down to (any of) three causes:

- A linear variation of the shear stress tensor with the velocity gradient at the wall is assumed.
- The fact that, during the rapid expansion, the translational, rotational and vibrational modes of the internal energy distribution may no longer be in equilibrium is not modelled.
- The fact that the flow slips rather than comes to a halt at the wall is not accounted for.

In view of these shortcomings, in the early stages of this work multiple options were explored as potential candidates for improving the model’s performance against rarefaction inside the micronozzle. In literature, multiple attempts are recorded at devising a way to partly mitigate these deficiencies, with varying and limited degrees of success.

One common approach is to explicitly split the temperature into its translational, rotational and vibrational components and then introduce extra conservation equations for the internal energy component associated with each of these temperatures. Usually, this is done via a simple relaxation equation in the Landau-Teller form (Nikitin and Troe, 2008):

$$\frac{de^*}{dt} = \frac{1}{\tau}(\bar{e} - e^*) \tag{3.10}$$

where e^* is the internal energy mode in question, $\bar{e}$ is the equilibrium value towards which it relaxes during the expansion and τ is the relaxation time. Notable examples in this regard are the works of Bertolotti (1998), who studied the effects of energy relaxation on boundary layer stability and of Johnson et al. (2000, 2006), who intoduced a vibrational energy relaxation to simulate rarefied nozzle flow.

Other authors (Xu et al., 2008; San et al., 2009; Zhao et al., 2014) have used extended versions of the NS equations that are better suited for approximating the detailed kinetics of rarefied flows. In some works it has been suggested to use a modified form of the viscosity, such that the effect of relaxation on the gas can be approximated. For instance, Lockerby et al. (2005) suggested the use of a wall function to describe the non-linear variation of the stress tensor close to the wall, while Dongari et al. (2011) introduced an "effective viscosity" adjusted according to the mean free path length. In other works, authors have introduced different hydrodynamic descriptions altogether in an attempt to reproduce the behaviour of the rarefied flow, such as Dadzie and Brenner (2012), who used the concept of a "vollume diffusion velocity" in the NS equations and later obtained significantly improved performance for simple, isothermal, rarefied channel flows (Christou and Dadzie, 2018).

In the context of this work, however, virtually none of these approaches are applicable, because they are typically derived on the assumption (among other, sometimes blunt, approximations) that the fluid involved is an ideal monoatomic, diatomic or at most simple polyatomic gas. Examples are argon (Ar), nitrogen (N_2) or carbon dioxide (CO_2). The particular thermochemical nature of the water vapour molecule, however, does not satisfy this criteria: the arrangement of its atoms make it a strongly polar molecule, which means that the interactomic collisions do not follow the simple laws that describe the above gasses; in fact, it is mainly this polarity behind its real-gas behaviour (Lambert, 1977).

In view of the above, it was decided to stick with the original NS equations without modifications, apart from the introduction of dedicated boundary conditions at the nozzle wall to account for the slipping of the gas, as explained in the following section. From there on, it is assumed that as long as the degree of rarefaction is not very high ($Kn < 1$), the model gives an acceptable representation of the flow. This is tested in Sec. 3.5.1.

3.4.1 Wall slip conditions

In a series of experiments in the late 19th century, Kundt and Warburg (1875) examined the damping of a vibrating disc by various gasses at low pressures and the flow of low-pressure gas through a capillary tube. Their comparative calculations were in each case made on the assumption that the gas comes to a halt at the wall, as is normally assumed for viscous flows, but did not agree with the experimental results. At low pressures the disc damping decreased and, when the pressure in the tube was low enough for its radius to be comparable to the molecular mean free path length, the flow rate was higher than expected. They attributed both effects to a slip of the gas over the solid surfaces.

These initial observations and a large volume of subsequent work have led to the definition of a dedicated "slip-flow" regime and it is generally assumed (as mentioned in Sec. 3.1) that if the Knudsen number exceeds 0.001, rarefaction effects begin to manifest. The variation of the gas velocity and temperature relative to the solid boundary in the direction normal to the boundary experiences a discontinuity at the wall and the gas is effectively slipping against it (refer to Fig. 3.2). Up to a certain degree of rarefaction - which is usually problem-specific - the NS equations remain applicable as long as they are supplemented with dedicated boundary conditions to describe the slipping at the wall (Hadjiconstantinou, 2003; Barber and Emerson, 2006).

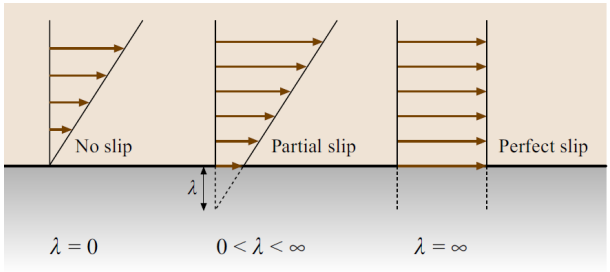

FIGURE 3.2: Visual interpretation of the Navier slip length, here denoted as λ. Extracted from Tropea et al. (2007).

By far the most commonly used velocity slip model is the one proposed by Maxwell (1879), expressed in vectorial form as:

$$u = u_w - \mathrm{A}\frac{2-\sigma_M}{\sigma_M}\lambda\nabla_n(\mathbf{S}\cdot\mathbf{V}) - \frac{3}{4}\frac{\mu}{\rho T}\mathbf{S}\cdot\nabla T - \frac{2-\sigma_M}{\sigma_M}\frac{\lambda}{\mu}\mathbf{S}\cdot(\mathbf{n}\cdot\tau) \tag{3.11}$$

where u is the gas velocity and u_w its velocity at the wall; σ_M is the tengential momentum accommodation coefficient, taking values from 0 to 1 and describing the extent to which the gas loses its momentum upon impinging on the wall; λ is the molecular mean free path; μ and ρ are the gas viscosity and density, respectively; $\mathbf{n}$ is the unit vector normal to the wall; and $\nabla_n\phi = \mathbf{n}\cdot\nabla$ describes the gradient of the variable normal to the wall. The parameter $\mathbf{S}$ is a mathematical operator which ensures that only the component of a vector that is tangential to the wall is kept. This is to mathematically express that the velocity only slips tangentially to the wall. It is defined via the identity vector I as $\mathbf{S} = \mathbf{I} - \mathbf{nn}$. Lastly, τ is the stress tensor given by Eqn. 3.7.

The right-most term $\left[-\frac{2-\sigma_M}{\sigma_M}\frac{\lambda}{\mu}\mathbf{S}\cdot(\mathbf{n}\cdot\tau)\right]$ in Eqn. 3.11 was introduced in later works by Barber and Emerson (2006) to account for the fact that when the gas slips over a curved surface, the contributions of the shear stress and shear heat flux must be included. The middle term $\left[-\frac{3}{4}\frac{\mu}{\rho T}\mathbf{S}\cdot\nabla T\right]$ expresses the fact that the rarefid gas will experience a drifting motion due to thermal gradients if the wall exhibits a temperature variation along its surface, a phenomenon known as thermal creep. The micronozzles of this work, however, are conical, so the wall is planar everywhere. Furthermore, the wall is assumed isothermal. As such, the two right-most terms in Eqn. 3.11 have been neglected for the rest of this work.

Similarly, a boundary condition for the temperature discontinuity at the wall is needed, with the most commonly-used relation being that of Smoluchowski (1898):

$$T = T_w - \left(\frac{2-\sigma_T}{\sigma_T}\right)\frac{2\gamma}{(\gamma+1)}\frac{\lambda}{Pr}(\mathbf{n}\cdot\nabla T) \tag{3.12}$$

where T is the gas temperature, T_w is its temperature at the wall, σ_T is the equivalent of σ_M for thermal accommodation and Pr is the Prandtl number, a dimensionless flow similarity parameter describing the ratio of momentum to thermal diffusivity and expressed via the gas viscosity μ, conductivity k and isobaric specific heat capacity C_p as:

$$Pr = \frac{C_p\cdot\mu}{k} \tag{3.13}$$

In this work, however, a slighly modified version is instead used, derived by Gokcen (Gokcen et al., 1987; Gokcen and Maccormack, 1989), as it has formally been derived in the limit of high Knudsen numbers and later shown by Lofthouse et al. (2008) to generally provide superior performance:

$$T = T_w - \left(\frac{2}{\sigma_T}\right)\frac{2\gamma}{(\gamma+1)}\frac{\lambda}{Pr}(\mathbf{n}\cdot\nabla T) \tag{3.14}$$

This condition is not originally included in OpenFOAM, therefore it had to be coded separately. The manner in which such boundary conditions are implemented in OpenFOAM is described in the work of Greenshields and Reese (2012) and will not be repeated here.

In summary, the single-phase model comprises of the NS governing equations 3.4-3.8, closed by the thermodynamic model described later in Ch. 4 and supplemented by the velocity slip and temperature jump boundary conditions at the wall, given by Eqns. 3.11 and 3.14.

3.5 Validation of the single-phase model

The discussions of the previous sections make it clear it is necessary to assess the model's capacity in reproducing flows exhibiting mild degrees of rarefaction, as well as the particular thermodynamics of water vapour. Ideally, it would be desirable to test the solver against experiment measurements featuring both these aspects simultaneously. Inconveniently, the present author could not find any such experiment in literature that is documented thoroughly enough to provide a suitable validation case. Hence, the solver is tested in each aspect separately and it is assumed that if it performs satisfactorily in each case, it will also do so when the flow physics are super-imposed. To that end, two experiments from literature are employed:

- The experiments of Rothe (1971), who provided detailed data on the internal flow topology of a small, low-density Laval nozzle operating on Nitrogen and expanding into near vacuum.
- The experiments of Cen and Xu (2010), who provided macroscopic performance measurements for a micronozzle of geometry and operational envelope comparable to the ones of interest here, operating on superheated water vapour.

Each case is presented separately in the following subsections.

3.5.1 Experiments of Rothe

The measurements of Rothe (1970, 1971) appear to be the only ones in literature that provide detailed data on the internal flow topology of a low-density nozzle, which is why they occasionally appear as a validation benchmark in works developing numerical tools for rarefied flows (see, for instance, the works of Chung et al. (1995), Ivanov et al. (1998) and Arlemark et al. (2012)). Rothe employed the electron-beam fluorescence technique and recorded measurements of density and translational/rotational temperature along the centerline, as well as along the radial directions at two selected locations on the centerline (Fig. 3.3).

Rothe used the Reynolds number as the primary experimental variable and ran multiple experiments on two separate nozzles with different throat diameters. To substantiate a decision on which experimental run to use here, an estimate of the micronozzle throat-radius-based Reynolds number is needed[1]. It is desired that a conservative estimate is made, so the minimum expected Re_t is pursued here. It must be noted that Rothe used a somewhat unusual definition of the Reynolds number, formulating it in terms of the condtions in the stagnation chamber:

$$B = \frac{\rho_0 (2H_0)^{1/2} r_t}{\mu_0} \tag{3.15}$$

with B being Rothe's notation for the Reynolds number, r_t the nozzle throat radius, the subscript 0 denoting stagnation conditions and ρ, H, and μ being the gas density, enthalpy and viscosity, respectively. Under the simplifications of ideal rocket theory under which it is typically estimated, the value of B attains a minimum at the lowest stagnation pressure and highest stagnation temperature. It is explained in Ch. 6 that, in this work, the minimum stagnation pressure is $p_0 = 1\,\text{bar}$ and the maximum stagnation temperature is $673\,\text{K}$. The nozzles in this work are typically $100\,\mu\text{m}$ deep, with a throat half-width of $45\,\mu\text{m}$. With these inputs, one may look up for the properties of steam (or even compute them, with the model of Ch. 4) values for the rest of the parameters as $\rho_0 = 0.322\,\text{kg/m}^3$,

[1] Here, we follow the notation of the original work of Rothe (1971), who defined the Reynolds number based on the throat radius. It is more common in literature for it to be expressed in terms of the throat diameter, instead.

$H_0 = 3278.23\,\mathrm{kJ\,kg^{-1}}$ and $\mu_0 = 2.44\,\mathrm{Pa \cdot s}$. These yield an estimated minimum "Rothe's" Reynolds number for the micronozzles of this work as $B = 1520$.

In Rothe's work, the most comprehensively documented nozzle operated at B =590, a value roughly 2.5 times lower. Being significantly more rarefied, that flowcase can provide a conservative impression on the model's ability to reproduce low density flows and is therefore used here.

Before the comparison is performed, it is preferable to convert the estimate of the Reynolds number to the more familiar form based on the approximate conditions at the throat, such that the comparisons can easily be done with other cases in this work and other works in literature, if needed [2]. A rough estimate can be obtained from quasi-1D isentropic nozzle theory. The Reynolds number is formally defined as (Sutton and Biblarz, 2017):

$$Re_t = \frac{\rho U L}{\mu} \tag{3.16}$$

where ρ, U and μ are the gas density, velocity and viscosity, respectively and L is a reference length taken here as the throat width (note: no longer the half-width). For micronozzles exhibiting a rectangular cross section, such as the ones of interest in this work, the Reynolds number may be reformulated as:

$$Re_t = \frac{\dot{m}}{\mu \cdot d} \tag{3.17}$$

where d is the nozzle depth and $\dot{m}$ is the mass flow corresponding to a chocked-throat condition. The mass flow can also be approximated with the same theoretical framework:

$$\dot{m} = \frac{p_0 A^*}{T_0} \sqrt{\frac{\gamma}{R} \left(\frac{2}{\gamma + 1} \right)^{(\gamma+1)/(\gamma-1)}} \tag{3.18}$$

with p_0 and T_0 being the stagnation pressure and temperature, A^* being the nozzle throat area, R the specific gas constant and γ the ratio of specific heat capacities of the gas. Moreover, to estimate the viscosity at the throat, an estimate of the throat temperature is needed, which may also follow from isentropic theory as:

$$\frac{T_0}{T_t} = 1 + \frac{\gamma - 1}{2} M_t^2 \tag{3.19}$$

where T_t and M_t denote the temperature and the Mach number at the throat, the latter being unity for a chocked supersonic flow.

Furthermore, for water, one may also take R =461.52 $\mathrm{J\,kg^{-1}\,K^{-1}}$ and $\gamma = 1.33$, as well as a viscosity $\mu \approx 2 \times 10^{-5}\,\mathrm{Pa \cdot s}$ at $T_t \approx 578\,\mathrm{K}$. These values give a minimum expected Reynolds number of $Re_t = 573$. Following the same procedure for the nitrogen flow in Rothe's nozzle, using the data from Table 3.1, one finds $Re_t \approx 270$ at sonic conditions, which shows the nozzle was substantially more rarefied than what is being treated here. The attention is now turned to the numerical check itself.

The selected nozzle in Rothe (1971) was of the axisymmetric type and relatively small, spanning roughly 6 cm in length and exhibiting a nozzle throat radius of 2.55 mm. The precise geometry is depicted in Fig. 3.3 and the flow case specifications are listed in Table 3.1.
The simulation was run on a 75k cell mesh, shown in Fig. 3.4. The stagnation conditions as given in the original work are assigned at the inlet. An isothermal wall fixed at 300 K is assumed, on which the slip condition of Gokcen is imposed. The rest of the numerical setup is as described in Ch. 6, which treats the numerics for the entirety of this work.

[2] Do note, however, that Rothe's definition of the Reynolds number is an accurate representation of reality, because the conditions at the stagnation chamber do not depend on the nozzle characteristics. Instead, a 3D planar micronozzle is not an isentropic flowcase, so the value of Re estimated by ideal rocket theory based on the conditions at the throat is only a rough approximation.

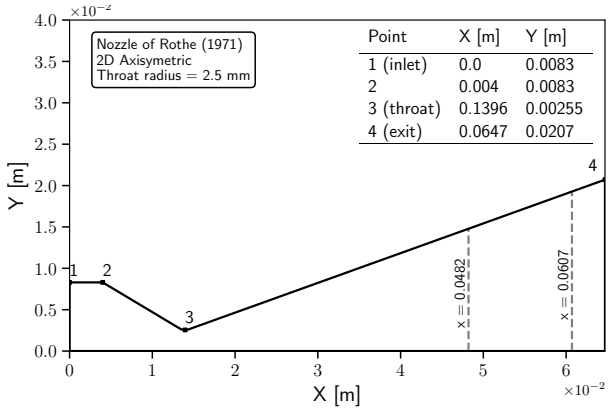

FIGURE 3.3: Geometry of the nozzle of Rothe (1971). The dotted lines indicate the locations at which Rothe took measurements in the radial direction.

Table 3.1: Main parameters for the selected experiment from the work of Rothe (1971)

Parameter	Value
Propellant	Nitrogen (N_2)
Stagnation pressure	473 Pa
Stagnation temperature	300 K
Ambient pressure	1.53 Pa
Ambient temperature	300 K
Wall temperature	300 K
Reynolds number	270

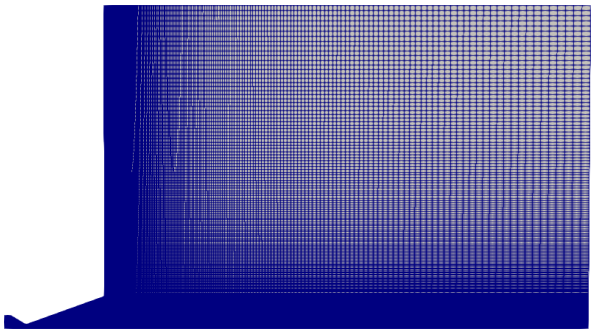

FIGURE 3.4: Computational mesh of the nozzle of Rothe (1971). The flow case is modelled as 2D axisymetric.

Some data is needed for the thermodynamics of Nitrogen. It is modelled as an ideal gas with a specific gas constant of $R = 296.8\,\mathrm{J\,kg^{-1}\,K^{-1}}$. The isobaric specific heat is computed according to the JANNAF polynomial formulation (McBride et al., 1993):

$$C_p = R((((\alpha_4 T + \alpha_3)T + \alpha_2)T + \alpha_1)T + \alpha_0) \tag{3.20}$$

and expressed in $\mathrm{J\,kg^{-1}\,K^{-1}}$. The original JANNAF formulation is only valid down to 200 K, but the range was extended in a recent work by Ganani (2019) to less than 100 K, by means of a numerical fit to the data of Span et al. (2000). The new coeffcicients follow as:

- $\alpha_0 = 3.497$
- $\alpha_1 = 1.365 \cdot 10^{-4}$
- $\alpha_2 = -1.232 \cdot 10^{-6}$
- $\alpha_3 = 3.315 \cdot 10^{-9}$
- $\alpha_4 = -1.792 \cdot 10^{-12}$
- $\alpha_5 = -1.044 \cdot 10^{3}$
- $\alpha_6 = 3.107$

The last two coefficients, α_5 and α_6 serve as the integration constants that result when one integrates the isobaric specific heat to determine the enthalpy and entropy, respectively. The viscosity is modelled as a function of the gas temperature T after the common and simple model of Sutherland (1893):

$$\mu = \frac{A_s \sqrt{T}}{1 + T_s/T} \tag{3.21}$$

To stay consistent with past work in the department, the reference viscosity and temperature are also adopted from the work of Ganani (2019) as A_s =1.4067 $\times$ 10^{-6} Pa $\cdot$ s and $T_s = 111$ K. The precise value of these constants varies slightly between different works in literature.

The output flowfield of the simulation is sampled for the gas density and temperature along the centerline (from the nozzle throat to slightly downstream of the exit), as well as the most downstream of the two radial locations for which Rothe provided data, as shown in Fig. 3.3. The latter selection was made because the degree of rarefaction in nozzles is typically highest closest to the wall and near the exit. The results of the model are plotted against the experimental data in Fig. 3.5a for the centerline measurements and in Fig. 3.5b for the radial ones. In all instances, the results are normalised by the stagnation values.

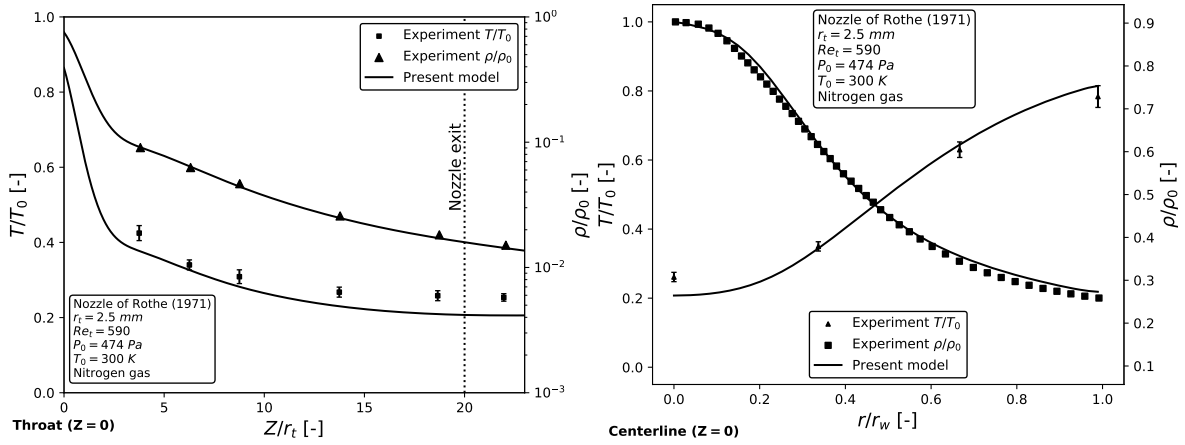

(a) Centerline measurement

(b) Radial measurement at x = 0.0607 m

FIGURE 3.5: Comparison of the single-phase model against the experiments of Rothe (1971)

It can be seen that the solver predicts the density with good accuracy, both along the centerline and in the radial direction near the exit. The latter is appreciable, given the degree of rarefaction typically increases near the nozzle lip. The same cannot be said in the case of the temperature, which is approximated fairly across the radial measurement, but is consistently underpredicted along the centerline. This is partly a manifetation of the fact that the rotational and translational temperatures deviate from each other when rarefaction is present, as shown in the work Chung et al. (1995), who treated the same case. The tendency of the model to underpredict the temperature appears to be typical of Navier-Stokes based solvers, in general (Ivanov et al., 1998; Arlemark et al., 2012).

In any case, the offset is not dramatic (roughly 15% at maximum) and since the modelled experiment is substantially more rarefied than what is treated in the present work, it is fair to assume that the tool will perform with suitable accuracy at higher Reynolds numbers. This is also indicated in the second validation case, presented next.

3.5.2 Experiments of Cen et al.

The experiments of Cen and Xu (2010) treated superheated water vapour flow through a micronozzle geometry loosely comparable to the ones that are of interest in the present work, exiting into a low pressure ambient inside a vacuum chamber. Their work therefore provides a suitable validation case to check if the single-phase model performs well also when hot water, rather than cold nitrogen, is involved. The only inconvenience is that their ambient pressure was at 500 Pa, substantially higher than the 30 Pa that is used in this work and, of course, not quite vacuum. However, the ability of the model to reproduce low-density flows was tested in the previous section and the main purpose here is to ensure its performance is not affected by the particular thermodynamics of water vapour or the presence of hot walls.

Cen and Xu (2010) ran a wide variety of experiments at an array of mass flows and heater temperatures. For the sake of brevity, only one case is treated here, selected for its similarity to the flowcase that in Ch. 6 will be set as the baseline flowcase of the present work. In the original authors' work, it is sometimes unclear whether the pressure/temperature values they list are stagnation or static conditions. It is inferred, based on the general description, that they are likely stagnation conditions and as such they are used here. So, for this validation simulation:

- Stagnation pressure/temperature are set at the inlet, as $P_0 = 1\,\text{bar}$ and $T_0 = 453.15\,\text{K}$ (180 °C).
- The wall is assumed to be isothermal, fixed at the stagnation temperature (for a motivation on this, see Sec. 6.4.1).
- At the exit, supersonic conditions are imposed, except for the subsonic portions where a total pressure is set at 500 Pa. The quiescent ambient is assumed to be at room temperature (293 K).
- All thermodynamic properties are computed as described in Ch. 4.
- The rest of the numerical setup is as described in Ch. 6.

The nozzle geometry and the corresponding computational domain are depicted in Fig. 3.6. The 3D mesh used had roughly 100000 cells, with 40 cells in the width and 20 cells in the depth direction, to sufficiently resolve the boundary layers building along the respective walls. The outlet spans a distance equal to 8 exit widths downstream and 4 exit widths in the width and depth directions.

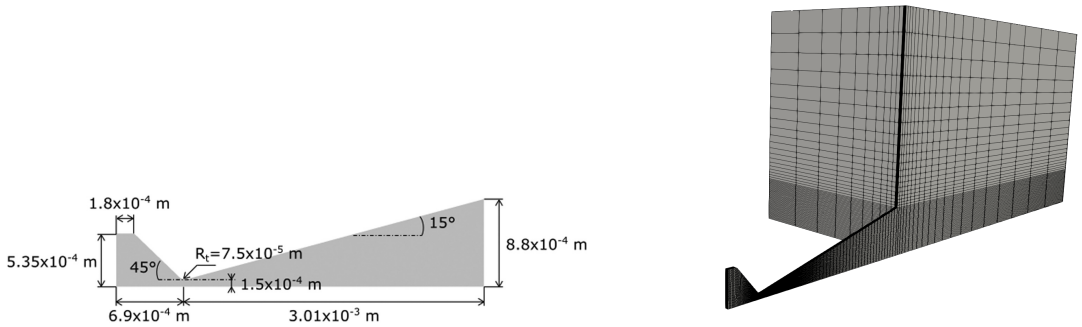

(a) Nozzle geometry (Giorgi and Fontanarosa, 2019b)

(b) Computational domain

FIGURE 3.6: Geometry and computational mesh of the nozzle of Cen and Xu (2010). The figure on the left has been extracted from Giorgi and Fontanarosa (2019b).

The experiments of Cen and Xu (2010) were not concerned with the detailed flow topology and only provided macroscopic performance parameters. These are compared to the simulation results in Table 3.2. It is seen that the model is in remarkable agreement with measurements, reproducing the experimental results very closely. The Reynolds number for this nozzle can be computed with the data

Table 3.2: Comparison between model predictions and experimental measurements for the nozzle of Cen and Xu (2010)

Parameter [Unit]	Experiment	Model	Offset
Mass flow [mg/s]	140	139.14	0.6 %
Thrust [mN]	1.97	1.95	1 %
Specific Impulse [s]	85.9	85.7	0.3 %

above as $Re_t \approx 4280$, which clearly shows what a difference in the rarefaction of the nozzle flow the higher ambience pressure of 500 Pa makes.

Perhaps a comparison is due here with the work of Giorgi et al. (2018), who used the same solver to simulate the same experiments, although at different inlet values. They employed different types of boundary conditions, did not account for the heat input from the wall or the temperature jump at the interface with the fluid and used a thermodynamic model based on the Peng-Robinson equation of state (Lopez-Echeverry et al., 2017). Their results were roughly $10\,\%$ off or more from experiments, which illustrates the validity of the present approach.

In view of the above, the single-phase model is considered validated.

Part II

Thermodynamics of water

CHAPTER 4

Thermodynamic properties of (supercooled) steam and water

As was mentioned earlier that the evolution of thermodynamic properties of steam under non-equilibrium expansion conditions departs markedly from those of an ideal gas (Reisel, 2015). At low pressures and high temperatures the difference is usually not much more than 1-2 %, but this offset deteriorates as the vapour moves closer to its saturated state. A real-gas model is therefore necessary and this section serves to outline the methodology followed for its implementation in this work.

4.1 Preliminary remarks

The real-gas description of steam in stable and metastable states typically follows from a long sequence of empirical relations and algebraic manipulations, that are usually compiled by fitting numerical approximations to large volumes of experimental data. Thermodynamic computations involving water in liquid and gaseous form are widespread enough in science and industry to have warranted the establishment of the International Association for the Properties of Water and Steam (IAPWS), whose 1995 and 1997 formulations for general scientific and industrial use, respectively, currently serve as the standard (Wagner et al., 2000; Wagner and Pruß, 2002). These formulations and various subsequent minor revisions constitute the state-of-the-art in terms of accuracy, however they extract a very heavy computational toll, because they are based on a multitude of high-order and high-complexity polynomials that have to be evaluated separately for every cell of the computational domain and for every timestep of the simulation.

To partially remedy this in this work, a large portion of the thermodynamic properties are instead evaluated based on an equation of state of the Virial form, complemented by transport and liquid properties computed with the help of suitable approximations to the IAPWS model and other sources. The present implementation is still multiple times more computationally intensive than a model based on the ideal gas assumption, but offers a reduction in computational time of at least one order of magnitude relative to the full IAPWS formulation, at a virtually insignificant loss of accuracy[1]. Heavy emphasis has been placed on further reducing this cost via methods that are presented in the following sections.

The major limitation of the Virial and the IAPWS formulations is that they are only valid for temperatures $\geq 273.16\,\mathrm{K}$. As explained in Sec. 2.5, the extreme cooling rates are expected to drive the vapor to temperatures well below this threshold before any condensation occurs. This presents a significant complication, because there appears to be no framework whatsoever to quantify the properties of water and steam in these temperatures, nor is there any substantial range of data to help create one. Extrapolation is in most cases not an option, because it is shown later that the Virial and the IAPWS formulation are poorly behaved outside their range of validity. Other equations of state found in literature were also tested and gave similar results. The author was left with little option but to

[1]The loss of accuracy is "insignificant" for our purposes only. The IAPWS formulation has been originally compiled to serve the most demanding of scientific requirements in terms of accuracy and its full level of precision is not needed in the present engineering application.

assume that the vapour can be described with sufficient accuracy by the ideal gas law. The rest of the thermodynamic parameters are then approximated via this law and theoretical considerations of statistical thermodynamics found in literature. The liquid properties are similarly described by a series of empirical equations assembled from various sources in literature or produced for the purposes of this work. While there is no way to validate these, it is explained later that there are good reasons to believe they are not far from reality.

Accordingly, the structure of this chapter is divided into two halves. The first portion treats the thermodynamics above the freezing point and the second below it. In each instance, the following types of data are given:

- Equation of state, vapour enthalpies, specific heats and associated properties
- Tranport properties: viscosity, conductivity and thermal diffusivity
- Properties at saturation: pressure, temperature and density
- Liquid properties: Density, enthalpy, surface tension, etc

The numerical implementation of some of these is also briefly described.

As a last note, the relations presented in this chapter appear in literature in various forms, occasionally containing typographical errors, erroneous derivations or dimensional inconsistencies. Where applicable, the mistakes found are pointed out and the equations are given here in their corrected version and in a form such that both inputs and outputs are in plain SI units, across the full thermodynamic model.

4.2 Basic equation of state

The equation of state (EoS) used here is the one derived by Vukalovitch (1958), in the form given later by Gerber and Kermani (2004). There are multiple EoSs given in literature and the main reason of choice of this particular one is its demonstrated robustness in the supercooled regime. Equations of state (as well as the IAPWS framework) are derived with equilibrium conditions in mind and most of them are unsuitable in metastable states. Bakhtar and Piran (1979) showed that Vukalovich's EoS reproduces data with negligible error, even for supercoolings of -40 or $-50\,°C$ relative to the local saturation temperature and authors such as Gerber and Kermani (2004) have successfully used it for condensation studies. Its range of validity, as for all properties in this first part of the chapter, is $0.01\,\text{bar} \leq p \leq 100\,\text{bar}$ and $273.16\,K \leq T \leq 1073.16\,K$. In the flow cases of this work, the pressure in the nozzle will not drop below 0.01 bar inside the micronozzle. It does so at the outlet downstream of the nozzle exit, where its properties are estimated by extrapolation.

The equation is given by:

$$p = \rho_g R T_g (B_1 + B_2 \rho_g + B_3 \rho_g^2 + B_4 \rho_g^3) \tag{4.1}$$

The subscript g denotes properties of the vapour and p, ρ, T and R are, respectively, the pressure, density, temperature and specific gas constant. The B_i terms are the Virial coefficients. They are a solely dependent on temperature and each carries its own dimensions. They follow successively as:

$$B_1 = 1 \quad [-] \tag{4.2}$$

$$B_2 = -\frac{e}{G T_g} - \phi_1 + b \quad [m^3/kg] \tag{4.3}$$

$$B_3 = -b\phi_1 + 4\phi_1^2\phi_2 \quad [m^6/kg^2] \tag{4.4}$$

$$B_4 = 32b\phi_1^2\phi_2 \quad [m^9/kg^3] \tag{4.5}$$

with empirical parameters:

$$\phi_1 = \frac{CG}{T_g^{(3+2m1)/2}} \quad \& \quad \phi_2 = 1 - \frac{22.7}{T_g^{(3m_2-4m_1)/2}} \tag{4.6}$$

where the constants are given by:

$$e = 63.2,\ b = 0.00085,\ C = 0.39 \cdot 10^6,\ G = 47.053,\ m_1 = 1.968,\ m_2 = 2.957 \tag{4.7}$$

For the subsequent computation of the enthalpy and specific heats, the first and second derivatives of the Virial coefficients with respect to temperature are needed. These have been derived below for the reader's convenience:

$$\frac{dB_2}{dT} = \frac{e}{G}T^{-2} + CGw_1T^{-w_1-1} \tag{4.8}$$

$$\frac{d^2B_2}{dT^2} = -\frac{2e}{G}T^{-3} - CGw_1(w_1+1)T^{-w_1-2} \tag{4.9}$$

$$\frac{dB_3}{dT} = bw_1CGT^{-w_1-1} - 8w_1C^2G^2T^{-2w_1-1}(1 - 22.7T^{-w_2}) + 4C^2G^2T^{-2w_1}(22.7w_2T^{-w_2-1}) \tag{4.10}$$

$$\begin{aligned}\frac{d^2B_3}{dT^2} =& - bw_1(w_1+1)CGT^{-w_1-2} \\ &+ 8w_1(2w_1+1)C^2G^2T^{-2w_1-2}(1 - 22.7T^{-w_2}) \\ &- 8w_1C^2G^2T^{-2w_1-1}(22.7w_2T^{-w_2-1}) \\ &- 8w_1C^2G^2T^{-2w_1-1}(22.7w_2T^{-w_2-1}) \\ &- 4C^2G^2T^{-2w_1}\left[22.7w_2(w_2+1)T^{-w_2-2}\right]\end{aligned} \tag{4.11}$$

$$\begin{aligned}\frac{dB_4}{dT} =& - 32bC^2G^2 2w_1T^{-2w_1-1}(1 - 22.7T^{-w_2}) \\ &+ 32bC^2G^2T^{-2w_1}(22.7w_2T^{-w_2-1})\end{aligned} \tag{4.12}$$

$$\begin{aligned}\frac{d^2B_4}{dT^2} =& + 32bC^2G^2 2w_1(2w_1+1)T^{-2w_1-2}(1 - 22.7T^{-w_2}) \\ &- 32bC^2G^2 2w_1T^{-2w_1-1}(22.7w_2T^{-w_2-1}) \\ &- 32bC^2G^2 2w_1T^{-2w_1-1}(22.7w_2T^{-w_2-1}) \\ &- 32bC^2G^2T^{-2w_1}(22.7w_2(w_2+1)T^{-w_2-2})\end{aligned} \tag{4.13}$$

where $w_1 = (3 + 2m_{1)}/2$ and $w_2 = (3m_2 - 4m_1)/2$ and the rest of the parameters have been previously presented.

4.3 Vapour thermodynamic properties

The rest of the thermodynamic parameters to describe the state of the water vapour may be derived from the Vukalovich equation, augmented with empirical factors. The first two of the following relations have been extracted from Bakhtar and Piran (1979), but have been corrected here for some typographical errors. The rest are derived according to basic thermodynamic relations.

Absolute specific enthalpy [J/kg]:

$$\begin{aligned} h_g = pv_g - RT_g^2 \left(\frac{1}{v_g}\frac{dB_2}{dT_g} + \frac{1}{2v_g^2}\frac{dB_3}{dT_g} + \frac{1}{3v_g^3}\frac{dB_4}{dT_g} \right) \\ + 1.111177T_g + 3.55878 \cdot 10^{-4}T_g^2 - \frac{6991.96}{T_g} + 2070.54 \end{aligned} \tag{4.14}$$

Isochoric specfic heat [J/(Kg.K)]:

$$\begin{aligned} C_{v_g} = \frac{\partial}{\partial T_g}(h_g - pv_g)_{v_g} =& 10^{-3} \left\{ -2RT_g \left[\frac{1}{T} \left(\frac{1}{v_g}\frac{dB_2}{dT_g} + \frac{1}{2v_g^2}\frac{dB_3}{dT_g} + \frac{1}{3v_g^3}\frac{dB_4}{dT_g} \right) \right.\right. \\ & \left.\left. + \frac{1}{2} \left(\frac{1}{v_g}\frac{d^2B_2}{dT_g^2} + \frac{1}{2v_g^2}\frac{d^2B_3}{dT_g^2} + \frac{1}{3v_g^3}\frac{d^2B_4}{dT_g^2} \right) \right] \right. \\ & \left. + 1.111177 + 0.00071T_g + \frac{6991.96}{T_g^2} \right\} \end{aligned} \tag{4.15}$$

Isobaric specfic heat [J/(Kg.K)]:

$$\begin{aligned} C_{p_g} &= C_{v_g} - \frac{T_g(\partial p/\partial T_g)_{v_g}^2}{(\partial p/\partial v_g)_{T_g}} \\ &= C_{v_g} - \frac{T_g \left[R\left(\frac{B_1}{v_g} + \frac{B_2}{v_g^2} + \frac{B_3}{v_g^3} + \frac{B_4}{v_g^4} \right) + RT\left(\frac{1}{v_g}\frac{dB_1}{dT} + \frac{1}{v_g^2}\frac{dB_2}{dT} + \frac{1}{v_g^3}\frac{dB_3}{dT} + \frac{1}{v_g^4}\frac{dB_4}{dT} \right) \right]^2}{-RT\left(\frac{B_1}{v_g^2} + \frac{2B_2}{v_g^3} + \frac{3B_3}{v_g^4} + \frac{4B_4}{v_g^5} \right)} \end{aligned} \tag{4.16}$$

Compressibility factor:

$$Z = \frac{p}{\rho RT} = B_1 + B_2\rho + B_3\rho^2 + B_4\rho^3 \tag{4.17}$$

Compressibility ratio:

A numerically convenient correction factor to account for the departure of the real gas from ideal behaviour is given by:

$$\psi = \frac{1}{ZRT_g} \tag{4.18}$$

Speed of sound in water vapour:

$$C_g = v_g \sqrt{-\frac{C_{p_g}}{C_{v_g}} \left(\frac{\partial p}{\partial v_g} \right)_{T_g}} = v_g \sqrt{\frac{C_{p_g}}{C_{v_g}} RT \left(\frac{B_1}{v_g^2} + \frac{2B_2}{v_g^3} + \frac{3B_3}{v_g^4} + \frac{4B_4}{v_g^5} \right)} \tag{4.19}$$

Specific heat ratio/Isentropic exponent:

$$\gamma = \frac{\rho}{p}\left(\frac{\partial p}{\partial \rho} \right)_s = \frac{\rho}{p}\frac{C_p}{C_v}\left(\frac{\partial p}{\partial \rho} \right)_{T_g} = \frac{\rho}{p}\frac{C_p}{C_v} RT(B_1 + 2B_2\rho + 3B_3\rho^2 + 4B_4\rho^3) \tag{4.20}$$

By replacing Eqns. 4.18, 4.20 into 4.19, the speed of sound may be expressed more simply as:

$$C_g = \sqrt{\frac{\gamma}{\psi}} \tag{4.21}$$

Specific gas constant:

The last parameter needed to close the above system of equations is the specific gas constant for water vapour, which in this work takes the value:

$$R = \frac{\mathcal{R}}{M_{molar}} = 461.51 \ \frac{J}{kg \cdot s} \tag{4.22}$$

where $M_{molar} = 0.018\,015\,28\,\text{kg/mol}$ is the molar mass of water and $\mathcal{R} = 8.314\,\text{J}/(\text{kg} \cdot \text{mol})$ is the universal gas constant.

4.3.1 Gibbs free energy

A major thermodynamic parameter that emerges in condensation studies (Sec. 5.3) is the specific Gibbs free energy, often also referred to as free enthalpy. It qualitatively signifies the amount of energy under constant pressure and temperature conditions that is available in the system for work in a reversible thermodynamic process (Perrot, 1998) and emerges in the model of the nucleation process. The parameter is formally related to the enthalpy and entropy of the system as:

$$G = U - TS + pV \tag{4.23}$$

where U and S here denote the specific internal energy and entropy, respectively, T is the temperature and the sum $U+pV$ expresses the enthalpy in the system. In this context, the change in G is of interest and it is associated with the surface energy (in turn related to the surface tension) that is to be invested in the emergence of the liquid surface that leads to the formation of the droplet. This is elaborated upon in Sec. 5.3. When a Virial equation of state is used, the expression for the change in Gibbs free energy is extended to account for the real gas effects and given by (in J/Kg):

$$\Delta G = RT_G \left\{ -ln\frac{\rho_g}{\rho_s(T_g)} + 2B_2[\rho_s(T_g) - \rho_g] + \frac{3}{2}B_3[\rho_s^2(T_g) - \rho_g^2] + \frac{4}{3}B_4[\rho_s^3(T_g) - \rho_g^3] \right\} \tag{4.24}$$

where $\rho_s(T_g)$ is the saturated vapour density at the local vapour temperature, obtained as described in Sec. 4.5.3 and R is the specific gas constant.

Due to the particular architectural construction of the thermodynamic framework in OpenFOAM, computing this expression would require either evaluating the Virial coefficients twice in the same iteration or a thorough reconstruction of this framework. The former option induces a significant computational overhead during the code execution, while the latter option would require an extensive coding effort, on top of the already quite extensive procedure it took to implement the model described in this chapter. To avoid these issues, it was decided to use a simplified version of Eqn. 4.24, given by:

$$\Delta G \approx RT_G ln\left(\frac{P}{P_{sat}}\right) \tag{4.25}$$

This is essentially the ideal-gas form, but for the low pressures treated here it provides an excellent approximation with a negligible error (typically less than 1%).

4.4 Vapour transport properties

The solution of the Navier-Stokes equations, as well as a number of other parameters in this work, require expressions for the gas dynamic viscosity, the thermal conductivity and the thermal diffusivity, descibing respectively the transport of momentum and energy. Such expressions have here been taken directly from the IAPWS formulation as described in Huber et al. (2009) and have been simplified, to reduce the computational expense.

4.4.1 Vapour dynamic viscosity:

The formulation derived by Huber et al. (2009) is valid for gaseous and liquid states alike and follows as:

$$\bar{\mu} = \bar{\mu}_0(\bar{T}) \cdot \bar{\mu}_1(\bar{T}, \bar{\rho}) \cdot \bar{\mu}_2(\bar{T}, \bar{\rho}) \tag{4.26}$$

In this expression, $\bar{\mu}_0(\bar{T})$ denotes the viscosity at the dilute-gas limit, $\bar{\mu}_1(p,\bar{T})$ introduces the dependency to pressure and $\bar{\mu}_2(\bar{T})$ is a correction to capture the particular behaviour of water vapour in the vicinity of the critical point. The overhead bar notation is to signify that these are in fact non-dimensional quantities, given by:

$$\bar{\mu} = \frac{\mu}{\mu^*} \qquad \bar{T} = \frac{T}{T^*} \qquad \bar{\rho} = \frac{\rho}{\rho^*} \tag{4.27}$$

where $\mu^* = 1 \times 10^{-6}\,\mathrm{Pa \cdot s}$, $T^* = 647.096\,\mathrm{K}$ and $\rho^* = 322\,\mathrm{kg/m^3}$. The critical point ($p = 22.064\,\mathrm{MPa}$, $T = 647.096\,\mathrm{K}$) is far outside the scope of interest here, so the right-most term can be neglected. The other two terms follow as:

$$\bar{\mu}_0(\bar{T}) = \frac{100\sqrt{\bar{T}}}{\sum_{i=0}^{3} \frac{H_i}{\bar{T}^i}} \tag{4.28}$$

with coefficients:

- $H_0 = 1.67752$
- $H_1 = 2.20462$
- $H_2 = 0.6366564$
- $H_3 = -0.241605$

and:

$$\mu_1(T, \rho) = exp\left[\rho_g \sum_{i=0}^{5} \left(\frac{1}{T_g} - 1\right)^i \sum_{j=0}^{6} H_{ij}(\rho_g - 1)^j\right] \tag{4.29}$$

This latter expression features more than 20 coefficients (not given here for the sake of brevity, but listed in the original reference) and it is readily understood that it comes at a heavy computational expense. The pressures treated in this work do not exceed 5 bar (0.5 MPa), while the greatest portion of the flow as it expands in the convergent and divergent of the nozzle is expected to be well below 1 bar. Furthermore, only the viscosity of the vapour state is of interest here. On these grounds, the assumption is made that the dilute-gas approximation is a valid one, such that the viscosity may be given exclusively by Eqn. 4.28 at only a small loss of accuracy. To ensure this is the case, the results are compared to the full model at a selection of pressures and temperatures in Table. 6.1. It can be seen that the offset is already less than 2% in the highest pressure and rapidly drops to less than 1% as the pressure decreases. This simplification is therefore accepted here.

Table 4.1: Comparison of reference viscosity datapoints with the present model's predictions

Temperature [K]	Pressure [bar]	Viscosity (IAPWS) [Pa·s]	Viscosity (Model) [Pa·s]	Offset [%]
450	5	1.5089×10^{-5}	1.5313×10^{-5}	1.4
420	3	$1.395\,57 \times 10^{-5}$	$1.412\,94 \times 10^{-5}$	1.2
373	1	$1.226\,48 \times 10^{-5}$	$1.233\,14 \times 10^{-5}$	0.5
320	0.1	1.0519×10^{-5}	$1.043\,16 \times 10^{-5}$	0.8

4.4.2 Vapour thermal conductivity

The same discussion applies as in the case of viscosity. Without being repetitive, the heat conductivity in this work is assumed to be the one at the dilute limit, given by Huber et al. (2009) as:

$$\bar{k}_0(\bar{T}) = \frac{\sqrt{\bar{T}}}{\sum_{k=0}^{4} \frac{L_k}{\bar{T}^k}} \tag{4.30}$$

with coefficients:

- $L_0 = 2.443221 \cdot 10^{-3}$
- $L_1 = 1.323095 \cdot 10^{-3}$
- $L_2 = 6.770357 \cdot 10^{-3}$
- $L_3 = -3.454586 \cdot 10^{-3}$
- $L_4 = 4.096266 \cdot 10^{-4}$

and $\bar{k_0} = k/k^*$, where $k^* = 1 \times 10^{-3}\,\mathrm{W/(m \cdot K)}$. The loss in accuracy is comparable to the one in the viscosity case.

4.4.3 Vapour thermal diffusivity

This parameter follows simply as (expressed in $\mathrm{m^2/s}$):

$$\alpha = \frac{k}{\rho \cdot C_p} \tag{4.31}$$

where k, ρ and C_p are the thermal conductivity, density and isobaric heat capacity of the water vapour, respectively. The product $\rho \cdot C_p$ corresponds to the vapour's volumetric heat capacity, expressed in $\mathrm{J/(m^3 \cdot K)}$.

4.5 Saturation properties

The pressure, temperature and density at saturation are driving parameters in this study and their accurate estimation is of primary importance. For this reason, they have been adopted directly from the IAPWS formulation, as described in Cooper (2007). In the early stages of this work, the commonly used saturation curve by Keenan et al. (1969) was implemented but turned out to be numerically inconvenient, because its formulation relies on complex derivatives of the pressure that are extremely sensitive to small variations in temperature[2].
The expressions below are valid in the range 273.16-647.096 K. The value of 647.096 K corresponds to the temperature at the critical point, above which the phase state of water is purely gaseous and saturation is not applicable. A separate formulation is given in Sec. 4.8 for the properties below the freezing point. For all expressions that follow, the cited works provide sample data for computer verification, which has been used to ensure the expressions are correctly implemented, down to the last decimal.

4.5.1 Saturation pressure

The IAPWS equation for the saturation pressure as a function of the local temperature is given by the following empirical equation:

$$p_s(T) = p^* \cdot \left[\frac{2C}{-B + (B^2 - 4AC)^{1/2}} \right]^4 \tag{4.32}$$

where $p^* = 1\,\text{MPa}$ and:

$$A = \theta^2 + n_1\theta + n_2$$

$$B = n_3\theta^2 + n_4\theta + n_5$$

$$C = n_6\theta^2 + n_7\theta + n_8$$

$$\theta = \frac{T}{T^*} + \frac{n_9}{(T/T^*) - n_{10}}$$

with $T^* = 1\,\text{K}$ and the following coefficients:

- $n_1 = 0.11670521452767 \cdot 10^4$
- $n_2 = -0.72421316703206 \cdot 10^6$
- $n_3 = -0.17073846940092 \cdot 10^2$
- $n_4 = 0.12020824702470 \cdot 10^5$
- $n_5 = -0.32325550322333 \cdot 10^7$
- $n_6 = 0.14915108613530 \cdot 10^2$
- $n_7 = -0.48232657361591 \cdot 10^4$
- $n_8 = 0.40511340542057 \cdot 10^6$
- $n_9 = -0.23855557567849$
- $n_{10} = 0.65017534844798 \cdot 10^3$

4.5.2 Saturation temperature

The saturation temperature at the local pressure is the inverse of Eqn. 4.32 and as such it is derived. It follows as:

[2] In case this is of relevance to the interested reader, the original work of Keenan et al. (1969) is not - at the time of this writing - available in electronic form and one is likely to gain access to its saturation curve equation indirectly via the work of Young (1988). Note that the latter reference contains a typographical error and the term inside the sum in that paper's Eqn. 27 should instead read $(3.3815 - 0.01T)$.

$$T_s(p) = T^* \cdot \frac{n_{10} + D - \left[(n_{10} + D)^2 - 4 \cdot (n_9 + n_{10} D)\right]^{1/2}}{2} \tag{4.33}$$

where:

$$D = \frac{2G}{-F - (F^2 - 4EG)^{1/2}}$$

$$E = \beta^2 + n_3 \cdot \beta + n_6$$

$$F = n_1 \beta^2 + n_4 \beta + n_7$$

$$G = n_2 \beta^2 + n_5 \beta + n_8$$

$$\beta = \left(\frac{p}{p^*}\right)^{1/4}$$

and coefficients as given in Sec. 4.5.1.

4.5.3 Saturation density

The expression for the saturated density has to be extracted from a separate source, that of Wagner and Pruß (2002), but it is thermodynamically consistent with the saturation pressure described by Eqn. 4.32. It follows as a function of the local temperature:

$$\rho_s(T) = \rho_c \cdot exp\left[c_1 \theta^{2/6} + c_2 \theta^{4/6} + c_3 \theta^{8/6} + c_4 \theta^{18/6} + c_5 \theta^{37/6} + c_6 \theta^{71/6}\right] \tag{4.34}$$

where:

- $\rho_c = 322\,\mathrm{kg/m^3}$
- $T_c = 647.096\,\mathrm{K}$
- $\theta = 1 - T/T_c$
- $c_1 = -2.03150240$
- $c_2 = -2.68302940$
- $c_3 = -5.38626492$
- $c_4 = -17.2991605$
- $c_5 = -44.7586581$
- $c_6 = -63.9201063$

This expression concludes the determination of the saturation properties.

4.6 Liquid phase properties

The thermodynamic properties of liquid water to be evaluated for the needs and purposes of this work are the density, enthalpy and surface tension. The IAPWS formulation provides relatively simple and straightforward expressions, so it is also used here. It is assumed in this work that the liquid properties are a function of temperature only. All outputs are in plain SI units. All formulas have been checked against benchmark results from the original publications to ensure they are reproduced correctly, down to the last decimal.

4.6.1 Liquid density

Based on the assumed independence from pressure, it is also assumed that the liquid density can be sufficiently described by its value at saturation. The expression is of the same form as that of saturated vapor:

$$\rho_l(T) = \rho_c \cdot exp\left[1 + b_1\theta^{1/3} + b_2\theta^{2/3} + b_3\theta^{5/3} + b_4\theta^{16/3} + b_5\theta^{43/3} + b_6\theta^{110/3}\right] \tag{4.35}$$

where:

- $\rho_c = 322\,\mathrm{kg/m^3}$
- $T_c = 647.096\,\mathrm{K}$
- $\theta = 1 - T/T_c$
- $b_1 = 1.99274064$
- $b_2 = 1.09965342$
- $b_3 = -0.510839303$
- $b_4 = -1.75493479$
- $b_5 = -45.5170352$
- $b_6 = -6.74694450 \cdot 10^5$

4.6.2 Liquid enthalpy

In principle, an expression for the liquid enthalpy can be extracted from the EoS of Vukalovich, based on the classic Clausius-Clapeyron relation. However, it would be based on the first and second derivatives with respect to temperature of the vapour's saturation pressure. A quick look at Eqn. 4.32 is enough to conclude this would result in a very cumbersome expression that would contain dozens of terms dependent on the temperature and would therefore be extremely sensitive to small variations in this parameter, which is not convenient for numerical purposes.

The IAPWS formulation provides polynomial expressions for the liquid enthalpy at saturation, that are straightforward to implement and highly accurate. High accuracy is of importance here, because the liquid enthalpy drives the quantification of the latent heat released upon condensation and is an important parameter in the two-phase model. So, it has been implemented here instead. The same assumption as for the liquid density is made, i.e., that the enthalpy can be sufficiently described by its value at saturation. Adopting the IAPWS expression for the liquid when the Vukalovich equation is used for the gas induces a thermodynamic inconsistency at the region of phase change. However, it was tested that this discrepancy would not cause any particular problems and this is later confirmed in the validation of the two-phase model in Sec. 5.9.

According to the work of Wagner and Pruss (1993), the specific enthalpy of the saturated liquid can be expressed as:

$$h_s = \alpha + \frac{T}{\rho_l}\frac{dp_s}{dT_s} \tag{4.36}$$

where T_g is the local gas temperature and ρ_l is the liquid density given by Eqn. 4.35. An approximation to the saturation pressure is given by:

$$p = p_c \cdot \left\{ exp\left[\frac{T_c}{T} \left(\alpha_1 \tau + \alpha_2 \tau^{1.5} + \alpha_3 \tau^3 + \alpha_4 \tau^{3.5} + \alpha_5 \tau^4 + \alpha_6 \tau^{7.5} \right) \right] \right\} \tag{4.37}$$

such that its derivative dp_s/dT_s may be derived as (following some mathematical manipulation and rearrangement of terms):

$$\frac{dp_s}{dT_s} = -\frac{p_s}{T_g} \cdot \left\{ ln\left(\frac{p_s}{p_c}\right) + \alpha_1 + \frac{3}{2}\alpha_2 \tau^{1/2} + 3\alpha_3 \tau^2 + \frac{7}{2}\alpha_4 \tau^{5/2} + 4\alpha_5 \tau^3 + \frac{15}{2}\alpha_6 \tau^{13/2} \right\} \tag{4.38}$$

with coefficients:

- $\tau = 1 - T/T_c$
- $T_c = 647.096$ K
- $\alpha_1 = -7.85951783$
- $\alpha_2 = 1.84408259$
- $\alpha_3 = -11.7866497$
- $\alpha_4 = 22.6807411$
- $\alpha_5 = -15.9618719$
- $\alpha_6 = 1.80122502$

The auxiliary parameter α in Eqn. 4.36 (not to be confused with the coefficients of Eqns. 4.37 and 4.38) also follows from a polynomial relation as:

$$\alpha = \alpha_0 \left(d_\alpha + d_1 \theta^{-19} + d_2 \theta + d_3 \theta^{4.5} + d_4 \theta^5 + d_5 \theta^{54.5} \right) \tag{4.39}$$

with coefficients:

- $\theta = T/T_c$
- $T_c = 647.096$ K
- $\alpha_0 = 1000$ J/kg
- $d_a = -1135.905627715$
- $d_1 = -5.65134998 \cdot 10^{-8}$
- $d_2 = 2690.66631$
- $d_3 = 127.287297$
- $d_4 = -135.003439$
- $d_5 = 0.981825814$

4.6.3 Surface tension

The value of the surface tension of liquid water in this work is determined at the local vapour temperature from the relation of Petrova (2014) as:

$$\sigma = B\tau^{\mu}(1 + b\tau) \tag{4.40}$$

Its derivative is also of relevance for the droplet growth model later, derived simply as:

$$\frac{d\sigma}{dT} = B\mu\tau^{\mu-1}\left(-\frac{1}{T_c}\right)(1 + b\tau) + B\tau^{\mu}\left(-\frac{b}{T_c}\right) \tag{4.41}$$

where $B = 0.2358 N/m$, $\tau = 1 - T/T_c$, $T_c = 647.096\ ^oK$, $\mu = 1.256$ and $b = -0.625$.

4.7 Interim recap

By this point, expressions have been given for the determination of gaseous and liquid properties in the range 0.01 bar$\leq$ p $\leq$ 100 bar and 273.16 K $\leq$ T $\leq$ 1073.16 K. The remainder of the chapter treats the determination of the same properties in the same pressure range, but for T $\leq$ 273.16 K, for which little to no data exists and approximations have to be made.

4.8 Thermophysical properties below 273 Kelvin

4.8.1 Gaseous properties

Equation of state

As explained previously, the vapour is described by the simple ideal gas law for temperatures below 273 K:

$$p_g = \rho_g R T_g$$

The rest of the gaseous thermodynamic properties have to be derived from empirical expressions either of the specific heats or the enthalpy. In this context, it is easier to start from the isobaric specific heat, because many thermodynamic frameworks use its ideal value as a baseline for the derivation of the real gas form, so some limited numerical data exists. Once this specific heat is known, the enthalpy may be derived by integration as:

$$h_0(T_g) = \int Cp_0(T_g) dT_g + h_c \tag{4.42}$$

where h_c is the resulting constant of integration. The details follow below.

Specific heat

The IAPWS formulation provides an expression for Cp_0 in the form:

$$C_p^0 = -n_3/\tau^2 - \sum_{i=4}^{8} n_i (\gamma_i)^2 e^{-\gamma_i \tau} \left(1 - e^{-\gamma_i \tau}\right)^{-2} \tag{4.43}$$

with coefficients:

- n3 = 3.00632
- n4 = 0.012436
- n5 = 0.97315
- n6 = 1.27950
- n7 = 0.96956
- n8 = 0.24873
- g4 = 1.28728967
- g5 = 3.53734222
- g6 = 7.74073708
- g7 = 9.24437796
- g8 = 27.5075105

It is a cumbersome expression that is numerically expensive to compute and inconvenient to integrate for the determination of the corresponding specific enthalpy. A suitable approximation in a simplified version was therefore sought. A careful examination of the form of the equation indicates that a good approximation may be found in a hyperbolic cosine fit of the original data (recall that $cosh = \frac{e^x + e^{-x}}{2}$, a form loosely comparable to that of Eqn. 4.43). Here, we set $\tau = T/647.286$ and numerically optimise parameters A, B and C such that the expression:

$$C_{p,approx}^0 = A + B * cosh(C\tau) \tag{4.44}$$

constitutes a non-linear least-squares regression to the IAPWS formulation. The resulting constants follow as $A = 1848.8562$, $B = 0.076658$ and $C = 13.333367$ and provide an approximation that is within a 1000th of a percent of the original local IAPWS value, across the full $T_g < 273.16$ temperature range. Indicatively, the two models are compared with two computations from literature, those of Friedman

and Haar (1954) and Tanimura et al. (2010). It can be seen that the offest between them is negligible, less than 0.1% in absolute value.

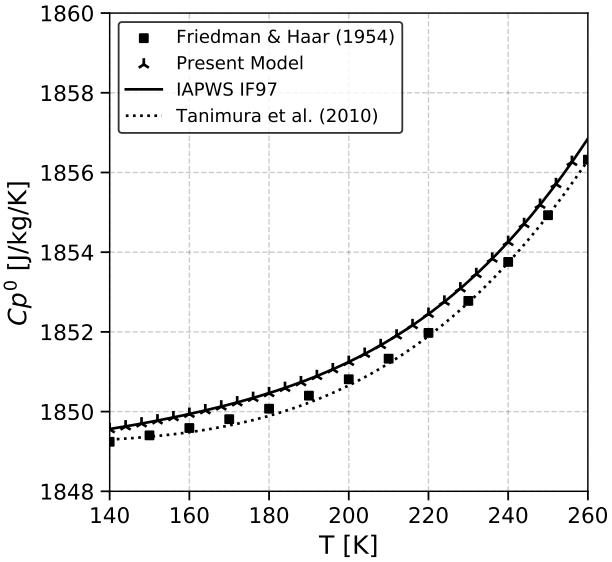

FIGURE 4.1: Variation of the the ideal water vapour specific heat with temperature and comparison with values from literature. There is a virtually exact overlap between the IAPWS and the present models, hence discrete values are given to aid visibility.

Expression 4.43 may then straightforwardly be integrated according to Eqn. 4.42 to yield:

$$h_g^0 = \left[A \cdot T + \frac{647.286 \cdot B}{C} sinh(C\tau)\right]_{T_{ref}}^{T_g} + h_{ref} \tag{4.45}$$

The constant of integration is essentially a reference vapour specific enthalpy at a reference temperature and is up for the user's choice. Here, we follow the NIST-JANNAF convention (Chase, 1998) and select $h_{ref} = 2\,551\,013.479\,\mathrm{J/kg}$ at $T_{ref} = 300\,\mathrm{K}$ (and pressure $p_{ref} = 1\,\mathrm{bar}$).

From there on, the remaining parameters of interest follow simply from the ideal gas assumption as listed below:

$$C_v^0 = C_p^0 - R \tag{4.46}$$

$$Z^0 = 1 \tag{4.47}$$

$$\gamma = \frac{C_p^0}{C_v^0} \equiv f(T_g) \tag{4.48}$$

For the remainder of this work we will dispense with the ^{0} superscript and it is understood that the model for the gas in the dillute limit takes over whenever the gas temperature drops below 273 K.

4.8.2 Transport properties

Viscosity:
The obvious course of action is to extrapolate the IAPWS expression Eqn. 4.28 of Sec. 4.4.1 to the low temperature range. This turns out not to be possible, because Eqn. 4.28 experiences a discontinuity at roughly 135 K and diverges. A better behaved expression may be derived in the commonly used form proposed by Sutherland (1893), but it would be more of a numerical artefact than a physical result. In fact, Sutherland's method is not suitable for a strongly polar molecule such as water, because it is based on an idealized intermolecular-force potential. In a past work, Crifo (1989) derived a series of approximate expressions for the viscosity at very low temperatures to study the physics of cometary tails, but when they were tested by the present author, it was found that none of these agree well with the IAPWS model, even at temperatures $\geq 273.16\,\mathrm{K}$.

Eventually, it was decided to use the IAPWS expression to produce datapoints for $\mathrm{T} \geq 273\,\mathrm{K}$ and then use these datapoints to derive a polynomial expression that maintains smooth monotonic behaviour for $\mathrm{T} \leq 273\,\mathrm{K}$. Essentially, we are extrapolating the IAPWS expression to low temperatures, but in a form that is numerically convenient and avoids discontinuities or other anomalous behaviours. The expression is given by:

$$\mu = c_0 + c_1 T + c_2 T^2 + c_3 T^3 + c_4 \cdot T^4 \tag{4.49}$$

with coefficients:

- $d_0 = 3.51068999 \cdot 10^{-06}$
- $d_1 = 3.27641137 \cdot 10^{-09}$
- $d_2 = 7.63396116 \cdot 10^{-11}$
- $d_3 = -6.52022078 \cdot 10^{-14}$
- $d_4 = 1.96761568 \cdot 10^{-17}$

The IAPWS and the present models are plotted in Figs. 4.2a and 4.2b, where it becomes clear that the latter is simply an extension of the former at low temperatures.

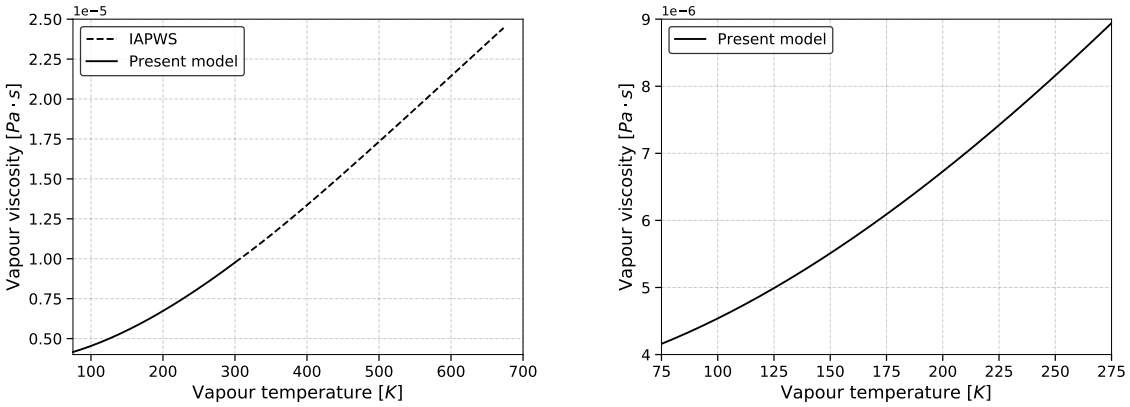

(a) Extended temperature range

(b) $\mathrm{T} \leq 300\,\mathrm{K}$

FIGURE 4.2: Vapour viscosity model for temperatures below the triple point. The IAPWS formulation (Eqn. 4.28) is included for $\mathrm{T} \geq 300\,\mathrm{K}$, for comparison.

Vapour thermal conductivity A similar discussion as above applies and only the final equation is given here for the sake of brevity:

$$k = d_0 + d_1 T + d_2 T^2 + d_3 T^3 + d_4 \cdot T^4 \tag{4.50}$$

with coefficients:

- $c_0 = 7.24966752 \cdot 10^{-3}$
- $c_1 = -1.58112357 \cdot 10^{-6}$
- $c_2 = 1.54438048 \cdot 10^{-7}$
- $c_3 = -8.44198169 \cdot 10^{-11}$
- $c_4 = 2.01111364 \cdot 10^{-14}$

4.8.3 Saturation properties

Saturation pressure curve

It is important to equip the model with a saturation pressure curve as accurate as possible, because it drives the determination of the supersaturation ratio and hence largely impacts the entirety of the condensation model. The author has examined various expressions in literature and one of the most comprehensively substantiated ones resulted from the work of Murphy and Koop (2005). They used the limited available experimental data, as well as an array of thermodynamic considerations based on the then state-of-the-art on the properties of supercooled water and produced the following relation:

$$\begin{aligned} p_{s,FP}(T) = exp\Big\{ & 54.842763 - \frac{6763.22}{T} - 4.210 \cdot ln(T) + 0.000367 \cdot T \\ & + tanh\left[0.0415 \cdot (T - 218.8)\right] \\ & \cdot \left(53.878 - \frac{1331.22}{T} - 9.44523 \cdot ln(T) + 0.014025 \cdot T\right)\Big\} \end{aligned} \tag{4.51}$$

The relation is assumed to be valid down to at least 125 K, making it suitable for our purposes. The authors also made sure it is consistent with the IAPWS saturation curve at the vicinity of the triple point (Eqn. 4.37 in Sec. 4.5.1).

Saturation temperature

The function for the saturation temperature at the local pressure is essentially the inverse of the saturation pressure function. Eqn 4.51 cannot readily be inverted and no other such relation is provided in literature. The problem is bypassed here by fitting a 4th-order logarithm-based polynomial to a tabulation of the results of Eqn 4.51, to yield:

$$\begin{aligned} T_{s,FP}(p) = & \, 1.11164211 \cdot 10^{-3} + 9.56173207 \cdot 10^{-3} \cdot ln(p) \\ & + 0.315572925 \cdot [ln(p)]^2 + 7.37978228 \cdot [ln(p)]^3 \\ & + 2.08416930 \cdot 10^2 \cdot [ln(p)]^4 \end{aligned} \tag{4.52}$$

It has been checked that Eqn. 4.52 is consistent with Eqn. 4.51 to within less 0.1 % across the full thermodynamic range, a negligible offset.

Saturation density

This follows simply via the ideal gas law that has been assumed to apply in this temperature range: $\rho_s = p_s / R / T_s$

4.8.4 Liquid properties

A recent overview of the state of the art on the estimation of various metastable liquid water properties in sub-freezing temperatures was compiled by Holten et al. (2012). The properties of supercooled water have usually been studied only at atmospheric pressure and most are generally only known with some certainty down to roughly 236-240 K. Water below those temperatures is extremely difficult to probe experimentally, primarily due to its tendency to readily crystallise unless extremely short timescales or small volumes are involved (Amann-Winkel et al., 2016); so much so, that authors often refer to the region as "no man's land" (Handle et al., 2017). As a result, data in that temperature range is practically non-existent and approximations are usually made. The analysis is further complicated by the existence of evidence that suggests water exhibits rather peculiar behaviour in such conditions, being in an intermediate state between liquid form and amorphous ice (Handle et al., 2017). The following paragraphs present a selection of expressions for the properties of supercooled liquid water that are approximate and cannot be verified or validated, but have at least been used by the cited authors in calculations that were in fair agreement with experiment. It is on these grounds that they have been adopted. Given that inside the micronozzle any liquid droplets will form at very low pressures, it is assumed that all liquid properties are dependent only on the temperature, a simplifiacation that is anyway common in condensation studies (Young, 1988).

4.8.4 Liquid density

Most available data on the liquid density do not extend below roughly 253 K (Holten et al., 2012). An exception is the work of Mishima (2010) who produced values until 200 K, but their data were derived at much higher pressures than are of interest here ($\geq$ 40 MPa). The expression employed here is the approximate fit derived by Wölk and Strey (2001) as given by Manka et al. (2012)[3] (expressed in $\mathrm{kg \cdot m^{-3}}$):

$$\rho_{l,sc} = \left\{ 0.08 \cdot tanh\left(\frac{T-225}{46.2}\right) + 0.7415 \cdot \left(\frac{T_c - T}{T_c}\right)^{0.33} + 0.32 \right\} \cdot 1000 \tag{4.53}$$

The expression was originially derived down to 220 K and configured to approximately much the density of amorphous ice at that region. Since it exhibits monotonic behaviour, here it has been extrapolated to silghtly lower temperatures (in the vicinity of 200 K). In any case, the density of water does not appear to exhibit dramatic variations in its value and is generally between 930-1000 $\mathrm{kg/m^3}$ in this temperature range.

4.8.5 Latent heat

During condensation calculations, it is important to compute the heat realeased as the vapour transitions phase. The latent is defined as the difference between the bulk enthalpies of the initial vapour and the resulting liquid. In Sec. 4.6.2, it was shown that for $T \geq 273.16$ K there are explicit expressions for each. In this case, however, it turns out that the available data make it easier to use the saturation curve and the Clausius-Clapeyron relation to instead deduce an expression for the latent heat L directly. Such an approximate expression was produced, based on various thermodynamic considerations, by Murphy and Koop (2005), formulated such that it is consistent with the IAPWS framework at the triple point (expressed in $\mathrm{J\ mol^{-1}}$):

[3]Note the expression in Manka et al. (2012) most likely contains a typographical error and the last divisor by 1000 should actually be a multiplier, as given in this work.

$$L(T) = \Bigg\{ \frac{6763.22}{T^2} - \frac{4.21}{T} + 0.000367 + \frac{0.0415 \cdot \left[53.878 - \frac{1331.22}{T} + 0.014025 \cdot T - 9.44523 \cdot ln(T)\right]}{(cosh(0.0415(T - 218.8)))^2} + \left(0.014025 + \frac{1331.22}{T^2} - \frac{9.44523}{T}\right) \cdot tanh\left[0.0415 \cdot (T - 218.8)\right] \Bigg\} \cdot R \cdot T^2 \tag{4.54}$$

It is presumed to be valid down to approximately 167K. Then, the liquid enthalpy can be deduced via Eqns. 4.54 and 4.45. The latent heat for $180\,\mathrm{K} < T < 300\,\mathrm{K}$ is plotted in Fig. 4.3, where it can be seen that the heat released follows an increasing trend with the degree of supercooling. A given mass of condensing water will release an amount of heat more than 10 % higher than at room temperature.

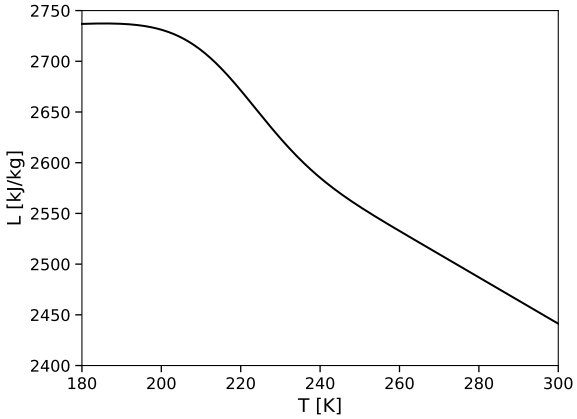

FIGURE 4.3: Variation of latent heat of supercooled water with temperature, according to the work of Murphy and Koop (2005).

4.8.6 Surface tension:

It is shown later in Sec. 5.3 that the value of the surface tension has a dominant contribution in condensation studies, therefore it is desirable that its determination is as reliable as possible. Very little experimental data is available on the surface tension of supercooled water and even that is limited to no further than roughly 243 K. Overviews of such datasets are given in the works of Holten et al. (2012) and Hrubý et al. (2014). It is suggested in Petrova (2014) that the IAPWS formulation given by Eqn. 4.40 is "reasonably accurate" down to 250 K. Other empirical relations have been formulated in various works in literature and a critical review of a few of the most common ones is given by Lamanna (2000). In that work, Lamanna argues that most of these relations are physically unsubstantiated and empirically derives her own, based on thermodynamic considerations and experimental data from her own work (denoted here as σ_{LD} from the original work):

$$\sigma_{LD} = \begin{cases} 0.0852 - 3.54236 \cdot 10^{-4} T + 3.50835 \cdot 10^{-6} T^2 \\ -8.71691 \cdot 10^{-9} T^3 \quad \text{[N/m] for T<250 K} \\ \\ (76.1 + 0.155 \cdot (273.15 - T)) \cdot 10^{-3} \quad \text{[N/m]} \\ \text{for T} \geq 250 \text{ K} \end{cases} \tag{4.55}$$

The other relation frequently cited in literature is that of Viisanen et al. (1993):

$$\sigma_{FP}(T) = 93.6635 \cdot 10^{-3} + 9.133 \cdot 10^{-6} \cdot T - 2.75 \cdot 10^{-7} \cdot T^2 \tag{4.56}$$

The rationale behind and accuracy of this latter equation is unclear. The only seemingly applicable source the author has been able to trace in literature is the dissertation of Dillman (1989) (as reported in Viisanen et al. (1993)), who appears to have used it in deeply supercooled states (apparently down to <200 K). In a later publication, Dillmann and Meier (1991) briefly state the empirical formula has in turn been adopted from Landolt and Börnstein (1960). The present author has not had access to either of these works, so the details of its derivation and validity cannot be verified. Lamanna did acknowledge that this relation is also thermodynamically consistent as is her own, but went on to dismiss it as inaccurate relative to experimental data. This is an interesting assessment, given that the experimental data in literature tends to be somewhat inconsistent in itself.

To obtain an independent assessment on this, Eqn. 4.55, Eqn. 4.56 (Strey et al., 1994) and the IAPWS formulation (Eqn. 4.40) have all been plotted in Fig. 4.4 against the experimental data of Hacker (1951), Floriano and Angell (1990) and Hrubý et al. (2014). The former two datasets have been chosen because they are some of the most frequently cited ones and exhibit the highest degree of supercooling. The latter dataset is added because it is the most recent one and has been produced by consistent measurements of two independent laboratory setups in different locations, therefore likely constitutes the current state of the art.

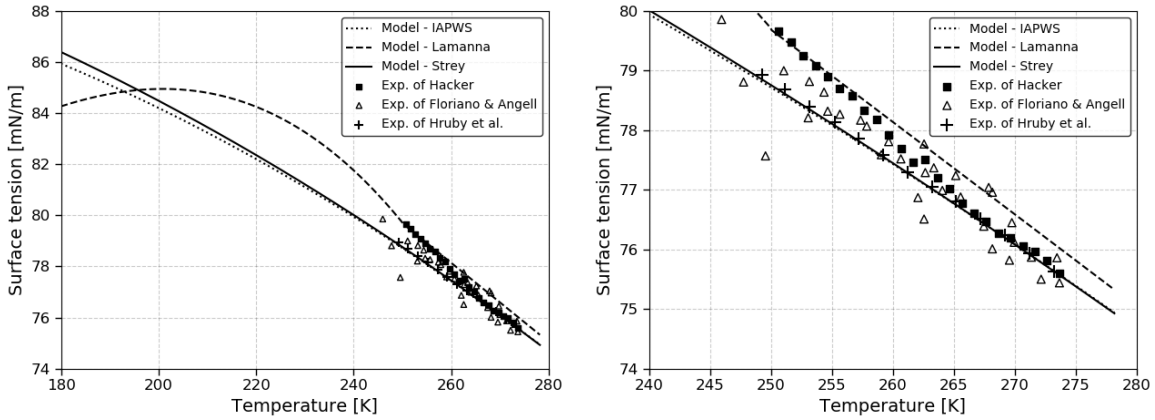

(a) Extended temperature range

(b) Temperature range in the vicinity of the triple point

FIGURE 4.4: Comparison of common models for the surface tension of supercooled liquid water with selected experimental datasets

In that figure it is shown that the expression of Lamana is in fact itself only in moderate agreement with the experiments of Hacker (1951) and Floriano and Angell (1990), experiences an inflection at the switching temperature of 250 K - this inflection was hypothesised in the past but is disputed by more modern data ((Hrubý et al., 2014)) - and a maximum at roughly 200K that could be more of a numerical artefact than a physical result. On the other hand, Eqn. 4.56 is in fair agreement with all data, in excellent agreement with the most recent data of Hruby et al. and in near-perfect agreement with the IAPWS formulation at the high temperature end. What is more, Viisanen et al. (1993) and Manka et al. (2012) have later both used Eqn. 4.56 to deduce nucleation rates in fairly close agreement with experiments at temperatures down to <200 K[4]. In the context of the discussion made in Sec. 5.3, explaining the high sensitivity of the CNT-predicted nucleation rate on the surface tension (which is also used in the aforementioned works as an intermediate step for the characterisation of the nucleation of ice), it may be assumed that such agreement with experiments would not have been possible if the

[4]The former authors did note discrepancies at the lowest temperatures, but showed these were likely not due to the accuracy of the thermophysical properties, but rather due to inherent shortcomings in the nucleation theory they employed

surface tension value had been largely inaccurate. Hence it is assumed here that it is suitable for our purposes and Eqn. 4.56 has been used for the two-phase model in this work, when $T < 273.15\,\mathrm{K}$.

4.9 Numerical implementation

The current structure of the thermodynamic framework in OpenFOAM is based on the gas pressure and temperature for the determination of thermodynamic properties. Indeed, the majority of expressions presented in this chapter can be implemented in the software via the creation of dedicated classes whose functions will simply receive the pressure p and/or temperature T of the gas/liquid and return the desired variable value. However, this creates an issue in those instances in which the density needs to be extracted from the value of pressure and temperature, because the equation of state (Eqn. 4.1) is a quartic polynomial function of the density that cannot simply be inverted.

In the early stages of this work, this was addressed by implementing the semi-analytical rapid quartic solver of Strobach (2010), which is shown by that author to provide gains in execution speed over more conventional quartic solvers. This was effective, but impractically slow for numerical purposes, as the solution of the polynomial over every cell of the computational domain still took too long to be useful. An alternative was found in implementing a table look-up method: the EoS is used to tabulate values of density for a range of pressure-temperature (p-T) combinations; then, an algorithm is written that when fed with a combination of p-T, looks for that specific location in the table to find the corresponding density value. Since the inputs will typically not correspond exactly to the discrete values saved in the table, the desired density value is computed by a simple linear interpolation from the nearest neighbouring table entries. This was also effective and offered a stark performance improvement relative to the quartic solver method (at least an order of magnitude faster over a given simulation case). However, since the computational means the author has had at his disposal have been somewhat limited, it was desirable to accelerate the solver further.

Luckily, a simplification is afforded in this particular case due to the fact that the flow in the micronozzle expander will generally feature low pressures of $\leq 0.5\,\mathrm{bar}$. In the polynomial of Vukalovich, the third and fourth Virial coefficients typically only have a significant contribution at high pressures (recall the EoS is valid up to 100 bar). It was found that for the low pressures of interest here they can be omitted, with virtually no loss in accuracy (less than 0.1 % between the original and the simplified version). So, for the simulations presented in this work, the expressions listed under Secs. 4.2 and 4.3 have been truncated after the second coefficient (B1), which makes the solution much faster. Should another user need this solver in the future, the full Virial EoS with the tabulation method remains implemented, such that any given range of pressure/temperature combinations covered by the full EoS can be simulated.

4.10 Freezing of droplets

The preceding discussions treated thermodynamic regions well below the triple point temperature, yet no mention of the liquid water freezing to ice or even the water vapour directly depositing to it was made. The reason is that, in this work, the prospect of the droplets freezing in the nozzle expander is ignored.

There is a sizeable volume of literature concerning the process of vapour nucleation in sub-freezing temperatures. One overview of at least the experimental work has been compiled by Wyslouzil and Wölk (2016). Among these works, there are three key observations that help substantiate the above assumption:

- One observation relevant to the present study is that, even in temperatures as low as near 200 K, if condensation occurs, the vapour will likely first collapse to liquid and only then transition to ice. The existence of such a step-wise mechanism was first stipulated by Ostwald (1897) and has been confirmed in more recent experiments (Manka et al., 2012; Wyslouzil and Wölk, 2016). This delays the occurence of freezing and implies the liquid droplet may have exited the nozzle by the time freezing begins. Indeed, the following point solidifies this hypothesis.
- Fransen et al. (2014) conducted calculations to estimate the mean life of liquid droplets at deep levels of supercooling; that is, how long it takes after the vapour has condensed to liquid for freezing to occur. They showed that freezing is insignificant down to 240 K and even at 220 K the mean life of the droplet would exceed 2 ms, far longer than what the flow here spends in the micronozzle. The discussion by the authors does imply that at low pressures, such as those of interest here, the lifetime may be shorter than estimated. But even in that case, it is unlikely the effect is of significance, as noted by the following point.
- The third relevant observation, is that the latent heat released as the supercooled water transitions to ice is insignificant compared to that released when the vapour first collapses to liquid. This becomes evident in Fig. 4 of the work of Manka et al. (2012), who recorded the pressure and temperature along the nozzle centerline as first condensation and then freezing occured at temperatures in the vicinity of 200 K. The locations of the onset of freezing are well downstream of that of the condensation. While the effects of the heat released upon condensation are clearly evident, the effect of freezing is too small to be distinguishable. The authors note that in the vicinity of 200 K, the heat of fusion is only about 5% that of condensation and so the resulting temperature rise does not exceed 1 K or so.

Based on these points, it can be safely assumed that 1) freezing is not very likely to occur in the short timeframes of micronozzle flow and 2) even if it does, its macroscopic effects are likely to be negligible. On these grounds it is neglected.

4.11 Summary of the thermodynamic model

For the simulation of water vapour condensing to liquid in rapid micronozzle expansions, it is necessary to be able to compute the properties of H2O in gaseous and liquid form, in equilibrium and in metastable states, as well as on the saturation line. To that end, a set of empirical relations has been amassed following an extensive review of literature, based on what is currently considered the state of the art in the scientific community. The model has been presented in two main portions, for $T \geq 273.16$ and $T \leq 273.16$. That is to denote that in the former case the properties are generally well known, while in the latter largely hypothesized.

Validation of these expressions would be desirable. For the thermodynamic regions for $T \geq 273.16$ this is not really necessary. It has been checked that the implemented expressions reproduce benchmark data in literature to the last significant digit and from there on, it is well established these expressions are representative of reality. This is implicitly confirmed in the successful validation cases of the entire condensation model in Sec. 5.9.

Less certainty is afforded for $T \leq 273.16$ K. It is reasonable to accept that the gaseous properties in that region, as derived here, are sufficiently accurate, given that the validation case of Sec. 3.5.2 implemented this model and was in good agreement with experiment. For the saturation and liquid properties, however, the lack of data leaves little option but to simply assume they are suitable for this work, especially for temperatures below roughly $T \leq$ 235-240 K. This is the threshold below which there is practically no experimental data. In the rough range 235-273.16 K most expressions have indeed been based on - at least some, albeit limited - available experimental data, such that it may be

assumed they are representative of reality. It is shown in Ch. 7 that most of the micronozzle cases examined in this work indeed operate roughly within this temperature range. However, the case featuring the lowest stagnation pressure or highest rate of expansion (nozzle with the highest expander angle) will feature temperatures in the divergent in the vicinity of 200 K. In that region the majority of expressions for the liquid properties are at least largely approximate. Their validity is assumed on the grounds that the original scientific works from which they are adopted, successfully implemented them in reproducing various condensation-related experiments in different contexts, with reasonable agreement. Hopefully, in the near future, progresses in the experimental sciences of H2O thermodynamics will help bridge this gap.

The analysis now proceeds to the presentation of the condensation model itself, in the following chapter.

Part III

Two-phase model

CHAPTER 5

Two-phase model

This chapter outlines the model for the computation of condensation in the flowfield. Including the emergence and evolution of the liquid phase requires modelling of three basic processes:

1. The spontaneous emergence of the first liquid nuclei out of the vapour
2. The subsequent growth of the droplets following their formation, by the coalescence of more vapour molecules
3. The interaction of the above two processes with the gaseous phase in terms of mass, momentum and energy

Dedicated approaches apply to each and the principles and limitations of these are outlined in this chapter. The chapter starts with a presentation of the basic modelling principles and some of the fundamental assumptions involved. The actual nucleation and droplet growth models then follow, with more assumptions scrutinised as the description goes along. The numerical implementation of the model in the OpenFOAM platform is also explained in detail and the chapter eventually concludes with the validation of the model against benchmark experiments.

5.1 Basic principles

The subject of non-equilibrium steam condensation in supersonic flows has received widespread study over the last 70 years at least and it is not the purpose of this document to review it in detail or address its historical develoment. Only a brief presentation of the main principles is given in this chapter. Comprehensive reviews can be found in works such as those of Wegener and Mack (1958), Feder et al. (1966), Hill (1966), Gyarmathy (1976), Lai and Kandambi (1993), Lamanna (2000), Bakhtar et al. (2005) and the references therein. The majority of the background information given in this chapter is extracted from these sources. It suffices to say here that, despite the decades of effort, the underlying physics still partly eludes scientific understanding and the related modelling efforts are largely approximate.

When it comes to continuum flows, the modelling of condensation is typically done in either of two ways:

- A Eulerian - Lagrangian approach. The gas is modelled from a stationary observer's perspective in the framework of a finite volume (and/or finite element) discretisation, typically via the numerical solution of the Navier-Stokes equations, as is the set-up of most modern compressible CFD tools. The liquid droplets, on the other hand, are modelled in the framework of an observer moving with the flow. Their motion in the gas is described by the integration of their precise trajectories, based on the Newtonian laws of motion.
- A Eulerian-Eulerian approach, in which both the gaseous and the liquid phase are described by means of a set of balance laws describing the conservation of governing variables. The trajectories of the droplets are not tracked in this case and their interaction with the gas is expressed in terms of a set of volumetrically averaged parameters.

While the former approach is more precise in its description of the flow dynamics and generally more accurate, the necessity to track the motion of the droplets comes at a distinctly higher computational cost, increasingly so as the complexity of the flowcase increases (Young, 1992; Gerber, 2002; Gerber and Kermani, 2004). The volumetric averaging inherent to the Euler-Euler approach sacrifices some accuracy in exchange for computational simplicity, especially at the region of the first onset of condensation, where gradients are very sharp and the vapour-droplet interaction particularly complex. Even so, the latter approach has historically proven to be sufficiently performant for most applications and since the computational means the present author has had in his disposal are limited, it is the method implemented in this work.

The Eulerian-Eulerian approach itself, also has two variants that typically dominate in literature, pertaining to how the population of droplets is quantified and how the thermodynamic interaction with the flow is described. The thermodynamic interaction is generally implemented by:

- A mixture based approach, in which the gaseous (g) and liquid (l) phases are directly coupled as a mixture in the definitions of the various thermodynamic properties of the flow, via substituting an expression of the form

$$\frac{1}{\rho} = \frac{1-Y}{\rho_g} + \frac{Y}{\rho_l}$$

  where Y is the fraction of the liquid to the vapour mass. Then, in the conservation equations, source terms are introduced only for the liquid phase equations to describe the birth and growth of droplets, while the vapour and its interaction with the liquid is described via the original Navier-Stokes laws and the above mixture definition, without any source terms.

- A source term based approach, in which the thermodynamics of the vapour and liquid are described separately and the coupling between the phases takes place directly at the conservation equations, by the introduction of a set of source terms in each and every of the balance laws.

In turn, for the quantification of the droplet population:

- A monodisperse droplet approach, in which it is assumed that the droplet population consists of sizes sufficiently uniform, such that it can be represented by a single group of spherical droplets of mean radius $\bar{r}$ and a liquid mass fraction $Y = N\rho_l \frac{4}{3}\pi\bar{r}^3$. (Mccallum and Hunt, 1999; Gerber and Kermani, 2004)

- A moment-based approach, in which the droplets are modeled as a set of populations of different sizes, whose properties are described by a set of successively solved ”moment” equations (Hughes et al., 2015).

The mixture- and moment-based method is supposed to be more accurate, since it largely avoids the crude averaging of properties of the source-term based, monodisperse approach. In some instances, this is in fact the case, but in other instances it is not (Starzmann et al., 2018), primarily due to the fact that the large uncertainties generally involved in any condensation study may overshadow any increments in performance resulting from the former method. Due to the particular architecture of OpenFOAM, it was generally found by the author to be much simpler to implement the source-term based, monodisperse method. This is especially due to the fact that the use of source terms avoids heavy modifications in the thermodynamic description of the gas, which can be quite tedious in the software. And as perhaps became apparent in Ch. 4, the simpler thermodynamic implementation that treats the gas and liquid separately has already been rather tedious in itself. Moreover, a moment-based approach typically introduces an additional 4 conservation laws, which comes at a computational expense. Since it has further been shown that the monodisperse, source-term based description offers

sufficiently high performance in most applications involving low pressures (Gerber, 2008), it is the method of choice here.

Accordingly, the implementation is done by augmenting the Navier-Stokes equations presented in Ch. 3 by an additional two balance laws, describing the conservation of the number of droplets in the flow N (expressed per unit vapour mass) and the conservation of the liquid-to-vapour mass fraction Y (dimensionless):

$$\frac{\partial \rho}{\partial t} + \nabla \cdot (\rho \mathbf{v}) = -S_Y \tag{5.1}$$

$$\frac{\partial}{\partial t}(\rho \mathbf{v}) + \nabla \cdot (\rho \mathbf{v}\mathbf{v}) = -\nabla p + \nabla \cdot \tau + S_V \tag{5.2}$$

$$\frac{\partial}{\partial t}(\rho E) + \nabla \cdot (\mathbf{v}(\rho E + p)) = \nabla(k \nabla T + (\tau \cdot \mathbf{v})) + S_h \tag{5.3}$$

$$\frac{\partial (\rho Y)}{\partial t} + \nabla \cdot (\rho Y \mathbf{v}) = S_Y \tag{5.4}$$

$$\frac{\partial (\rho N)}{\partial t} + \nabla \cdot (\rho N \mathbf{v}) = S_N \tag{5.5}$$

The source terms S_x describe the exchange of mass, momentum and energy between the two phases and are addressed in Sec. 5.6. From there on, the modelling of condensation concerns the suitable description of the processes of nucleation and droplet growth, such that expressions for the source terms given above can be derived. This is the subject of the remainder of this chapter, starting from an overview of the most basic assumptions in the following section. In a general sense, the condensation model as described in this chapter is largely an adaptation of the work of Gerber and Kermani (2004), with modifications whenever applicable to our purposes.

5.2 Assumptions

Only the basic assumptions made are listed below. More assumptions will be introduced as the model is outlined (some of which require a more elaborate discussion than others) and they are directly addressed in the respective sections.

1. In supersonic nozzle expansions, the timescale needed for foreign nuclei to serve as condensation surfaces far exceeds that of the expansion process itself and their contribution may be ignored (Hill, 1966; Bakhtar et al., 2005). The contribution of the nozzle walls is also neglected henceforth on the same grounds, as well as on the grounds of the fact that the nozzles of interest in this work are generally assumed to be elevated to temperatures $>400\,\mathrm{K}$, where condensation is not likely. Therefore, only homogeneous nucleation is considered in this work.
2. The volume of the medium surrounding a given droplet is assumed infinite. The volume of the droplets is small relative to that of the gaseous phase ($\leq 5\%$), such that no volume fraction equations need to be solved to treat the phases separately.
3. Droplets are assumed perfectly spherical and infinitely stiff. At the earliest stages of nucleation, when the newly formed clusters are only a few water molecules wide, the droplet is likely not quite of spherical shape. But for most practical purposes, this is a good approximation, as was also confirmed in the nucleation studies of Kim et al. (2004).
4. As is typically the case in nozzle flows, owing to the high speeds and short dimensions, the effect of gravitational forces on the flow and the droplets are negligible.

5. It is assumed the droplets are small enough for the velocity slip between them and the gas to be negligible. Effectively, this means the droplets present no drag to the flow and travel at the gas velocity. The validity of this assumption is scrutinised in Sec. 5.5.

6. It is assumed that no droplet agglomeration takes place (i.e. different droplets do not coalesce on each other) and the interactions between the droplets themselves are ignored. This is a good approximation, as long as the mass fraction of the liquid phase remains low ($Y < 0.1$) (Gerber and Kermani, 2004).

5.3 Droplet nucleation model

Most nucleation studies are based on a theoretical framework referred to as the Classical Nucleation Theory (CNT), developed in its original form by researchers such as Volmer (1939) and Frenkel (1955) and having seen various modifications since. As it is relevant to our later discussion, an overview of the basic principles is briefly given here, but the reader is referred to the work of Bakhtar et al. (2005) and the references therein for a comprehensive overview. Insightful discussions into the underlying physics have been given by McDonald (1962, 1963).

The basic idea is to express the nucleation process in terms of a "nucleation rate", i.e., a parameter describing the rate of generation of liquid clusters per unit mass (or volume) of vapour, per unit time. It can then be used as input to the droplet growth model (described in Sec. 5.4), for a complete description of the condensation process. The CNT derives the nucleation rate based on considerations from statistical thermodynamics and a number of simplifications on the local flow topology.

One starts by considering the specific Gibbs free energy of the system, introduced earlier in Sec. 4.3.1 and given by:

$$G = U - TS + pV$$

Initially, for a droplet-free vapour of total mass M_t, the total Gibbs free energy is $G_1 = G_G M_t$. After a spherical droplet of radius r, area $A_L = 4\pi r^2$ and mass $M_L = \rho_l \frac{4}{3}\pi r^3$ has condensed, the mass is divided into a vapour and a liquid constituent: $M_t = M_G + M_L$. So, for the initial state, one may write:

$$G_1 = G_G(M_G + M_L)$$

When the droplet forms, the vapour experiences a change ΔG in its Gibbs free energy and the balance can simply be written as (denoting the final state by the subscript "2"):

$$G_2 = G_1 + \Delta G = G_G(M_G + M_L) + \Delta G$$

This change ΔG essentially expresses the Gibbs free energy of the droplet and is associated with two contributions:

- a change in the system's chemical potential due to the emergence of the new phase
- an amount of work expended in forming the surface area of the droplet.

The change in chemical potential can be expressed as the difference in free enthalpies $G_G - G_L$ between the vapour and the droplet in the final state. By using fundamental thermodynamic relations and assuming 1) an ideal gas such that its specific volume is $\frac{RT}{p}$, 2) that the specific volume of the droplet is negligible and 3) only small perturbations from equilibrium so that conditions are essentially isothermal, it is easy to show that the difference in G between the vapor and the droplet is:

$$G_G - G_L = RTln\left(\frac{p_G}{p_s}\right)$$

where the term in the logarithm is the ratio of saturation. The second contribution has to do with the energy extracted by the condensed droplet in the form of the surface energy required to keep its liquid form bonded. In CNT theory it is defined by σA_L, where σ is the liquid surface tension per unit area. Eventually, a simple mathematical manipulation of the above relations shows that the change in the total Gibbs free energy of the system (not per unit mass) following the condensation of a droplet is given by:

$$\Delta G = G_2 - G_1 = G_G M_G + G_L M_L + \sigma A_L - G_G(M_G + M_L) = \sigma A_L + (G_L - G_G)M_L \Rightarrow$$

$$\Delta G = 4\pi r^2 \sigma - \frac{4}{3}\pi r^3 \rho_l R T_g ln\left(\frac{p_g}{p_s}\right) = \Delta G_s + \Delta G_v \tag{5.6}$$

The terms ΔG_s and ΔG_v respectively denote the surface energy contribution to the free energy of the droplet and a bulk contribution proportional to its volume. It is a core assumption of the classical nucleation theory that the free energy of the droplet down to its smallest possible size can be expressed as a sum of these two contributions, also implicitly assuming in the process that the droplet has a spherical shape at that size (as explained in Sec. 5.2). The surface term is always positive while the volume term always negative and, in the small radius limit, the surface term prevails. It is instructive to use this expression to produce a generic plot of ΔG as a function of the droplet radius, shown in Fig. 5.1.

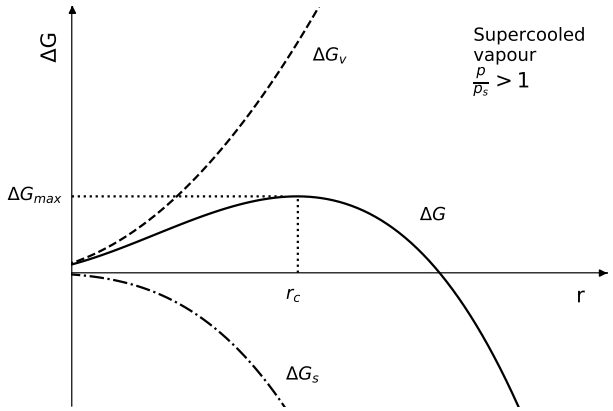

FIGURE 5.1: Variation of ΔG with droplet radius for supersaturated vapour ($S > 1$). The surface and volume constituents are denoted by ΔG_s and ΔG_v, respectively.

It can be seen that there is a value of the radius r for which ΔG obtains a maximum. For a radius beyond this value, the droplet will decrease the Gibbs free energy of the system by capturing more vapor molecules, whereas for a smaller value, it will increase it by loosing molecules back into the vapour. What this means physically, is that there is a critical radius value r_c at which the droplet is in unstable equilibrium with its surroundings and that if a freshly nucleated liquid cluster exceeds this value it will be stable enough to grow, otherwise it will disintegrate back to vapour. On these grounds, the critical radius is a major driver in the determination of the nucleation rate and it is straightforward to derive that ΔG attains a maximum of:

$$\Delta G^* = \frac{16\pi\sigma^3}{3\left[\rho_l R T_g ln\left(\frac{P_g}{P_s}\right)\right]^2} \tag{5.7}$$

at a critical radius ($S = \frac{P_g}{P_s}$):

$$r_c = \frac{2\sigma}{3\rho_L(\Delta G^*)} = \frac{2\sigma}{\rho_L R T_g ln(S)} \tag{5.8}$$

The derivation of the expression of the nucleation rate itself is somewhat extensive and will not be given here, but can be found in Bakhtar et al. (2005). The essential principle is to consider that during the nucleation process, clusters continually form and disintegrate at approximately an equal rate, such that the concentration of clusters of a given size (say, a cluster of g water molecules, termed a g-mer) is approximately constant. When a favourable free energy gradient ΔG_g is present, however, new nuclei will form at radii exceeding the critical radius and, instead of disintegrating, will start to grow. The concentration of g-mers, here denoted by f_g, is no longer constant and varies in time proportionally to the rate at which a population of g-mers per unit volume per unit time grows to (g+1)-mers. One can then use some basic principles of statistical thermodynamics to express this process with a balance equation of the form:

$$\frac{\partial f_g}{\partial t} = -\frac{\partial J}{\partial g} \tag{5.9}$$

From there on, the basic idea is to assume that once the nucleation rate J has reached steady-state, the concentration n of clusters of critical size $r = r_c$ follows a Boltzmann (equilibrium) distribution:

$$n = n_1 e^{-\Delta G_g / k_B T_g} \tag{5.10}$$

where n_1 is the number of molecules per unit volume. Following some further manipulation and using the expression for ΔG given by Eqn. 5.6, a steady-state solution to Eqn. 5.9 for the CNT-predicted nucleation rate is derived in its final form as:

$$J = q_c \frac{\rho_g^2}{\rho_l} \sqrt{\frac{2\sigma}{\pi m^3}} exp\left(-\frac{4\pi\sigma}{3k_B T_g} r_c^2\right) \tag{5.11}$$

where q_c is a condensation coefficient touched upon in Sec. 5.4.1 and $m = 2.988 \times 10^{-26}$ kg is the molecular mass of water. The rest of the parameters have been previously introduced. This expression is the cornerstone of the nucleation model adopted here and serves to quantify the first emergence of liquid droplets out of the vapour, before they go on to grow. However, the assumptions under which it is derived need some scrutiny for the purposes of this work, as discussed in the following subsections.

One last comment is due, here. In Sec. 4.8.6, it was stated that the surface tension is a driving parameter in the condensation model and it now becomes clear why. Inspecting Eqn. 5.11 shows that σ enters the exponent to the power of 3, via the critical radius. The nucleation rate then becomes very sensitive to this parameter. It is instructive to make a back-of-the-envelope calculation using Eqn. 5.11. Assume typical values for the parameters: $q_c = 1$, vapour and liquid densities of $\rho_g = 0.05\,\mathrm{kg/m^3}$ and $\rho_l = 1000\,\mathrm{kg/m^3}$, temperature $T_g = 280\,\mathrm{K}$, surface tension $\sigma = 0.07\,\mathrm{N/m^2}$ and a saturation ratio $p/p_s = 10$. The critical radius follows from Eqn. 5.8 as $r_c = 4.7 \times 10^{-10}\,\mathrm{m}$. These values give a nucleation rate $J = 1.03 \times 10^{26}\,\mathrm{droplets/m^3}$. Now, increase the surface tension value by 1 % to 0.0707 N m and repeat the computation, all other parameters fixed: $J = 6.25 \times 10^{25}\,\mathrm{droplets/m^3/s}$. A 1 % increase in the surface tension induced an almost 40% decrease in the nucleation rate. In different conditions, the effect may be as much as 100 % (Young, 1992). This is why it is important that this parameter is accurately modelled and the reason that motivated the detailed discussion of Sec. 4.8.6.

The surface tension value as evaluated in Ch. 4 is a bulk property and generally determined by means of a liquid film measurement. This degree of sensitivity of J on it continues to this date to fuel a debate on whether it is applicable to use the bulk surface tension value on droplets that span only a few nanometres and have little reminiscence of a liquid film. In fact, when their condensation model is

implemented and turns out to be in disagreement with validation data, many authors in literature use the value of σ as a tuning parameter to correct the model (see, for instance, the works of Young (1992) and Gerber (2002); Gerber and Kermani (2004)). But such corrections can only be made in hindsight and hence are of little use to exploratory numerical studies. In this work, the bulk value of σ as given by Eqns. 4.40 and 4.56 is used without any modifications and it is shown in the validation of Sec. 5.9 that this creates no substantial disparity with experiments for the present model.

5.3.1 On the validity of the steady-state nucleation assumption

Eqn. 5.11, in the form given here or in a number of variations, serves as the backbone of many, if not most, modern nucleation analyses. However, its validity for the particular flow cases of interest here warrants some discussion, because it entails the steady-state assumption. This means it is assumed that the time interval between the moment conditions in the flow become suitable for nucleation to begin and the moment the generation rate of critical clusters has reached equilibrium is negligible. In conventional nozzles, this assumption is supported by the fact that the transient stage of the nucleation process typically lasts about a microsecond, while the process itself as a whole stays active for 10-50 µs (Bakhtar et al., 2005). In contrast, the characteristic flow timescales in micronozzles are in the order of a couple of microseconds at most. For geometries comparable to those of interest here, experiments by Bayt (1999) and Bayt and Breuer (2000) showed that characteristic residence times of fluid particles in typical micronozzle configurations, measured from the throat to the exit, are in the range 1-2 µs. Therefore, we must examine whether Eqn. 5.11 is applicable to our case.

Our focus is then shifted to the transient portion of the nucleation process. The work of Abraham (1981) faced a similar issue when examining small (throat diameters of 0.025-0.25 mm) laval nozzles operating on sulfur hexafluoride (SF6) propellant. The authors stated a correction factor was implemented to account for nucleation transients, but provided little detail on the specifics. The matter is examined in a bit more detail here, the purpose being to make a rough estimation of how long it takes the nucleation to reach equilibrium in conditions relevant to micronozzles.

In a conventional nozzle, the nucleation region only occupies a narrow region in the expander, because it is quickly quenched by the latent heat released as the nucleated droplets grow. Here, however, it is expected that due to the small dimensions, if nucleation occurs it will stay active throughout the micronozzle expander, even as the nucleated droplets may grow. For this reason, the characteristic timescale is taken as the full time of traversion of the expander by a microdroplet.

The subject of transient nucleation, for steam or liquid water, received some attention in the 20th century, with the works of Probstein (1951), Kantrowitz (1951), Wakeshima (1954), Collins (1955) and Courtney (1962a,b) being some of the most detailed treatises. Kashchiev (1969) produced a semi-analytical transient solution to Eqn. 5.9 in the form:

$$J_{tr}(t) = J_{ss}\left[1 + 2\sum_{i=1}^{\infty}(-1)^n exp(-n^2 t/\tau)\right] \tag{5.12}$$

where the subscripts tr and ss denote the transient and steady-state (given by Eqn. 5.11) nucleation rates, respectively, t is the time elapsed from the onset of condensation and τ is the relaxation time until equilibrium is reached. Estimates for τ may be derived via suitable approximations to analyses of statistical thermodynamics on the vapour flow and numerous versions have been given by various authors, including Kashiev himself. In a later work, Kelton et al. (1983) found the simple expression by Collins (1955) to work well when short timescales are involved:

$$\tau = \frac{9\pi k_B T g_c^{\frac{2}{3}}}{\mu'^2 \sigma \beta} \tag{5.13}$$

In this expression $k = 1.38 \times 10^{-23}\,\mathrm{m^2 kgs^{-2} K^{-1}}$ is the Boltzmann constant and σ the surface tension of the liquid cluster. The parameter g_c expresses the number of water molecules contained in a liquid cluster of critical radius r_c. Assuming a perfectly spherical cluster of molecules of mass m and using Eqn. 5.8 it follows:

$$g_c = \left(\frac{4\pi\rho_L}{3m}\right)^{1/3} \frac{2\sigma m}{\rho_L k T_G ln\left(\frac{P}{P_{sat}}\right)} \tag{5.14}$$

To close the system of equations, expressions for the parameters β and μ' in Eqn. 5.13 are needed. The term β expresses the frequency of collision of single molecules per unit area and, for the particular case of a vapour nucleating onto itself, was given by Collins (1955) as:

$$\beta = n_1 \left(\frac{kT}{2\pi m}\right)^{1/2} \tag{5.15}$$

where n1 is the concentration of vapour molecules. The concentration may be calculated from the value of the vapour density, the molar mass M_{molar} and the Avogadro number $\mathcal{N}_a$ as:

$$n_1 = \frac{\rho_g}{M_{molar}} \mathcal{N}_a \tag{5.16}$$

Lastly, μ' is an auxiliary parameter following as:

$$\mu' = 4\pi \left(\frac{3m}{4\pi\rho_L}\right)^{2/3} \tag{5.17}$$

It is now possible to use Eqn. 5.12 supplemented by Eqns. 5.13-5.17 to obtain estimates of the time it takes for the nucleation rate of critical clusters to reach equilibrium given a set of vapour conditions. At first sight it might seem that there are too many variable parameters involved. But a close inspection of the equations shows that selecting a temperature value fixes all parameters except for the pressure (recall from Ch. 4 that ρ_L, σ and P_{sat} are a function of temperature only and all other parameters are either a function of these or constant). It is therefore possible to examine how quickly the nucleation rate reaches steady-state for a given supersaturation ratio at a selected temperature.

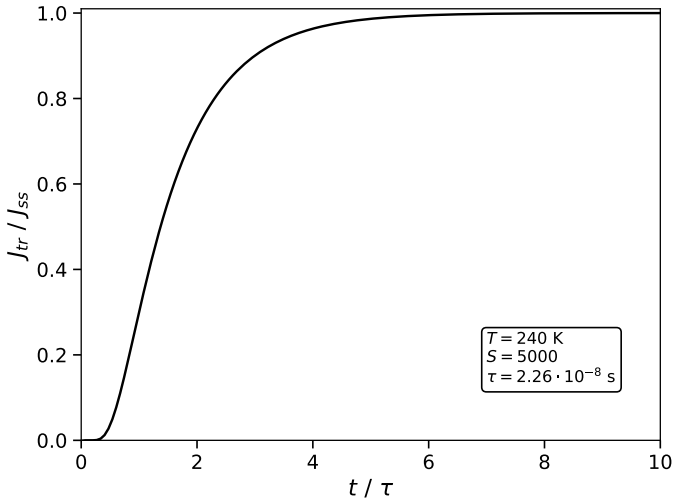

FIGURE 5.2: Example of the temporal evolution of the transient nucleation phase

An indicative plot is given in Fig. 5.2. The temperature and saturation ratio have been set at 240 K and 5000, respectively. These may seem like extreme values, but it was originally expected (and later, in Ch. 7 confirmed) that the extreme expansion rates would make such conditions typical in the micronozzle. The figure shows that the nucleation rate has reached 99 % of its steady-state value after roughly 6.5τ

or about 9×10^{-8} s. This is less than 1/10th of the time the flow is estimated to stay in the expander. It is a small fraction, but not necessarily a negligible one.

Even so, here it is chosen to neglect the transient phase. On one hand, the author could not readily see a way to implement a transient nucleation rate in a finite-volume framework, in which the radii of the computed droplets are averaged. It is simply not possible to track the history of a droplet whose properties are continually averaged over the entire droplet population in a cell, therefore implementing a transient model is not feasible. The prospect of some simple correction factor was also examined and some examples in literature exist, but they are too approximate and inconsistent to be of practical use here. On the other hand, this fraction is not very significant and, in any case, assuming a steady-state nucleation provides the worst case scenario on the magnitude of the nucleation, such that any design decisions resulting from the results of this analysis will be conservative. On these grounds, it has been decided to tolerate any loss of accuracy that may result from this assumption.

5.3.2 Corrections to the classical nucleation rate

Complete from a thermodynamic perspective as the nucleation rate derivation may appear, Eqn. 5.11 actually rarely agrees well with experiments by itself (Bakhtar et al., 2005). It seems that the precise mechanisms of nucleation are still not fully understood, but CNT also inherently suffers from a number of limitations. In the brief discussion of its derivation, it became clear it involves assumptions such as that of isothermal/isobaric conditions, that the droplet is in equilibrium with its surrounding vapour or the vague assumption on the nature of the surface tension forces. It should be understood that CNT was originally developed as a general theory and not as one applicable only to non-equilibrium flows. It turns out that some of these assumptions break down in rapid expansions.

To bypass these limitations, it is customary that empirical correction factors are introduced to Eqn. 5.11. Various corrections have been proposed for different circumstances. Overviews of some of the main ones can be found in Bakhtar et al. (2005) and Lai and Kandambi (1993). Here, two corrections are implemented, briefly discussed below.

Non-isothermal nucleation correction The assumption of isothermal conditions described above is fairly valid in those cases in which steam is transported as part of a non-condensible carrier gas (say, argon), because the collisions between the molecules of the carrier and the droplets are sufficient to transfer the energy released on condensation away from the the droplet kinetically, such that large temperature gradients are avoided at the interface. However, in pure vapour expansions, the freshly nucleated clusters are smaller than the vapour molecules' mean free path, such that the collision mechanism is not particularly effective and a significant temperature gradient is established. To amend this disparity, Kantrowitz (1951) derived a correction of the form:

$$J = \frac{J_{CNT}}{1-\eta} \tag{5.18}$$

where J_{CNT} is given by Eqn. 5.11 and η follows as (in a simplified form for low-pressure cases):

$$\eta = q_c \frac{2(\gamma-1)}{\gamma+1} \frac{h_{fg}}{RT_g} \left(\frac{h_{fg}}{RT_g} - \frac{1}{2} \right) \tag{5.19}$$

The parameter q_c is the same condensation coefficient as in Eqn. 5.11 and is revisited in Sec. 5.4.1. The term h_{fg} denotes the latent heat per unit mass of vapour released upon the droplet's condensation: $h_{fg} = h_g - h_f$. Young (1992) and Bakhtar et al. (2005) note this correction will reduce the rate of nucleation in conventional nozzles by a factor of 50-100. In this work, it has been closer to the upper end of this range and often exceeded it, giving corrections of 200-300.

Correction by Wölk and Strey (2001) In a series of experiments with H2O vapour in an argon carrier gas, Wölk and Strey (2001) found that the classical nucleation theory underpredicted the experimental nucleation rates when the process took place in very low temperatures (in the vicinity of 240 K). They produced an empirical correction of the form:

$$J = J_{CNT} exp\left(A + \frac{B}{T}\right) \tag{5.20}$$

with $A = -27.56$ and $B = 6500$. Even though this correction factor was originally developed solely for their own experiments, it was later found to achieve remarkably accurate predictions for a wide array of experimental measurements (Manka et al., 2010; Wyslouzil and Wölk, 2016). Since the micronozzles of interest here are likely to experience nucleation at very low temperatures (even below 240 K), this correction factor has also been implemented in the micronozzle simulations. Its value varies roughly between 0.02 at 273 K and 140 at 200 K.

The discussion on the model for the first stage of nucleation concludes here. Attention is now shifted to the second stage, the growth of the nucleated droplets.

5.4 Droplet growth model

Similarly to how it was done for the case of nucleation, a rate expression is used to quantify the droplet growth process as well: the rate at which the droplet radius increases/decreases as the droplet grows/evaporates.

The instant a droplet of critical size forms, its temperature is essentially equal to that of the immediately surrounding vapour. But as the vapour continues to expand in the nozzle divergent, its temperature drops at a much faster pace than that of the droplet and a temperature gradient between the two ensues. A mass-energy exchange mechanism is then established, by which cold molecules of the supersaturated vapour impinge on the droplet and coalesce on its surface, releasing energy in the form of heat. This is both due to the mere temperature difference between the two and due to the latent heat release of the vapour molecules as they transition phase. This is a complex gas-kinetic phenomenon that is not well described and cannot at present be precisely quantified. It is however known that it is strongly dependent on the local degree of flow rarefaction in the vicinity of the droplet and therefore a droplet-based Knudsen number emerges as a driving parameter (Lamanna, 2000):

$$Kn = \frac{\bar{l}}{2r} \tag{5.21}$$

The Knudsen number in Eqn. 5.21 is not to be confused with that of Ch. 3. In this particular case, the characteristic length is the droplet diameter, not the nozzle throat width. The parameter $\bar{l}$ still denotes the molecular mean free path of steam, computed according to the kinetic theory of gases (Vincenti and Kruger, 1967):

$$\bar{l} = \frac{\mu_g}{p_g}\sqrt{\frac{\pi k_B T_g}{2m}} \tag{5.22}$$

where m is the molecular mass of water vapour, k_B is the Boltzmann constant and the rest of the parameters are as previously defined.

The heat balance across the droplet may be written as (Lai and Kandambi, 1993):

$$(h_g - h_p)\frac{dm_P}{dt} = \alpha_P \lambda_g (T_p - T_g) + m_p C_{p,L}\frac{dT_p}{dt} \tag{5.23}$$

where h_p is the enthalpy of the droplet, $(h_g - h_p)$ denotes the latent heat released per unit mass of vapour upon condensation, $\frac{dm_P}{dt}$ is the mass change of the droplet as it condenses/evaporates, λ_g is the coefficient of convective heat transfer from the gas to the droplet, T_p is the droplet's temperature and r its radius. The right-most term, which resembles the internal energy flux of the liquid droplets, is typically much smaller than the other two and may be neglected. This is partly because the droplets are minuscule and so their heat capacity is essentially negligible and partly because in a supersonic nozzle flow the thermal relaxation time of the droplet is orders of magnitude shorter than that of the flow and hence the term $\frac{dT_f}{dt}$ tends to zero (Lamanna, 2000). The equation may be re-written as:

$$4\rho_L \pi r^2 (h_g - h_P)\frac{dr}{dt} = 4\pi r^2 \lambda_g (T_p - T_g) \tag{5.24}$$

which allows for solving for the desired parameter, the rate of droplet growth (taken as positive in case of condensation and negative for evaporation):

$$\frac{dr}{dt} = \frac{\lambda_g (T_P - T_g)}{(h_g - h_P)\rho_L} \tag{5.25}$$

In solving for this parameter, expressions are needed for λ_g, T_p and h_p. These are deduced as described

in the following paragraphs.

5.4.1 Coefficient of gas-droplet convective heat transfer

There are numerous expressions in literature for λ_g, but the most widely used one, with the additional benefit that it is suitable for use at low pressures, is the one originally derived by Gyarmathy (1976) and later corrected by Young (1982):

$$\lambda_g = \frac{k_g}{r} \frac{1}{1 + (1 - \upsilon) \frac{2\sqrt{8}}{\pi} \frac{\gamma}{\gamma+1} \frac{Kn_p}{Pr_g}} \tag{5.26}$$

where k_g is the thermal conductivity of the gas, γ is the specific heat ratio of the gas, Kn_p is the droplet based Knudsen number given by Eqn. 5.21 and Pr is the local Prandtl number of the gas. The Prandtl number is a non-dimensional flow similarity parameter which qualitatively expresses the relative significance of momentum diffusion to thermal diffusion, is defined in terms of the momentum and thermal diffusivities, respectively and follows as:

$$Pr = \frac{(\mu/\rho_g)}{[k_g/(C_{p,g}\rho_g)]} = \frac{c_{p,g}\mu_g}{k_g} \tag{5.27}$$

where all parameters have been introduced previously. Eqn. 5.26 also features a parameter υ and a correction factor $(1 - \upsilon)$, which warrant a brief discussion.

Droplet growth studies commonly employ two coefficients to approximately quantify the effectiveness of the condensation and evaporation processes, in terms of how many of the vapor molecules that impinge on a droplet actually turn into liquid or resort back to vapour and vice versa. These are correspondingly termed the condensation coefficient q_c and evaporation coefficient q_e, respectively and typically defined as (Marek and Straub, 2001):

$$q_e = \frac{\text{number of molecules condensed on the liquid phase}}{\text{number of molecules impinging on the liquid phase}} \tag{5.28}$$

$$q_e = \frac{\text{number of molecules evaporated to the vapour phase}}{\text{number of molecules emitted from the liquid phase}} \tag{5.29}$$

The coefficient q_c also emerged in the previous section during the nucleation analysis. There is currently no universally reliable way to quantify their value and it is common in high-pressure condensation studies to assume with negligible loss in accuracy that the two are equal to 1, such that both processes are perfect. However, Young (1982) noted a discrepancy between theory and experimental measurements for non-equilibrium conditions in the very low pressure range (condensation starting at ≤ 0.5 bar, as in the case of micronozzles of interest here) that could only be effectively remedied if the assumption $q_c = q_e = 1$ was void. He then correlated the two to the degree of non-equilibrium in the flow via an empirical coefficient α as:

$$\frac{q_c}{q_e} = 1 + \alpha \frac{T_f - T_g}{T_s(p_g)} \tag{5.30}$$

where the fraction on the right-hand side expresses the extent to which the flow has deviated from equilibrium saturation conditions. In this manner, he found that the droplet growth of Eqn. 5.25 agrees with experiments if a correction factor $(1-\upsilon)$ is introduced to Gyarmathy's convection coefficient expression as shown in Eqn. 5.26, with υ given by:

$$\upsilon = \frac{RT_s(p_g)}{h_{fg}} \left\{ a - 0.5 - \frac{2 - q_c}{2q_c} \left[\frac{\gamma + 1}{2(\gamma - 1)} \right] \left(\frac{RT_s(p_g)}{h_g} \right) \right\} \tag{5.31}$$

It is nowadays common to set $q_c = 1$ and adjust α to fit experiments, for which Young (1982) originally suggested a value $\alpha = 9$. However, White and Young (1993) later showed that the value of α varies for different nozzle geometries and flow conditions and can essentially only be determined after experimental data is available.

Such data is not available for micronozzles. Since the flowcases treated here are drastically different from those examined by Young (1982) (dimensions and expansion rates orders of magnitude different, temperatures much lower) and his original suggestion for α has anyway been found to differ already between conventionally scaled-nozzles, there is little reason to assume that his suggested value is suitable for our purposes. So, although the validation cases for this model presented in Sec. 5.9 do incorporate suitable values for α as given in literature, the lack of data drives us to set $\alpha = 0$ in Eqn. 5.31 for the subsequent simulations for the VLM nozzles, such that $q_c = q_e = 1$ and the condensation process is assumed perfect. While a non-quantifiable discrepancy with reality is then expected, White and Young (1993) noted that this discrepancy is generally not detrimental to the validity of the results. Furthermore, at least in the case of the nucleation rate, Bakhtar et al. (2005) noted that if the Kantrowitz correction is employed as described in Sec. 5.3, then the rate becomes essentially insensitive to variations in q_c.

5.4.2 Droplet specific enthalpy

The total specific enthalpy of a liquid droplet, h_p, follows as the sum of three constituents: the inherent enthalpy of liquid water corresponding to the local flow conditions, the kinetic energy of the droplet as it traverses the flowfield and the surface energy that maintains its shape (Gerber, 2002). Recalling that it is assumed here the droplet travels at the gas velocity:

$$h_p = h_f + \frac{|\mathbf{V}|^2}{2} + \frac{3\left(\sigma + T_p \frac{d\sigma}{dT}\right)}{\rho_f r} \tag{5.32}$$

where the liquid enthalpy h_f, density ρ_f and surface tension σ are computed as described in Ch. 4 and T_p is the temperature of the droplet, treated in the next paragraph. It was found in the present work that the right-most term, associated with the surface tension, is orders of magnitude smaller than the other two and has been neglected.

5.4.3 Droplet temperature

It was stated earlier that the rapid expansion of the vapour differentiates its temperature from that of the liquid droplet it surrounds. Gyarmathy and Meyer (1965) showed that an expression for determining the temperature of the liquid droplet may be deduced by considering the kinetic expression for the droplet growth (Lai and Kandambi, 1993):

$$\frac{dr}{dt} = \frac{1}{\rho_f}\frac{2q_c}{2-q_c}\left[\frac{p_g}{\sqrt{2\pi R T_g}} - \frac{q_e}{q_c}\frac{p_s(T_p)}{\sqrt{2\pi R T_p}} exp\left(-\frac{2\sigma}{r\rho_f R T_p}\right)\right] \tag{5.33}$$

If Eqn. 5.33 is equated to Eqn. 5.25 and the droplet growth term dr/dt is eliminated, a relation results for T_p. However, it is a rather extensive relation and one that needs to be solved iteratively, making it numerically expensive. In a later work, Gyarmathy (1976) demonstrated that an excellent approximation at no significant loss of accuracy may be obtained with a linearisation in the form:

$$T_p = T_s(p) + [T_s(p) - T_g]\frac{r}{r_c} \tag{5.34}$$

Lai and Kandambi (1993) discussed that Eqn. 5.34 has the additional benefit of offering straightforward physical insight, indicating that a sub-critical droplet will evaporate, while a stable one ($r > r_c$) will continue to grow.

All parameters needed to determine the droplet growth rate in Eqn. 5.25 are now determined and the model of the droplet growth is complete. The remainder of this chapter explains how the entire condensation model is brought together through the source terms of Sec. 5.1 and how it has been implemented numerically in OpenFOAM. But first, one last major assumption is explored, concerning whether the drag of the droplets on the flow can be ignored, as supposed in Secs. 5.2 and 5.1.

5.5 Inertial influence of the droplets on the flow

The introduction of droplets into the flow raises the question of whether their size is large enough to require a dedicated treatment of their influence on the momentum of the gas or whether they may be assumed to travel at the gas velocity. In conventional-scale nozzles, the characteristic dimensions are typically in the order of 1 cm or more whereas the droplets themselves may not have exceeded 1 µm in diameter by the time their growth has been quenched. It is then common practice to assume the droplets are too small to be of any substantial inertial influence and this indeed provides good agreement with experiments, as can be seen by inspecting many of the various works cited in this chapter. In this case however, the characteristic dimensions of the micronozzle itself are in the sub-millimetre range and the validity of this assumption comes into question. We proceed here to check it.

There is no experimental data available on the influence of nanodroplets on micronozzle flows. The only usable information at hand are a limited number of exploratory numerical studies, among which that of Greenfield et al. (2018) stands out as probably the most comprehensive investigation on the matter to date. Their work examined various flow configurations by varying three main control parameters: the throat-based Reynolds number Re_t; the mass loading of the discrete phase relative to the gas, defined as $\phi = \dot{m}_{droplet}/\dot{m}_{gas}$; and the Stokes number, which follows as:

$$St = \frac{\rho_L U d_p^2}{18 \mu_g L} \tag{5.35}$$

where ρ_p is the mass density of the particle, U is a reference velocity, d_p is the diameter of the particle and L is a reference length. The Stokes number qualitatively expresses the relaxation time of the droplet motion relative to that of the gas. A small Stokes number ($St << 1$) implies the motion of the particle closely follows that of its host gas. In the work of Greenfield et al. (2018), U was taken as the average velocity at the nozzle exit in the case of a purely gaseous flow and L as the nozzle throat diameter.

They found that for a mass loading as high as 50 % at a Reynolds number $Re_t = 780$, the droplets have a negligible inertial effect and act as tracer particles, as long as $St <= 0.01$. They did, however, also find that although the particles may present negligible drag, they do have a substantial impact on the momentum flux through the nozzle exit due to the fact that their presence displaces the neighbouring gas particles. This may prompt the conclusion that inertial effects have to be included here, but it must be understood that the flowcases they examined are different from the ones of interest here, in that the particles were inserted to the flow in addition to the already existing gas (hence the impactful displacement). Instead, here the droplets appear as a subtraction of mass from the already existing gas, instead. It was also explained in Sec. 5.2 that the mass fraction does not exceed 0.1. These facts are used here to make the assumption that the particles will not cause any appreciable displacement to the gas when they form and that upon formation, they will act as tracer particles for $St \leq 0.01$. The findings of Greenfield et al. (2018) may then be used for a back-of-the-envelope calculation to deduce a rough threshold for the maximum droplet size that may be accommodated without requiring the

inclusion of drag effects.

For this calculation, $L = 40\,\mu m$, the gas viscosity is taken at a temperature of 300 K as $\mu_g = 1 \times 10^{-6}\,Pa \cdot s$, the liquid density is assumed as $\rho_L = 1000\,kg/s$. The average exit velocity is approximated from preliminary droplet-free simulations as $U = 750\,m/s$. With parameters along these values it follows that the allowable droplet diameter is in the order of $10^{-8}\,m$. The short timeframes involved in the micronozzle flow make it unlikely that a liquid critical cluster forming at a diameter in the order of 10^{-10}-$10^{-9}\,m$ will have sufficient time to substantially exceed this threshold (this is confirmed in Ch. 7). On the basis of this, the inertial effects of the droplets are then ignored for the remainder of this work. The droplets are assumed to travel at the gas velocity.

5.6 Inclusion of the second phase in the conservation equations

Finally, it is possible to formulate the source terms presented in Sec. 5.1 and close the system of equations in the condensation model.

The source term in the equation for the conservation of the number of droplets (Eqn. 5.5) expresses the generation of new droplets by means of nucleation from the vapour. This process is described by the nucleation rate J, computed as described in Sec. 5.3. Then, it follows simply that:

$$S_N = J \tag{5.36}$$

Recall that while the droplet number N itself is expressed in units of "droplets per unit mass of vapor", J instead bears units of "droplets per unit volume of vapor per second"[1], so that Eqn. 5.5 is dimensionally consistent.

The remaining source terms are associated with the subtraction/addition of mass from/to the vapour as droplets are first nucleated and then grow or evaporate. For a droplet of mass m_p, this can be denoted as $\frac{dm_p}{dt}$ and under the assumption of a perfectly spherical droplet of surface area $\alpha_p = 4\pi r^2$, one may write:

$$\frac{dm_p}{dt} = \alpha_p \rho_f \frac{dr}{dt} \tag{5.37}$$

where dr/dt is given by Eqn. 5.25. The system of equations can be closed by noting that the droplet mass and the corresponding droplet radius are related to the governing variables Y and N via:

$$m_p = \frac{Y}{N} \quad \rightarrow \quad r = \left(\frac{3Y}{4\rho_f \pi N} \right) \tag{5.38}$$

It is stressed again that all droplet dimensions are average and refer to an assumed average droplet size, sufficiently representative of whatever distribution of sizes may exist in the flow in reality. With that information at hand, the rest of the source terms follow as:

$$S_Y = S_{nucl} + S_{growth} = \frac{4}{3}\pi r_c^3 \rho_f J + N \bar{\alpha}_r \rho_f \frac{dr}{dt} \rho_g \tag{5.39}$$

$$S_U = -\mathbf{v} \cdot S_a \tag{5.40}$$

$$S_h = -h_p \cdot S_a \tag{5.41}$$

where h_p is the total enthalpy of the droplet, given by Eqn. 5.32, which can also be expressed in terms

[1] In literature, J is instead often found in units of droplets per unit mass of vapor per second, but then Eqn. 5.11 has to be adjusted accordingly

of the total enthalpy of the gas and the latent heat released upon condensation as $H_g - h_{fg}$. The appearance of the momentum source term S_U may at first appear in conflict with the discussion of Sec. 5.5, but one should notice it does not denote any drag effect of the droplets on the flow; it instead merely represents the internal loss of momentum from the gaseous phase by the fact that a portion of it has been turned into liquid.

Lastly, it is noted that, as described in the original reference of Gerber (2002), equation 5.39 only contains the latter term, related to the droplet growth. It is unclear why the authors chose to neglect the contribution of the nucleation itself or how the value of Y is then initialised when the first droplets nucleate. In any case, it is physically meaningful to include it and so has been done here.

5.7 Numerical implementation

The previous sections have described the approach for the modelling of the metastable condensation in the nozzles, which as has already been explained is largely faithful to the work of Gerber and Kermani (2004). This section provides details on the numerical implementation of the model, which is inherently different from that work, due to the different solvers involved.

5.7.1 Numerical implementation of the governing equations

To maintain consistency, the conservation equations for the droplet number N and the liquid mass fraction Y stay adherent to the existing methodology of the rhoCentralFoam solver, as described in Greenshields et al. (2009).

Refer to Fig. 5.3, which illustrates any two neighbouring control volumes in the computational domain. The cells interface is denoted by f and the vector normal to the face (that helps define the fluxes of properties from face to face) by S_f.

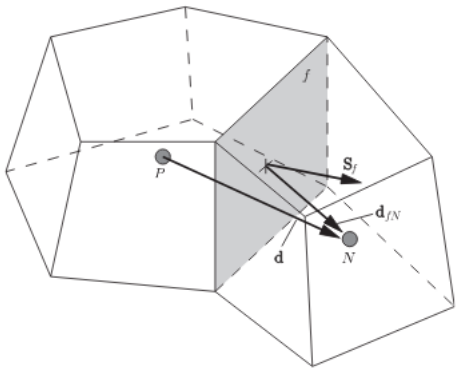

FIGURE 5.3: Schematic of neighbouring control volumes in the computational domain. Extracted from Greenshields et al. (2009).

Adopting the original authors' notation, if any of these two variables of interest (Y/N) are denoted by $\mathbf{\Psi}$ then the corresponding conservation equation may be written as:

$$\frac{\partial \rho \mathbf{\Psi}}{\partial t} + \boldsymbol{\nabla} \cdot [\mathbf{u}(\rho \mathbf{\Psi})] = S_{\mathbf{\Psi}} \tag{5.42}$$

where $S_{\mathbf{\Psi}}$ denotes the source term of the respective equation.
As is standard finite-volume CFD methodology, the convective term is integrated over each control volume, converted to a surface integral by Green's theorem and then linearised as:

$$\int_V \boldsymbol{\nabla} \cdot [\mathbf{u}(\rho\boldsymbol{\Psi})] = \int_S d\mathbf{S} \cdot [u\boldsymbol{\Psi}] \approx \Sigma_f \mathbf{S}_f \cdot \mathbf{u}_f \boldsymbol{\Psi} = \Sigma_f \phi_f \boldsymbol{\Psi}_f \tag{5.43}$$

the last term representing the sum of the volumetric fluxes of the variable $\boldsymbol{\Psi}$ through each of the faces f of the given control volume. To account for the fact that transport of information in a compressible flow also takes place by the propagation of waves on top of convection, the flux at any given face is split in an outward (+) and inward (-) direction, with each component being assigned a weight α:

$$\Sigma_f \phi_f \boldsymbol{\Psi}_f = \Sigma_f [\alpha \phi_{f^+} \Psi_{f^+} + (1-\alpha)\phi_{f^-} \Psi_{f^-}] \tag{5.44}$$

The weight α is based on the local volumetric flux ψ_f at the local speed of propagation at the cell face, which is in turn associated to the local speed of sound c in each direction $\left(c_{f_\pm} = \sqrt{\gamma R T_{f_\pm}}\right)$.

$$\psi_{f+} = max(c_{f+}|S_f|) + \phi_+, c_{f-}|S_f|) + \phi_-, 0) \tag{5.45}$$

$$\psi_{f-} = max(c_{f+}|S_f|) - \phi_+, c_{f-}|S_f|) - \phi_-, 0) \tag{5.46}$$

In the method of Kurganov and Petrova (2007) which is used by rhoCentralFoam, the weight α is then expressed as a function of the volumetric fluxes and then biased in the upwind direction as:

$$\alpha = \frac{\psi_{f+}}{\psi_{f+} + \psi_{f-}} \tag{5.47}$$

In this work, the variables Y and N are always reconstructed from the cell faces based on a second-order upwind scheme, to help tackle the steep gradients that result at the location of onset of nucleation.

Linearisation of the source terms

Without going much into the details, which the reader can find in any standard textbook on computational fluid dynamics (e.g. Versteeg and Malalasekera (2007)), it suffices to say that in finite-volume methods, convergence of the solution to any of the governing equations is promoted when the matrix containing the coefficients of the discrete equation set is diagonally dominant. That is, the entries along the diagonal are larger in magnitude than the rest of the entries along their respective rows combined.

The source terms in Eqns. 5.2 and 5.5 depend on the variable that is being solved for, Y and U respectively. As metastable condensation is quite an impulsive phenomenon, it can happen that in the condensation region the rate of the variation of these source terms is larger than that of the rest of the terms in their equation. If they are directly included in the solution matrix, they can negative affect its dominance and hence degrade the solver's convergence behaviour. A relatively simple and effective way to amend this mathematically, is to linearise the source term into an active and a passive component.

For example, in the case of the liquid mass generation source term S_Y in Eqn. 5.4, one may write (using approximately the notation of Gerber and Kermani (2004)):

$$S_Y = S_{Y,o} + S'_Y (Y - Y_o) \tag{5.48}$$

where the "o" subscript denotes the old timestep values and the prime denotes the active coefficient, i.e. the derivative of the source term with respect the variable being conserved, here Y. Based on Eqn. 5.39, these follow as:

$$S^o_Y = \frac{4}{3}\pi r_c^3 \rho_f J + N \bar{\alpha}_r \rho_f \frac{dr}{dt} \rho_g$$

$$S'_Y = \frac{3\rho_g}{r}\frac{dr}{dt}$$

A similar modification follows for the momentum source term. Then, the code is configured such that the active term is only included in the solution matrix if it is negative, to guard the solution's convergence.

5.7.2 Bounds on parameters of the liquid phase

At the nucleation front, the region in the flowfield where condensation first appears, the magnitudes of the values of the nucleation rate J, liquid mass fraction Y, droplet number N and radius r are susceptible to numerical artefacts (divisions by zero, nonphysically high/low values, etc). A few steps are implemented to keep the solution manageable.

An examination of Eqns. 5.11 and 5.8 shows that J is implicitly dependent on the logarithm of the supersaturation ratio. The discussion in section 2.5 implied that this ratio smoothly transitions from less to greater than unity during the expansion process. However, at unity, the ratio in the term $ln(S)$ becomes zero and leads to an undefined form for the critical radius. This is simply the mathematical manifestation of the fact that droplets do not start developing before the vapour becomes saturated. Hence, condensation calculations are performed only after $S > 1+E$, where E is the machine precision and the nucleation rate - which, recall, has units of #/unit volume of vapour/second - is assumed to become effective only when $\rho_g J \delta t > 1 + E$, with δt being the running timestep. That is, only after at least one cluster has nucleated in the running control volume of the mesh.

Similarly, the expression for the droplet growth rate is dependent on the droplet radius, which is only defined at the presence of droplets of radius $r \geq r_c$. An additional threshold is needed, such that the growth rate is computed only when the number of droplets per unit mass of vapour N is greater than unity. Numerically this must be expressed as the number of droplets per control volume. For a computational cell of volume V_{cell}, the threshold becomes $\rho_g N V_{cell} > 1 + E$

The smallest radius that a liquid cluster can attain is that corresponding to two molecules that have bonded. This is assumed here to be equal to the diameter of the single molecule, approximately 2.75×10^{-10} m and a minimum threshold has been placed for the radius at that value. A minimum threshold is also convenient for Y. This value can be arbitrary and here we adopt $Y = 10^{-12}$ after the work of Hric and Halama (2015).

Lastly, on the basis of the discussion in Sec. 4.10 on ignoring the freezing of droplets, the condensation model is deactivated when $T < 173.16$ K, to save some computational time. For the micronozzles treated here, this only happens substantially downstream of the nozzle exit, such that the flow topology inside the micronozzle is not affected.

5.8 Algorithmic summary of the model

For the reader's convenience, a summary of the condensation model (which, recall, is only one component of the total model) and an overview of its implementation in the form of pseudo-code is listed in Algorithm 1. This contains only the top-level steps. The reader should understand that the implementation in OpenFOAM of the condensation model as described in the preceding sections and of the thermophysical model outlined in Ch. 4 entail a myriad of architectural particularities that have been skipped here for the sake of brevity. The source code is too extensive to list in this work, but it can be provided to the interested reader upon request.

Algorithm 1: Pseudo-code of the condensation model

```
for each cell in the domain do
    Compute saturation properties;
    if ρNV_cell < 1.0 and/or Y < 10^-12 then
        Set Y and N to zero;
    end
    if T < T_crit and T < T_s(p) and T ≥ 173.16 then
        Compute liquid thermophysical properties at local conditions ;
        if ρNV_cell > 1.0 and/or Y > 10^-12 then
            Compute droplet radius from Y and N;
        else
            Set droplet radius to zero;
        end
        if Saturation ratio ≥ 1 then
            Compute change in Gibbs free energy;
            Compute critical radius;
        else
            Set critical radius to zero;
        end
        if r_p ≥ r_c and r_p ≥ r_min then
            Compute droplet growth rate;
            Compute droplet growth portion of mass generation source term;
        else
            Set both terms to zero;
        end
        if r_c > r_min then
            Compute nucleation rate;
            if J · V_cell · δt < 1.0 then
                Set nucleation rate to zero;
            end
        else
            Set critical radius and nucleation rate to zero;
        end
        Compute the rest of the source terms;
    else
        No supercooling → Set all condensation terms to zero;
    end
end
```

5.9 Validation of the two-phase model

There are various experimental datasets available in literature for the validation of condensation models, with some of the most commonly cited being those of Barschdorff et al. (1972), Moses and Stein (1978b) and Moore et al. (1973). Typically, the authors will have recorded the pressure and possibly also the droplet size along the nozzle centerline, as these are representative manifestations of the occurrence of condensation and also easier than other parameters to probe.

In this work, the (rather popular in literature) nozzles A and B are chosen from the work of Moore et al. (1973), who also provide data of pressure and a single droplet size measurement along the centerline. There are primarily three reasons motivating this choice:

- The nozzles operate in very low pressure conditions, comparable to those found in the expanders of the micronozzles examined in this work: the stagnation pressure is at 25 kPa, giving a pressure of roughly 4-6 kPa in the expander. The rapid expansion in the micronozzle against near-vacuum conditions will drive the pressure from 1-5 bar at the inlet to similar values in the expander.

- The original nozzle shape used by Moore et al. (1973) consisted of a parabolic-like convergent section attached to a straight, conical divergent section. The interface at the nozzle throat was not smooth and created a sharp discontinuity (turning corner). This discontinuity causes the generation of expansion fans that propagate into the expander section, creating a complex interference pattern with the condensation-affected flow, that results in benign oscillations in the pressure field. As such, it provides a good test to the solver's ability to reproduce a less-than-basic condensation flowfield.
- Unlike other experiments (e.g., those of Barschdorff et al. (1972)) where the nozzle shape is very smooth and the influence of the boundary layer can perhaps be neglected, here the boundary layers, even though very thin, play an important role. The aforementioned discontinuity at the throat is partly submerged in the boundary layers, meaning that the expansion fans are partly attenuated. A good agreement with experiments will ensue only if the viscous influence of these layers can be captured (as is evident by, e.g., comparing the inviscid simulations of Blondel (2014) to the viscous simulations of Gerber and Kermani (2004)). This also provides a good test for the solver, especially since the boundary layers have a driving influence on the micronozzles tested later.

The original nozzle geometry is depicted in Fig. 5.4. Inconveniently, the geometry of the parabolically-shaped convergent section was not documented by the original authors. As such, it is customary in literature to replace the parabolic section with a straight conical shape that features the same diameter at the inlet and throat sections. It turns out that the precise convergent shape does not influence the results (which can also be seen in the close agreement with experimental data in the convergent section in Fig. 5.5), so this approach is adopted here. The corresponding adjusted geometries are plotted in Figs. 5.5a and 5.5b.

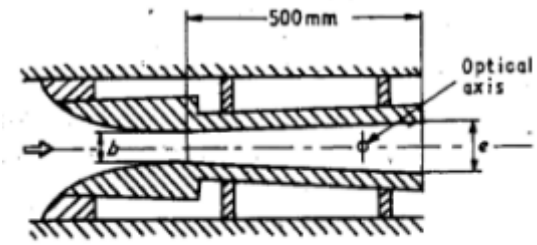

Nozzle	A	B	C	D	E
b (mm)	63	100	120	127	140
e (mm)	114	144	150	148	157

Width of each nozzle is 152 mm

FIGURE 5.4: Geometries of the nozzles of Moore et al. (1973), as shown in the original publication. Depicted is the best image quality available to the present author.

Briefly, the simulation setup is as follows. The experimental nozzles were planar, with a substantial distance from the side walls, hence the simulations are two-dimensional. The internal topology is modelled by a fine mesh of roughly 20k cells, in which heavy emphasis is placed near the wall such that the boundary layers can be sufficiently resolved. At the inlet, stagnation pressures and temperatures according to the original work are set as boundary conditions, whereas at the outlet all parameters are allowed to vary freely according to Neumann zero gradient conditions, as is suitable for a pressure-driven supersonic nozzle flow. The walls are modelled as adiabatic (i.e., temperature gradients are zero at the walls, such that no heat exchange takes place) and friction is accounted for, with the viscosity (and all other thermodynamic parameters) modelled as in Ch. 4. Taking advantage of symmetry, only the upper half of the nozzle is modelled and symmetry boundary conditions are imposed along the centerline. The condensation coefficients of Eqn. 5.26 are set as $q_c = 1$ and $\alpha = 5$, following

the suggestions of Young (1992). In this and the following simulations, the linearisation method is chosen for the implementation of the source terms. The simulations are initialised with the internal pressure field set at 6 kPa and the temperature a couple of degrees below the stagnation value, such that the flow quickly chokes at the nozzle and convergence is promoted. The cases would typically reach convergence within 1 s of virtual simulation time. Furthermore, to save computation time, the first 0.5 s would be run with the thermodynamics modelled under the ideal-gas assumption, which is a good first approximation and much faster to compute. The nominal thermodynamic model would then be activated until the final convergence was reached.

In addition, Gerber and Kermani (2004) suggested that nozzle A is better modelled if the effects of benign turbulence are accounted for. The modelling of turbulence is a science in itself, but not very relevant for the rest of this work, so we will not go into detail here. It suffices to say that the numerical implementation of the governing equations in OpenFOAM has been extended such that the transport of gaseous and liquid properties by turbulent diffusion is captured in the model, exactly as described by the above work of Gerber and Kermani (2004).

The results of the simulations are plotted in Figs. 5.5c and 5.5d. The left-hand vertical axis lists the pressure ratio and the right-hand axes - which, note, is logarithmic - features the droplet radii values. Only a single droplet size has been reported by the original author, although as Young (1992) has explained, when this is accompanied by pressure measurements, it is sufficient in its own right for validation purposes. It can be seen that the agreement with experiment is very good. What is particularly notable is how closely the droplet radii are predicted, the agreement in both instances being almost exact. This is somewhat positively surprising, given that the monodisperse droplet averaging approach adopted here neglects the variability in droplet sizes.

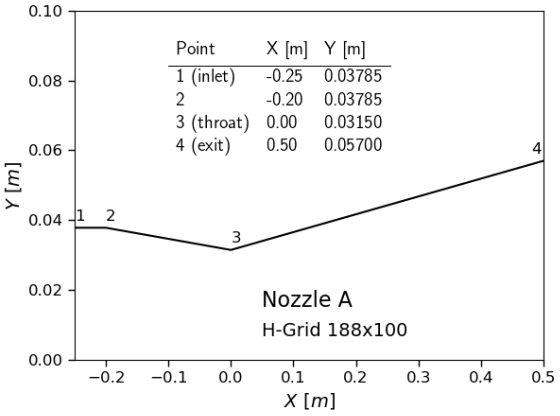

(a) Geometry of nozzle type A

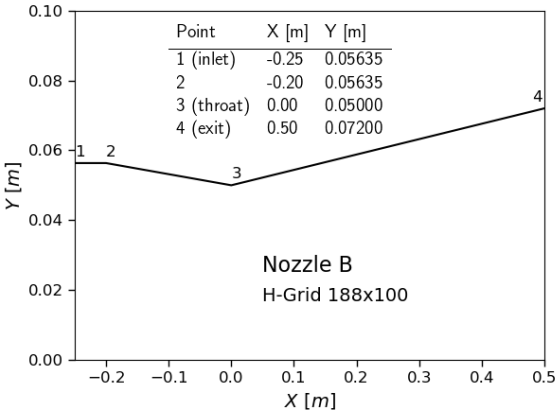

(b) Geometry of nozzle type B

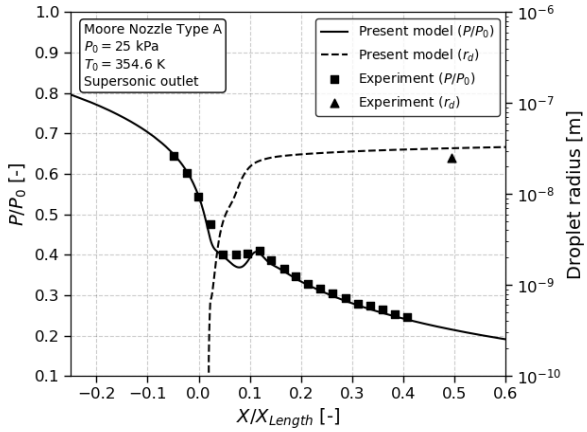

(c) Simulations vs experiment for pressure ratio and droplet radius data of nozzle A

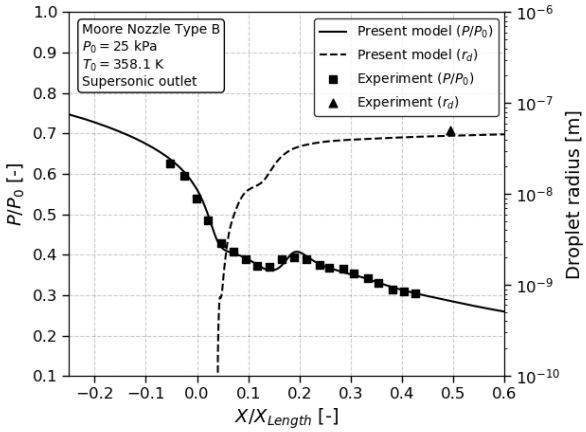

(d) Simulations vs experiment for pressure ratio and droplet radius data of nozzle B

FIGURE 5.5: Validation of the two-phase model against the experiments of Moore et al. (1973). All measurements are along the nozzle centerline. The simulations have been run on hexahedral 188x100 grids, heavily weighted near the wall and downstream of the nozzle throat, such that the boundary layers and the nucleation fronts are sufficiently resolved.

In view of the above results, the condensation model is assumed validated. Before we move on, however, it is instructive to take a look at how the primary parameters of these flows evolve, to gain a basic overview of what actually happens inside the nozzle when condensation occurs. To that end, a selection of representative vapour and liquid parameters have been sampled from the simulations along the centerline of nozzle B and are plotted in Figs. 5.6 and 5.7.

It can be seen that as steam starts expanding in the nozzle, the saturation ratio (Fig. 5.6c) quickly climbs above 1 and keeps rapidly increasing to a maximum just above 8. Correspondingly, the temperature (Fig. 5.7a) dives almost 40 degrees below its saturation value. The increase in supersaturation decreases the local value of the critical radius, which makes it easier for stable droplets to form. Liquid clusters nucleate at rates in the order of 10^{20} and immediately start to grow. As droplets condense and grow (liquid mass generation rate rises in Fig. 5.6e) and wetness rises (Fig. 5.6f), latent heat is released and subcooling decreases. The resulting pressure rise decreases the supersaturation ratio, until the flow has reached equilibrium. Once the degree of supersaturation has decreased enough for nucleation to stop, no more droplets are generated and the number of droplets (Fig. 5.7b) stays approximately constant (the small variation being due to convection). It can be seen that the mass generation rate reaches its maximum just as the supersaturation rate returns to the vicinity of 1. It

drops afterwards but does not immediately vanish; droplets continue to grow as long as the vapour remains supercooled. The pressure increase slows the expansion and causes a deceleration of the flow, evident in the dip in the velocity curve (Fig. 5.7d). The increase in temperature raises the sonic velocity, so also the Mach number drops (Fig. 5.7c). Eventually, the decrease in velocity decreases the propulsive effectiveness of the nozzle, whereas the entropic losses that have resulted from the release of heat damage its effciency.

5.9.1 Validation for micronozzle flows

The above cases have confirmed that the condensation model functions well. However, the nozzles tested are not classifiable as micronozzles, nor does the temperature inside them drop below 273 K, which is a turning point in the thermophysical model. Ideally, it would be desirable to also test the model in representative micronozzle conditions, such as to assess its response against extremely rapid expansions and very cold temperatures. Inconveniently, this has not been possible in this work.

Following an extensive literature research, the author could trace only three candidates as suitable validation cases. Moses and Stein (1977) tested condensation and droplet freezing for a wide array of nozzles and operating conditions, some of which operated in the cryogenic regime. Unfortunately, the cases that would be of interest here are not thoroughly documented and hence not usable for our purposes. In a more recent work, Bobbert et al. (2002) did in fact use a micronozzle with the specific purpose of controllably producing small water clusters in the expander. However, that work took place in a different scientific context and the type of data given is not usable here either. The earlier cited work of Manka et al. (2012) does actually provide usable data, as it recorded pressure/temperature and droplet measurements along the centerline of small cryogenic nozzles exhibiting very fast expansion[2]. Unfortunately, however, their work did not treat pure steam, but rather a small mass fraction of steam in a carrier argon gas. To reproduce this here, the model would have to be able to capture not only the phase exchanges of steam itself, but also the thermodynamic interactions between steam and the carrier gas. This is not presently possible in the model and would have taken substantially more effort than has already been expended to achieve it.

For these reasons, a validation on micronozzle-representative case is not run and it will have to be assumed that if the model accurately captures condensation in cases such as above, it will also satisfactorily do so in the case of micronozzles. In that regard, uncertainty is likely to stem from mainly two sources:

- That there is increasing ambiguity involved in the determination of the liquid properties when the flow temperatures drop to the vicinity of 235 K or below that, as was explained in Ch. 4.
- That it is conceivable the rarefaction of the flow inside the micronozzles may impact the validity of the nucleation rate, as given by Eqn. 5.11. As was briefly mentioned, the derivation of this expression assumes a gas in equilibrium, an assumption that also implicitly finds its way into the Gibbs free energy expression that serves as the basis for the nucleation analysis. However, as was explained in Ch. 3, the rapid expansion may push the translational and rotational degrees of freedom of both the gas and the freshly nucleated clusters out of equilibrium, raising questions on what the macroscopic impact of that may be. Brief discussions on these matters can be found in the works of Sharaf and Dobbins (1982), Zhong et al. (2005) and Jansen et al. (2009).

The examination of these issues will have to be left to future work and based on all preceding discussions, it is assumed here that the two-phase model is suitable for the present purposes. That being said, it is now time to finally proceed with the actual simulations, which is treated in the remainder of this work.

[2]The nozzle geometry, not documented in the original work, was obtained via personnal communication with the authors.

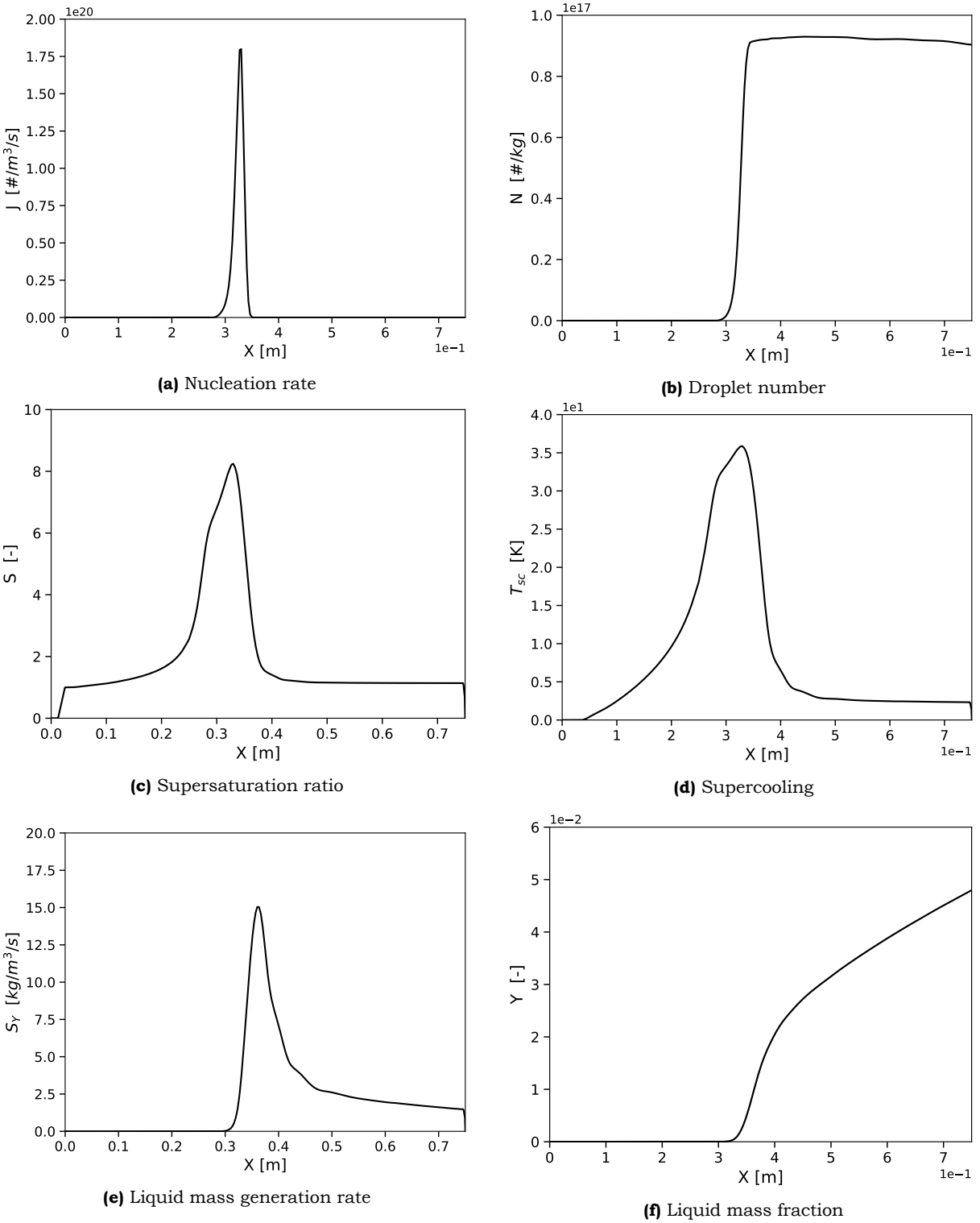

(a) Nucleation rate

(b) Droplet number

(c) Supersaturation ratio

(d) Supercooling

(e) Liquid mass generation rate

(f) Liquid mass fraction

FIGURE 5.6: Evolution of condensation parameters along the centerline for Nozzle B of Moore et al. (1973). The nozzle inlet, throat and outlet are, respectively, at X=0, X=0.25 and X=0.75.

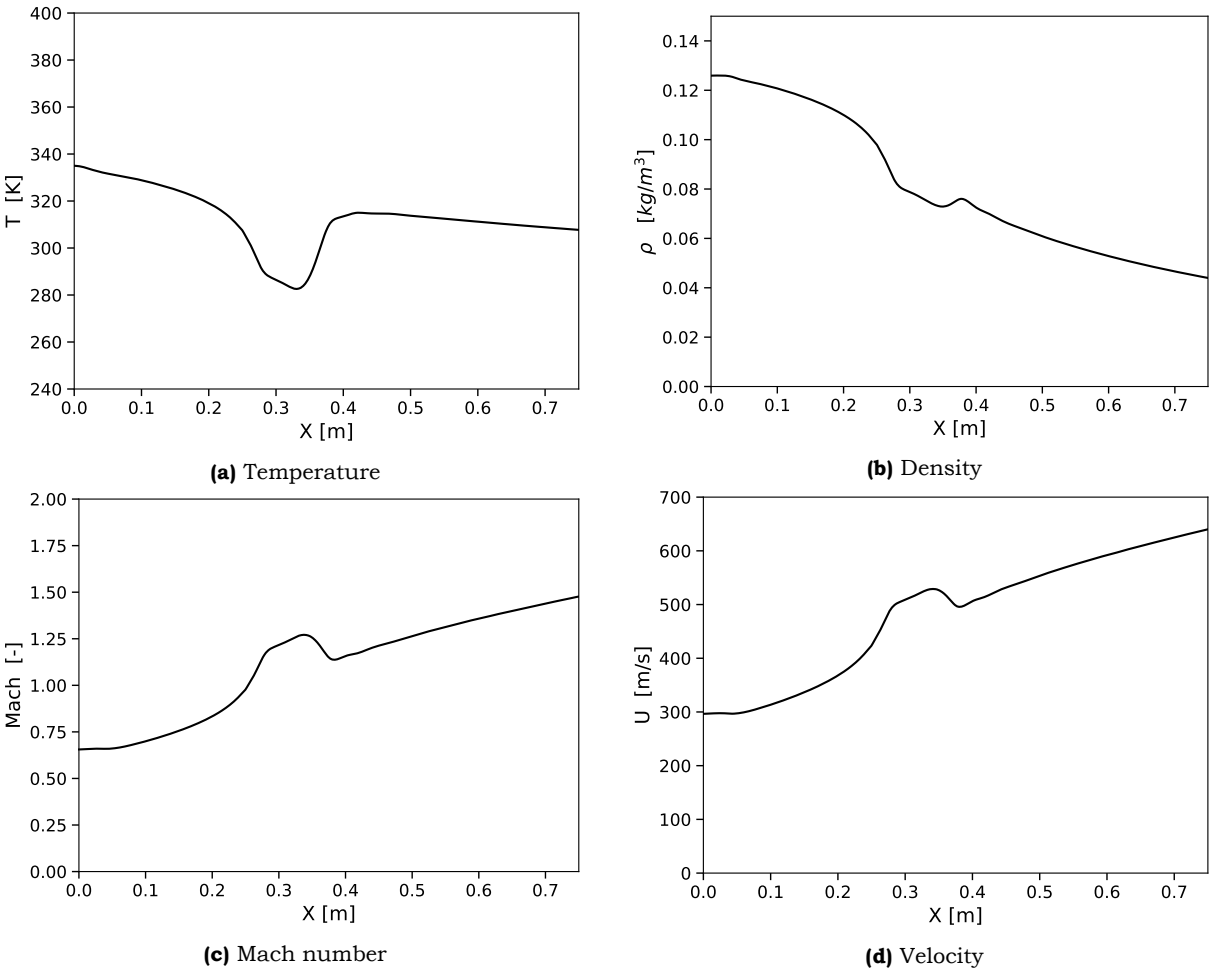

(a) Temperature

(b) Density

(c) Mach number

(d) Velocity

FIGURE 5.7: Evolution of flow parameters along the centerline for Nozzle B of Moore et al. (1973). The nozzle inlet, throat and outlet are, respectively, at X=0, X=0.25 and X=0.75.

Part IV

Numerical setup and results

CHAPTER 6

Preparation of the simulations

6.1 Geometry

The micronozzles treated in this work are of planar convergent-divergent shape. The geometry is adopted from the past TU Delft work of Ganani (2019), to maintain some consistency and continuity. The convergent and expander regions are connected via a curved throat duct. Three different geometries are examined. In all instances, the convergent section angle is kept fixed and the divergent angle is varied, in a manner such that the area ratio between the throat and exit stays the same in all instances. A schematic of the generic geometry is given in Fig. 6.1, with the corresponding dimensions listed in Table 6.1. The computational mesh comprises of roughly 105000 cells. The nozzle section exhibits 100x20x10 cells in the "length x width x depth" directions. As it is known that there is a toll in the validity of the results unless the outlet downstream of the nozzle exit is also included (Ivanov et al., 1999), the domain is extended a distance equal to 8, 6 and 6 nozzle exit widths in the downstream, lateral and normal directions, respectively. Taking advantage of the symmetry of the geometry along the xy and xz midplanes, only 1/4th of the domain is simulated, such that the computational cost is reduced. An overview of the mesh is given in Figs. 6.2 and 6.3.

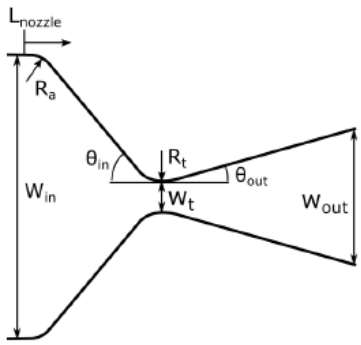

FIGURE 6.1: Geometric features of the micronozzles treated in this work. Extracted from Ganani (2019).

Table 6.1: Geometric parameters of the micronozzles treated in this work. Extracted from Ganani (2019).

Parameter	Value
Convergent half-angle (θ_{in})	45°
Expander half-angle (θ_{out})	15°, 30°, 45°
Inlet width (W_{in})	3 mm
Throat width (W_t)	45 µm
Nozzle length (L_{nozzle})	2893.04, 2177.4, 1917.63 µm
Area ratio (ϵ)	16.971 [−]
Convergent curvature ratio $\left(\frac{R_a}{W_{in}}\right)$	0.005 [−]
Throat curvature ratio $\left(2\frac{R_t}{W_t}\right)$	1 [−]

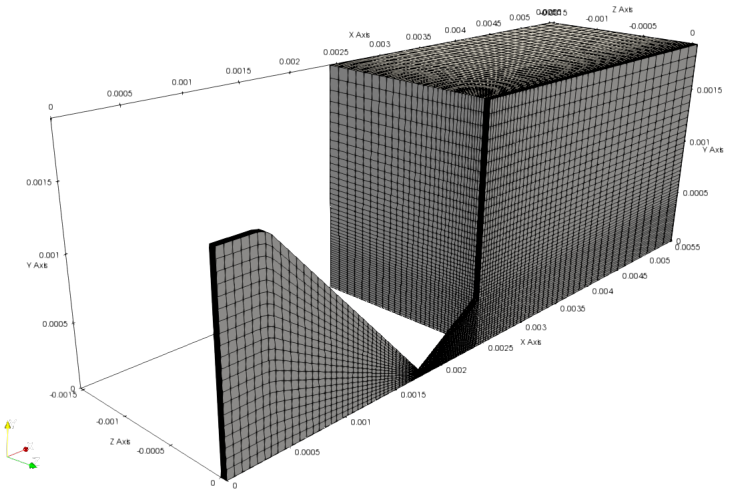

FIGURE 6.2: Overview of the computational domain

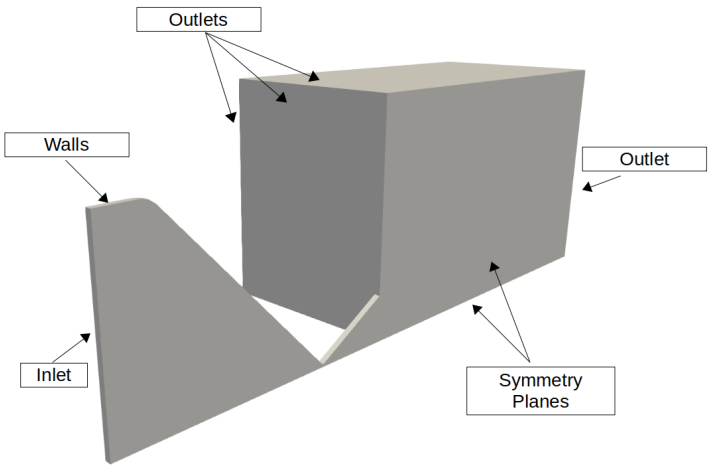

FIGURE 6.3: Overview of the computational domain boundaries

6.2 Control variables and baseline configuration

In the preceding chapters, it was shown that the condensation mechanism in the nozzle depends primarily on the degree of supersaturation and the local flow conditions, particularly the pressure and temperature. In turn, these are mainly influenced by the inlet flow conditions and the geometry of the nozzle. Since these two factors are also the primary design drivers for the nozzle performance in general, it has been decided to use 4 related control variables in this study and examine how the condensation process, if any, varies with these parameters relative to a selected baseline case. These parameters and their settings are:

- Stagnation pressure at 1, 3 and 5 bar
- Stagnation temperature at 473, 573 and 673 K
- Expander angle at 15, 30 and 45 deg
- Nozzle depth at 100 and 200 µm

The choice of these particular parameters is motivated by that the stagnation conditions determine, together with the expansion rate, the flowfield in the expander; the expander angle in turn largely determines this expansion rate for a selected area ratio; and the nozzle depth is included because it was expected it will have a dominant impact on the flow via the heat input from the wall (more on that in Sec. 6.4.1).

The choice of the stagnation values themselves is somewhat arbitrary, but has been made on the consideration that they are roughly representative of the planned operational envelope for these resistojets (van Wees et al., 2016). Angles in the range 15-45 deg cover the range typically employed in micronozzles, as it has been found that values lower than 15 deg will generally result in fully subsonic flow due to boundary layer growth in the expander over a wide range of operating conditions, whereas values higher than 45 deg induce excessive expansion losses (Louisos and Hitt, 2008). Concerning the nozzle depth, values from experiments reported in literature generally vary between 10-300 µm (Louisos and Hitt, 2008), even though higher values of 600 µm or more have been reported (Louisos et al., 2008). Generally, it is recommended that the depth is not lower than 50 µm, because otherwise the interference from the boundary layers along the walls becomes excessive and the flow remains subsonic over most common operating conditions (Louisos and Hitt, 2012); depths above roughly 300-400 µm become increasingly challenging for the deep reactive ion etching (DRIE) micro-production technique typically applied in TU Delft for manufacturing VLM nozzles (Silva et al., 2017; Tang et al., 2018). In a past TU Delft work, Silva et al. (2018a) used nozzles with a 100 µm depth and this was later adopted in the work of Ganani (2019), so this has also been used as a baseline here. It was then decided to simply double the value to 200 µm of depth for a second simulation, to offer a clear comparison and insight into the effect of this parameter.

Concerning the choice of the baseline simulation parameters, it is useful to choose a configuration of practical interest. As was explained earlier, the VLMs at TU Delft are developed with a range of target operational conditions in mind and, at this preliminary stage, there is little reason to prefer one set of conditions over another. For this work, the baseline configuration has taken the values listed in Table 6.2, which have been chosen on the basis that they are representative of this operational envelope and lie somewhere near the middle of the ranges of the conditions/geometric configurations currently considered, such that they are roughly representative of typical performance that may be expected from the nozzle.

Since a portion of the region downstream of the nozzle exit is also included in the domain, a selection must be made for the ambient conditions. The VLMs at TU Delft are experimentally characterised in-house in a dedicated vacuum chamber facility that can reach a minimum pressure of roughly 30 Pa and will typically be at ambient temperature. It was decided it would be useful for future comparisons

between simulations and experiments to have these parameters equal, so these are the ambient conditions selected in this work. The wall temperature is set at the stagnation value, a decision motivated in Sec. 6.4.1.

Table 6.2: Parameters of the baseline micronozzle simulation

Parameter	Value
Propellant	Pure H2O
Stagnation pressure	3 bar
Stagnation temperature	473 K
Expander angle	30 deg
Nozzle depth	100 μm
Ambient pressure	30 Pa
Ambient temperature	293 K
Wall teoremperature	473 K

It must be understood that, in reality, this 30 Pa in the chamber is established either by air that could not been pumped out or by some inert gas (nitrogen, argon, etc) if the chamber has first been purged. Here, however, the simulation treats the flow of water vapour exclusively, so the assumption is implicitly made that the vacuum chamber ambience also contains water vapour. For such low pressures, it is unlikely that the precise nature of the ambient gas will have any substantial impact on the results.

Before continuing, now that the operational conditions of the VLMs have been framed, it is useful to briefly revisit the singe-phase validation case of the experiments of Rothe (1971) in Sec. 3.5.1, to get a more detailed impression of how the degree of rarefaction in the micronozzles compares to that experiment. The most rarefied micronozze flowcase here is the one featuring the lowest stagnation temperature, i.e., the 1 bar case. Fig. 6.4 compares the Knudsen contours across the midplanes of each nozzle. For the micronozzle, it has been extracted from the solution of the respective flowcase that is presented in detail later. It can be seen that the Rothe nozzle exhibits Kn about an order of magnitude higher than the micronozzle, consistently throughout the expander. This is why it was assumed in that part of the work that since the solver was in fair agreement with the experiment at those degrees of rarefaction, it is reasonable to assume it will perform satisfactorily for the micronozzle cases. It should be kept in mind that since the values of Kn are computed based on the local flow properties, the Kn values depicted deviate from reality when the flowfield itself does. Still, as it was shown that the temperature is underpredicted, the values given are likely conservative estimates.

6.3 Estimates of macroscopic performance

Indicative performance estimates in terms of the thrust, specific impulse and specific impulse efficiency are given for the cases simulated, especially to highlight the performance impact in those cases where condensation may be significant. The three parameters are chosen because they are a macroscopic manifestation of the flow properties that are typically affected by the phenomenon and they also indirectly encompass the influence of such features as the size of the viscous layers, the mass flux at the nozzle exit, etc. It should be understood, however, that these estimates are limited in extent, because the main purpose here is not to make detailed investigations of the micronozzles' macroscopic performance under all possible scenarios, but rather to assess whether condensation should be a matter of concern in a general sense.

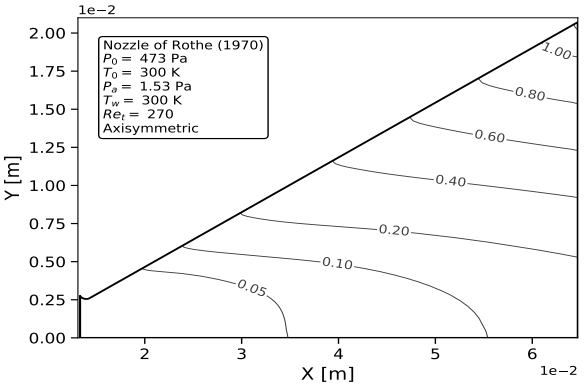

(a) Nozzle B590 ($Re_t = 270$) of Rothe (1971), operating on Nitrogen

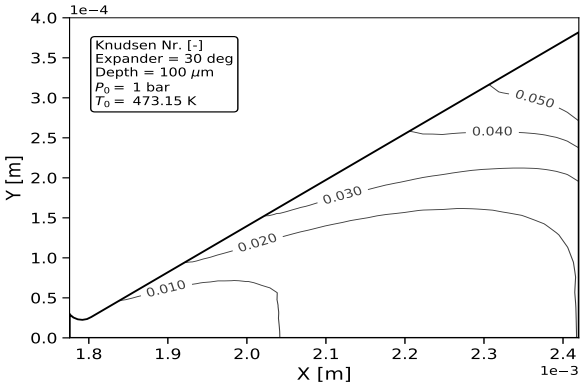

(b) VLM 100 µm-deep micronozzle with an expander angle of 30 deg, $P_0 = 3$ bar and $T_0 = 473$ K

FIGURE 6.4: Comparison of Knudsen number fields between the nozzle of Rothe (1971) and one of the micronozzle flow cases

The nozzle thrust formally follows as:

$$F_T = \int\int_{A_e} \vec{V}(\rho\vec{V}\cdot\vec{n})dA_e + \int\int_{A_e}(p-p_a)\vec{n}dA_e \tag{6.1}$$

where A_e is the nozzle exit surface area, n is the outward-pointing surface normal vector and p_a is the ambient pressure. Pearl et al. (2017) argued that the viscous stress can have a substantial impact at these scales and that the thrust expression should be augmented to read:

$$F_T = \int\int_{A_e} \vec{V}(\rho\vec{V}\cdot\vec{n})dA_e + \int\int_{A_e}(p-p_a)\vec{n}dA_e - \int\int_{A_e}(\vec{\tau}\cdot\vec{n})dA_e$$

However, the extra term was found to have a negligible contribution in this work and has been ignored, such that the thrust force is described by the original Eqn. 6.1. The determination of the specific impulse requires the mass flow in the normal direction at the nozzle exit:

$$\dot{m} = \int_A \rho(\vec{V}\cdot\vec{n})dA \tag{6.2}$$

The specific impulse itself then follows simply as:

$$I_{sp} = \frac{\int F_T dt}{g_0 \int \dot{m} dt} \tag{6.3}$$

where $g_0 = 9.807\,\mathrm{m/s^2}$ is the gravitational acceleration on the Earth's surface and the integral over time t denotes the duration of operation. In this work, we are only interested in the value of I_{sp} at any signle moment in time after the nozzle has reached steady-state operation, such that the above expression reduces to simply $I_{sp} = F_T/(g_0 \cdot \dot{m})$. It is occasionally also insightful to get an impression of how the simulated nozzle performs relative to its ideal case, as estimated by quasi-1D isentropic nozzle flow theory. In this work, this is quantified via the specific impulse efficiency, defined as:

$$n_{I_{sp}} = \frac{I_{sp,\ actual}}{I_{sp,\ ideal}} \tag{6.4}$$

where the ideal specific impulse, $I_{sp,ideal}$ may be derived as a function of the stagnation and nozzle exit properties as (Sutton and Biblarz, 2017; Louisos and Hitt, 2012):

$$I_{sp,ideal} = \sqrt{\frac{2\gamma RT_0}{g_0^2(\gamma-1)}\left[1-\left(\frac{p_{exit}}{p_0}\right)^{\frac{\gamma-1}{\gamma}}\right]} \tag{6.5}$$

For the purposes of the ideal case, the ratio of specific heats of water vapour has been assumed fixed at $\gamma = 1.33$. The pressure ratio in this relation follows from the supersonic solution of the area ratio expression from ideal rocket theory:

$$\frac{A_e}{A^*} = \frac{\sqrt{\gamma \left(\frac{\gamma+1}{2}\right)^{\frac{1+\gamma}{1-\gamma}}}}{\sqrt{\frac{2\gamma}{\gamma-1} \cdot \left(\frac{p_e}{p_0}\right)^{\frac{2}{\gamma}} \cdot \left[1 - \left(\frac{p_e}{p_0}\right)^{\frac{\gamma-1}{\gamma}}\right]}} \tag{6.6}$$

where the expansion ratio is given in Table 6.1. For a given specific heat ratio, the pressure ratio is determined exclusively by the expansion ratio in the context of isentropic quasi-1D rocket theory. Since the area ratio is the same in all nozzles examined here and the ideal rocket theory does not otherwise concern itself with the nozzle geometry, the theoretical specific impulse is the same for all simulations presented in this work, except in those cases in which the stagnation temperature is varied.

6.4 Numerical setup

This section outlines the boundary conditions used for the numerical solution of the conservation equations, the mathematical schemes implemented to reach this solution and the manner in which the simulations are initialised. This latter aspect is important for eliminating fatal numerical instabilities inherent to the solver and for accelerating the otherwise rather time-consuming simulations.

6.4.1 Boundary conditions

Inlet:

The stagnation conditions p_0 and T_0 that are used as control variables are assigned at the inlet, in a manner such that the incoming flow is subsonic compressible. For the velocity, its gradient is set to zero such that it can freely follow the pressure variation, as this is a pressure-driven supersonic flow.

Outlet:

In this case, the problem is slightly complicated by the fact that the domain downstream of the nozzle exit is also included in the simulation. This domain will not experience fully supersonic flow throughout its topology, but is instead expected to feature subsonic flow or even stagnant gas in those regions that remain only mildly or not at all affected by the supersonic jet emanating from the nozzle exit. A physically correct and numerically convenient boundary condition would then have to be able to treat the supersonic and subsonic regions of the outlet boundary separately, ideally prescribing a fixed pressure/temperature value for the subsonic portions and a supersonic condition at the supersonic regions. Unfortunately, such a condition does not currently exist in the default version of OpenFOAM.

A similar issue would have been faced in past works using the same solver, such as those of Pearl et al. (2014), Giorgi et al. (2018) and Ganani (2019). Giorgi et al. (2018) based their boundary conditions on the nozzle mass flow, which is not particularly interesting as an input parameter in the present simulations, so their approach is not applicable in the present work. Pearl et al. (2014) fixed the pressure at the outlet at 1 kPa so they would not need to account for any rarefaction effects. Manually setting the farfield outlet pressure in a supersonic nozzle jet flow will also likely affect the flow inside the nozzle itself, as the effect of the forced boundary condition propagates backwards into the computational domain. Therefore, this is also not a desired approach in the present case. Ganani (2019) implemented a wave transmissive boundary condition, which modifies the value of the property at the boundary such that a target value (for instance, the selected ambient pressure) can be approximated at some

hypothetical distance downstream of the boundary. However, his choice of this distance (just 10 µm) is so short that it is probably more damaging to the simulation than it is beneficial, while it can also not replicate the correct ambient conditions at those regions in the domain that are subsonic. What is more, he imposed velocity boundary conditions that artificially block possible backflow into the domain, which potentially makes the solutions at the outlet unphysical. Hence, this approach is not considered suitable for the present purposes either.

The present author found that the only comprehensive way to tackle the issue was to implement a new boundary condition in OpenFOAM. This condition checks if the local velocity is higher than the speed of sound and, if it is, it imposes a zero gradient condition, otherwise resorts to a stagnation condition. In the latter case, the stagnant value was set at 30 Pa according to the discussion of the previous section, such that the ambient pressure is correctly applied. The implementation of this condition was developed in an earlier work by Kraposhin et al. (2015) and has been adopted from there. There is a price to pay for this improvement in the realisticity of the solution, it being the speed of convergence. At those regions of the farfield boundaries where the interface between the subsonic and supersonic regions is located, the solver can take some time to settle on the correct configuration and, at times, may even become unstable. So, some caution is needed in the initialisation of the solution. The rest of the parameters are all assigned zero gradient conditions.

Walls:

The boundary condition at the wall is of particular importance from the perspective of the temperature, because the high surface-to-volume ratio of the nozzle implies that whatever temperature condition is set at the wall is going to dominate the flow topology. Recall from Ch. 3 that a temperature jump condition is employed, but the thermal condition of the wall still needs to be specified. The author did not want to make the typical assumption of an adiabatic wall, because it is unlikely that a wall comprising of a material as heat-conductive as silicon is going to stay unaffected when the heater is activated upstream of the nozzle and, in turn, is not going to supply heat to the flow. On the other hand, it is also not realistic to make a detailed model of the conjugate heat transfer between the flow and the wall structure, because at this stage of the design, there is little information on the final configuration of the nozzle's structure. Instead, in this work, the assumption is made that the wall is elevated and fixed at the stagnation temperature of the flow. This may seem extreme, but there is justification for it.

It is possible to obtain a rough estimate of the time it takes for the thruster's silicon substrate to heat up following the activation of the heating element, under the assumption it is a semi-infite solid (Louisos and Hitt, 2012). For the sake of simplicity, it is assumed that the heater's temperature also serves as the stagnation temperature of the flow. The characteristic thermal diffusion length for a given material can be approximated as:

$$L \approx \sqrt{\alpha t} \tag{6.7}$$

where α is the thermal diffusivity and t is the time it takes heat to traverse this length. From the data in Appendix B.2 of Rebeiz (2003) one finds, for MEMS-rated silicon, values for the thermal conductivity $k = 156\,\mathrm{W\,m^{-1}\,K^{-1}}$, the specific heat $C_p = 713\,\mathrm{J\,kg^{-1}\,K^{-1}}$ and the density ρ =2320 kg/m^3, yielding a thermal diffusivity $\alpha = 9.43 \times 10^{-5}\,\mathrm{m^2/s}$. Eqn. 6.7 is in principle valid for a point heat source, so we will assume this is located at the center of the heater, roughly 5 mm away from the nozzle exit (refer to Fig. 5.1 in Ganani (2019), for the detailed geometry). This is an extremely conservative estimate, as in reality the heater occupies a very substantial surface area and mass relative to the substrate. Even in that case, one finds a timescale t ≈0.2 s, which is very short. It is therefore reasonable to assume that the heater will raise the wall to its temperature within a negligible amount of time from its actuation. This is further supported by the fact that under nominal operational conditions, it is likely the heater will be activated until it rises to the desired temperature, before the flow is allowed into the

vapourisation plenum. From there on, in a past work, Louisos and Hitt (2012) examined the influence of heat transfer on the micronozzle performance and, based on a detailed first-order calculation, showed that the time the flow spends in the nozzle is sufficient for it to receive heat from the hot wall. On these grounds, it is accepted that setting a fixed-value wall condition in the boundary condition for the temperature, with that value set at the stagnation temperature, is a valid approach. It is notable that the validation case against the experiments of Cen and Xu (2010) in Ch. 3 utilised this condition and obtained very close agreement, which speaks to its validity.

A slip condition is employed for the velocity, as discussed in Ch. 3. For all other parameters, zero gradient conditions are set at the wall. It is also assumed that the nozzle walls are perfectly smooth. Depending on the production technique used to manufacture the nozzle, it could be that the influence of surface roughness should be examined (Torre et al., 2010), but this is left to future works. Here, the influence of the walls is indirectly expressed in the accommodation coefficients appearing in the velocity slip and temperature jump boundary condtions (Eqns. 3.11 and 3.14). The author was not able to find any data on these coefficients for the flow of rarefied water vapour in silicon microchannels and other authors (Silva et al., 2016) concur that such data is rather scarce for polyatomic mocelules in general. Arkilic et al. (2001) experimentally determined values for the tangential momentum accommodation coefficient for another, simpler, polyatomic molecule, carbon dioxide (CO2). In a recent review, Sharipov (2011) noted that this coefficient is likely not substantially affected by the internal molecular structure for polyatomic molecules. Based on the findings in these works, here values $\sigma_M = 0.8$ and $\sigma_T = 0.85$ have been adopted, which also gave good results in the validation against the experiments of Cen and Xu (2010) in Sec. 3.5.2.

Other:

The additional two droplet-related parameters N and Y are assigned zero gradient conditions everywhere in the domain, such that their evolution is exclusively dominated by the evolution of the flow itself. Potential backflow from the boundaries is artificially blocked, given this would be an unphysical situation. Since only 1/4th of the full domain is simulated, all properties are assigned symmetry boundary conditions at the two symmetry planes of the domain.

6.4.2 Numerical solution methodology

The choice of numerical schemes was targeted at achieving second-order accuracy in the discretisation of the conservation laws, as this is generally considered necessary to achieve reliable results in simulations of non-equilibrium condensation (Blondel, 2014).

To that end, the temporal terms are discretised with a Crank-Nicholson scheme (Crank and Nicolson, 1996), with a weight factor of 0.9 suggested by OpenFOAM guidelines. The divergence terms are generally taken care of directly by the method of Kurganov and Petrova (2007) that is inherent to the solver, therefore they need not be assigned a dedicated scheme. An exception is the divergence of the stress tensor, which is computed purely explicitly and has thus been treated with a simple second-order Gauss linear scheme.

A choice must also be made for the Total Variation Deminishing (TVD) limiter implemented by the algorithm of Kurganov and Petrova (2007). A comparison of various such schemes in the case of metastable condensation modelling was performed in the dissertation of Blondel (2014), who found the limiters of van Leer (1979) and van Albada et al. (1997) to give the most convenient trade-off between precision and numerical performance. Here, the latter scheme is chosen. Lastly, the reconstruction of the variables Y and N from the cell faces is not done using a TVD scheme, but rather a second-order unbounded linear-upwind scheme (Warming and Beam, 1976), to help tackle the very steep gradients that occur in the region of the flow where nucleation first starts. The Laplacian term in the energy

equation is treated with a simple gauss linear discretisation. The surface-normal gradient of the velocity in the energy equation is assigned a standard central-difference, corrected surface-normal gradient scheme. The rest of the gradient terms in the conservation laws are discretised with a least-squares scheme, whose extrapolated values are bounded by the maxima and minima of the neighbouring cells.

To maintain some brevity, the mathematical details of these schemes are skipped here and the reader is referred to the cited works. The OpenFOAM implementation may slightly differ from the original sources, so the interested reader is also advised to consult the software's user guide and source code. The described numerical setup has been used not only for the main simulations, but also for all validation cases presented in the preceding chapters.

The fact that the micronozzles exhibit throat-based Reynolds numbers in the order of 1000 or less make it unlikely that any turbulence will occur, so no turbulence model has been implemented.

6.5 Initialisation of the solution

Rather than starting the simulations with the solver at the nominal setup as described above, a dedicated initialisation procedure was implemented, aimed at addressing two problems:

Numerical instabiities

The cases simulated exhibit a pressure ratio between stagnation and outlet conditions in the vicinity of 10000, a rather high value that imposed very sharp pressure and density gradients at the start of the simulations. These gradients consistently turned out to be fatal to the solver's numerical stability, a problem that plagued this work for a long time. One method to address it would be to start at a low stagnation pressure (e.g., at a pressure ratio of 10) and then progressively step up this value over time. While effective, this is also quite time-consuming, as one has to wait for the nominal value to be reached, before the actual simulation can be ran. A faster method was found in using a basic built-in solver of OpenFOAM that solves the simple laplacian diffusion equation. This solver was slightly modified to treat the diffusion of pressure and was then used to obtain a smooth pressure field between the high stagnation value and the low ambient value, which was fed as an initial solution to the solver. It turned out to be effective in eliminating the instabilities and encouraging relatively fast convergence.

In some instances, the numerical oscillations are violent enough to drive the value of the temperature or the density negative and cause the solver to crash. To tackle this, a minimum value for the specific internal energy is manually implemented, to set a lower limit to the values that the solution of the temperature takes. This value is purely arbitrary and has been here set at approximately $2 \times 10^6\,\mathrm{J\,kg^{-1}}$, roughly corresponding to a temperature of 40 K, far below what can be expected to be found inside the nozzle. This hard-coded limit is, of course, unphysical, so it is only used as a tool to bound the simulation at its early stages. It quickly ceases to be effective as the solution stabilises.

Slow-paced execution

The algorithm implemented in the underlying solver is explicit in nature, hence limited by a maximum value for the timestep, which makes its execution rather slow. The situation is exacerbarated by the fact that the real-gas thermophysical model of water is inherently very computationally intensive, even in its somewhat reduced form described in Ch. 4. A simulation that would have been left to run in its entirety with this model, would take several days to complete. To accelerate this, the following steps were taken:

- A manual multi-grid approach is implemented, in which a solution is first obtained on a coarse mesh of 30000 cells, then mapped to the fine mesh and run until convergence. The solution in the coarse mesh is itself initialised with the laplacian solver described above.

- The simulation in this coarse mesh is not run with the actual thermophysical model, but with a much-faster rough approximation. The gas is treated fully as ideal. The enthalpy is computed linearly relative to a threshold value, with the same NIST-JANNAF convention as described in Sec. 4.8.1. The isobaric specific heat is assumed constant, set at a representative value of roughly $1800\,\mathrm{J\,kg^{-1}\,K^{-1}}$. And the transport properties are determined via Sutherland's method, with coefficients obtained from Nishii et al. (2019). This initialisation provides a good approximation to the final solution that is obtained with the nominal model of Ch. 4 on the fine mesh.

This initialisation decreases the simulation time from several days to about 24-48 hours, when run on a quad-core, 8GB RAM, Dell Precision T3600 machine. The simulation is assumed to have converged when the normalised velocity residuals have dropped below 10^{-6} and the variation of an array of parameters of interest (such as pressure at the inlet, maximum droplet radius, liquid mass generation rate, etc) has stabilised to within less than a percent.

CHAPTER 7

Results and discussion

The most notable results of the simulations are gathered in this chapter. The outputs are primarily given in the form of isoline contour plots[1] of the expander section flow, for a selection of the primary parameters: Mach number and temperature as indicators of the flow conditions, saturation and nucleation rates as drivers of the condensation, mass factions and corresponding droplet radii as the results of the condensation. This allows for a detailed but clear quantified overview of the main flow topological features. The properties have primarily been sampled along the nozzle's midplane, as it is there that the expansion mainly manifests. The outputs have been grouped according to the four control variables, i.e. stagnation temperature and pressure, expander angle and nozzle depth. For a selection of cases it is shown what effect, if any, the condensation has had on the flow. Some macroscopic performance estimates are also provided. In all instances, to aid visibility, only the expander section of the nozzle is shown (from the throat section to the exit), where also all the phenomena of interest take place. An overview of the macroscopic performance of the cases examined is offered at the end of the chapter, in Sec. 7.5.

For interpreting the results presented here, it is helpful to briefly recap some of the main aspects of the physics involved in this particular problem and of the model implemented:

- The nozzle treated is planar and has dimensions spanning no more than a couple of mm. Both the throat and the depth are only a fraction of a mm.
- The superheated steam enters the nozzle at temperatures of 200 °C or more and stays in the nozzle for no more than about 2 µs. The flow temperature drops hundreds of degrees within 1 µs and within a fraction of a millimetre.
- The walls are assumed to be fixed at the stagnation temperature. The planar wall, which has by far the most dominant contribution to the nozzle's high surface-to-volume ratio, serves as a major heat source for the expanding flow and also imposes thick boundary layers.
- The flow model and the thermophysical and condensation models come with considerable uncertainty, as has become clear in preceding sections. The results should therefore not be taken for their exact value and the focus should be placed on the general trends rather than the precise figures.

One final major point to be kept in mind is that the smallest possible physical manifestation of condensation is a dimer, i.e. a cluster of two water molecules. This has been assumed here to have a radius of about 2.75×10^{-10} m, equal to the diameter of a single water molecule (the radius in reality is likely to be closer to 3×10^{-10} m (Mukhopadhyay et al., 2018)). In some of the results that follow, the resulting radii are below this threshold and are therefore unphysical. While these results are still used to provide insights into how the control variables affect the condensation mechanisms, the reader should keep in mind that condensation is likely not to have actually occurred in these cases.

With these points in mind, a targeted presentation and discussion of the results can start.

[1] A script has been written in the Python language to import the raw CFD data from OpenFOAM and perform the post-proccessing of the results as presented here.

7.1 Effect of stagnation pressure

The variation of the total pressure allows to examine phenomena that are largely present in the rest of results presented in this chapter, as well.

Fig. 7.3 depicts the Mach/Temperature contours for each stagnation pressure and Figs. 7.4 and Figs. 7.5 list the respective results for saturation ratio/nucleation rate and liquid mass fraction/droplet radius. Recall that on all instances the walls are kept at 473 K and the outlet pressure and temperature are 30 Pa and 293 K, respectively. The nozzle geometry is the one with a 30 deg expander angle and 100 μm depth.

Firstly, the stagnation pressure has an obvious impact on the flow topology. It can be seen that at 1 bar the inertia of the flow is too low for the supersonic core to persist at the maximum Mach number until the nozzle exit and it drops from $M = 2.5$ roughly half-way through the expander to less than 2 by the exit. The low inertia gives room for thick viscous layers to develop along the walls, which in turn allows the temperature to maintain values higher than 300 K in the larger portion of the flowfield. The effect is alleviated as the total pressure is increased, with the subsonic layers becoming much thinner, the core expansion persisting largely undisturbed until the exit, the temperatures in the expander dropping to as low as roughly 210 K and the Mach number climbing to as high as 3 in the 5 bar case. In this latter case, it is interesting to note that the temperature topology is almost identical to the one in the 3 bar case, even though one would expect lower temperatures as a result of the faster expansion. More on that below.

Now turning the attention to condensation, the baseline case exhibits radii smaller than the dimer threshold and therefore nucleation barely takes place. The other two cases, however, do see regions of clusters of 2-4 molecules, at liquid mass factions of roughly 2 % or less.

What is particularly striking is the degree of supersaturation. As was explained in Ch. 5, the saturation ratio in most conventional nozzles exhibiting condensation is typically in the range 6-20. In this case, the rapid expansion and resulting extreme supercooling has driven this ratio up to values in the order of 10^3, with some small regions in the core of the fastest expansion (5 bar case) even narrowly veering into the 10^4 range. The high supersaturation keeps the critical radius value low and results in high nucleation rates. Whereas in conventional nozzles these rates are somewhere in the vicinity of 10^{20}, here they climb to 10^{29}. Physically, this means that if condensation does ensue, the high supersaturation implies it will occur very impulsively, with bursts of enormous numbers of very small clusters, spanning 3-4 water molecules at most, forming in the vapour simultaneously.

This helps explain the aforementioned abnormality in the temperature topology of the 5 bar case. To get a clearer picture of the impact of condensation, this simulation has been ran for a second time, in this instance with the condensation model switched off (i.e., purely gaseous flow). The Mach number and temperature fields between the cases with and without condensation are compared in Fig. 7.1. Apparently, even though the liquid clusters are about as small as they can physically be, the fact that they spontaneously nucleate in such abundance still manages to inflict a sensible effect on the flow. The temperature is raised by more than 20 K near the centerline and the Mach number drops by about 0.2 or more. This also has a macroscopic effect, albeit a small one: the thrust rises by roughly 1.5 %, from 2.95 mN to about 3 mN. Whether this is significant or not is left to the future mission designer to judge. Performance metrics in the nominal condition, meaning with the condensation model active, are listed in Table 7.1. A complete overview of all simulations with and without condensaiton is given in Table 7.5. It can be seen there that the 1 bar case stays virtually unaffected by the condensation, as the small mass fractions that emerge as a result of it are not sufficient for any substantial effect.

The fact that the thrust increases as a result of the condensation is in itself peculiar. It was shown in the validation cases of Sec. 5.9 that the latent heat release causes a pressure rise that should act

Table 7.1: Variation of macroscopic performance with stagnation pressure

Parameter [Unit]	1 bar	3 bar	5 bar
Thrust [mN]	0.503	1.72	2.95
Specific Impulse [s]	97.08	105.22	107.74
Sp. Impulse Efficiency [-]	0.832	0.902	0.924

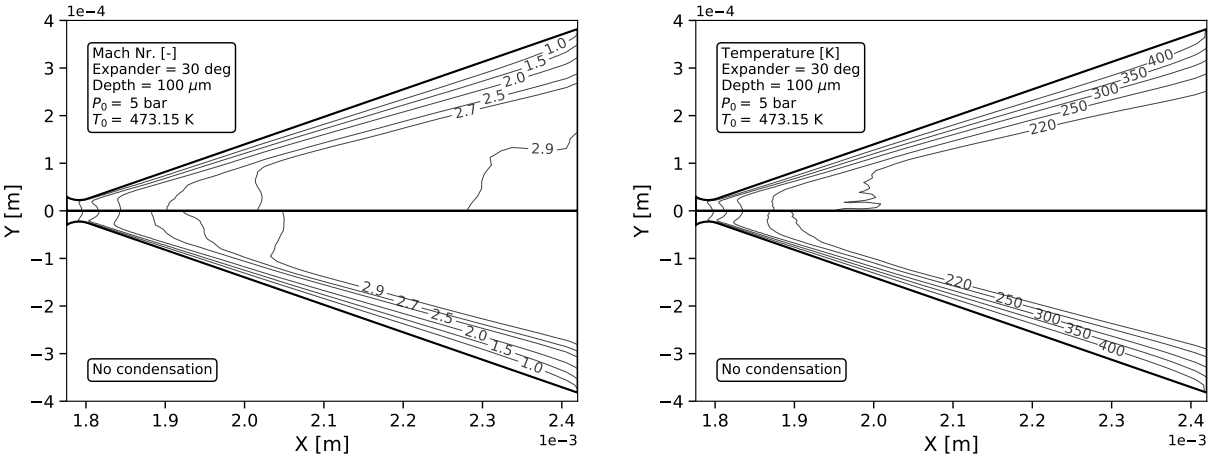

(a) Mach - 5 bar

(b) Temperature - 5 bar

FIGURE 7.1: Comparison of the flowfield for the 5 bar case with (upper half) and without (lower half) the effect of condensation

to slow the expansion. Indeed, in those cases, the velocity exhibited a sharp dip following the onset of condensation, so, if anything, it would be expected here that the thrust should drop. Especially so, given the Mach number is clearly affected here. Why does it not?

The answer can be found by a) revisiting the definitions of the thrust force and Mach number (here, for convenience, in a simplified one-dimensional form for an ideal gas):

$$F_t = \int_A [\rho U_x^2 + (p - p_\infty)] dA$$

$$M = \frac{U_x}{\sqrt{\gamma R T}}$$

b) recalling that the momentum and energy effects of the condensed phase are captured in the following source terms (S_Y being the generation rate of liquid mass per unit volume of vapour):

$$S_U = -U \cdot S_Y \qquad \& \qquad S_h = -h_p \cdot S_Y$$

and c) by taking a closer look at the velocity, rather than the Mach number field (Fig. 7.2):

What is observed is that the velocity field itself is only very subtly slowed down by the condensed phase, staying essentially unchanged. The drop in Mach number noted in Fig. 7.1 came not as a result of a decrease in velocity, but rather due to the increase in temperature following the release of latent heat. The secondary question that arises then is why the condensible has a notable heat energy contribution but not a notable momentum one. This is likely attributable to the fact that as the vapour spontaneously transitions phase after it has been supercooled to the extreme value of almost 200 K, it releases an unusually high amount of latent latent heat per unit mass (refer to Fig. 4.3 in Sec. 4.8.5). At the same time, however, this mass of the condensible itself in absolute value is rather low: Fig. 7.5e indicates mass fractions in the vicinity of 1% relative to the vapour. In such a case, the mass generation

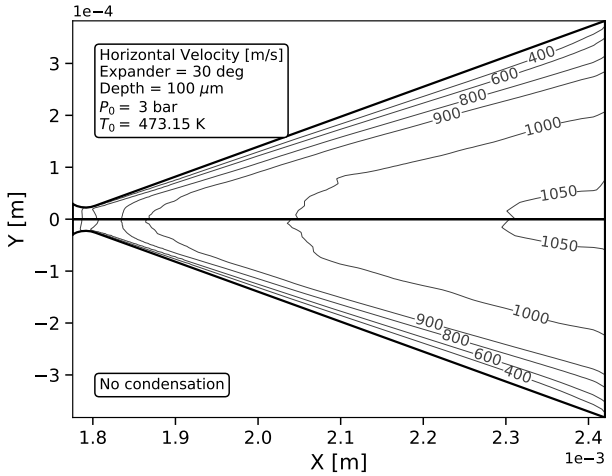

FIGURE 7.2: Horizontal velocity isolines for the 5 bar case with (upper half) and without (lower half) the effect of condensation

rate S_Y stays low, but the high value of h_p still drives the energy source term S_h to high contributions, whereas the momentum source term S_U contributes little to the bulk of the flow. Correspondingly, since the velocity remains largely unperturbed, the effect of the change in momentum on the thrust force is also benign. The majority of the contribution towards the noted 1.5 % thrust increase is then due to the increase in pressure in the expander as a product of the latent heat, which drives upwards the integral $\int_A (p - p_\infty) dA$ at the nozzle exit.

The phenomena discussed above also largely apply to the rest of the results presented in this chapter.

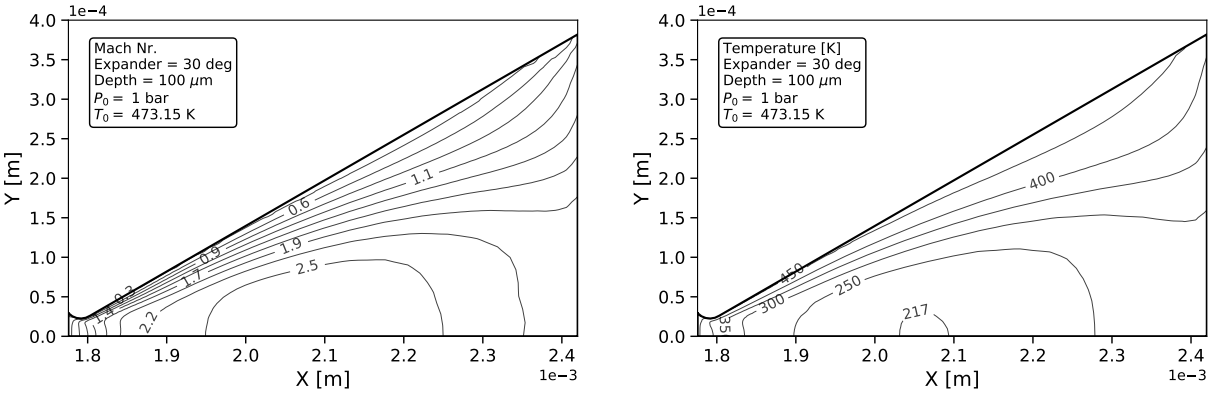

(a) Mach - 1 bar

(b) Temperature - 1 bar

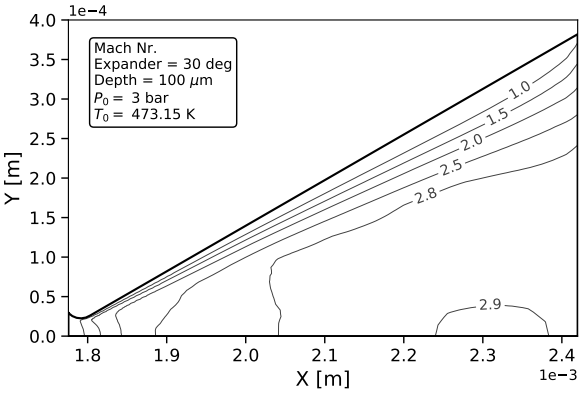

(c) Mach - 3 bar

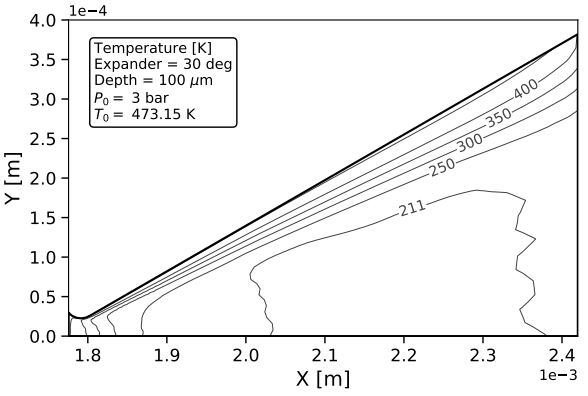

(d) Temperature - 3 bar

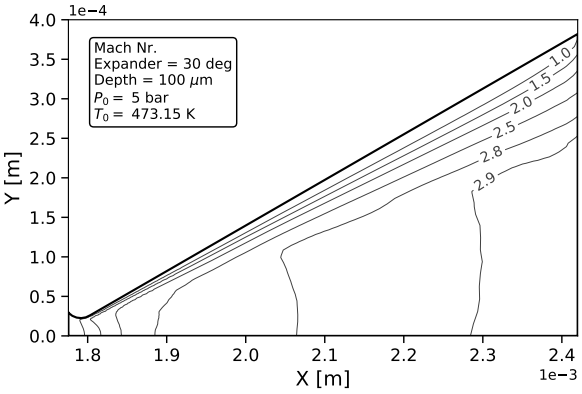

(e) Mach - 5 bar

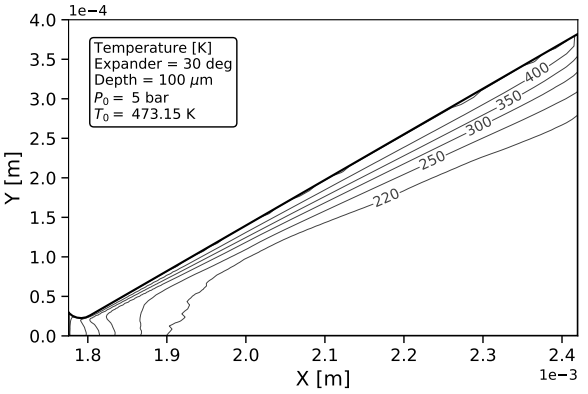

(f) Temperature - 5 bar

FIGURE 7.3: Isolines of Mach number and temperature at pressures of 1-5 bar

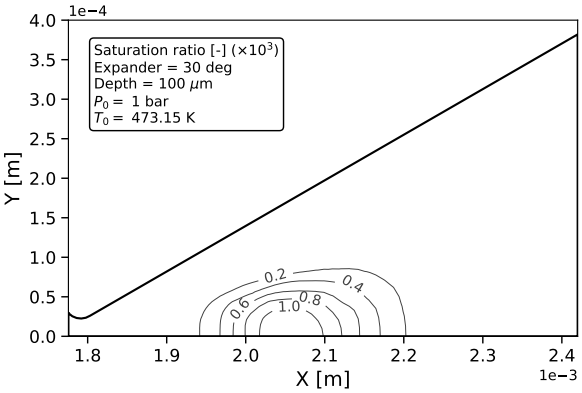

(a) Supersaturation ratio - 1 bar

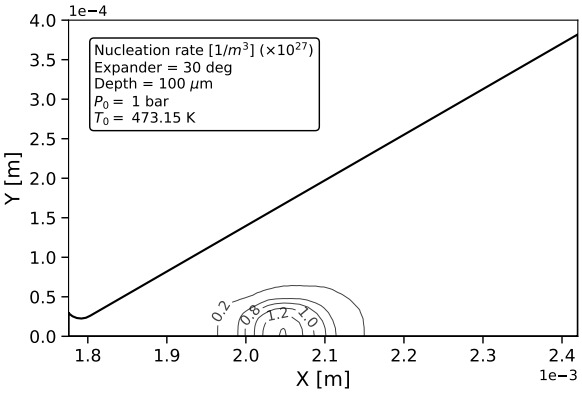

(b) Nucleation rate - 1 bar

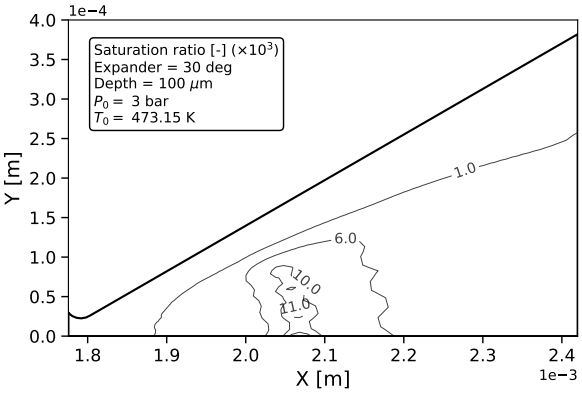

(c) Supersaturation ratio - 3 bar

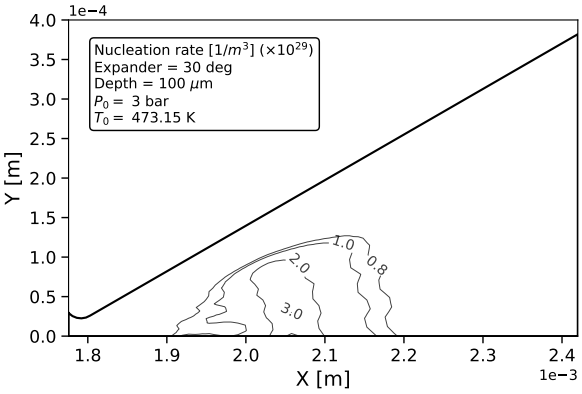

(d) Nucleation rate - 3 bar

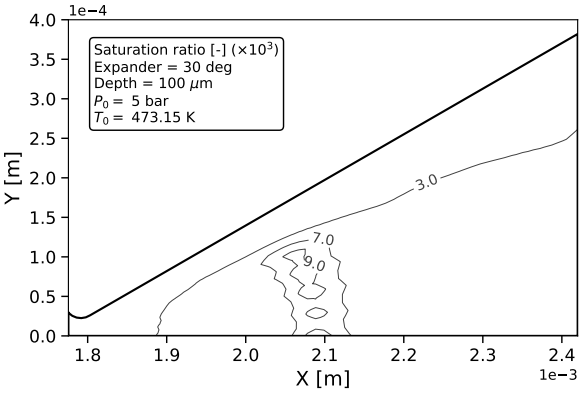

(e) Supersaturation ratio - 5 bar

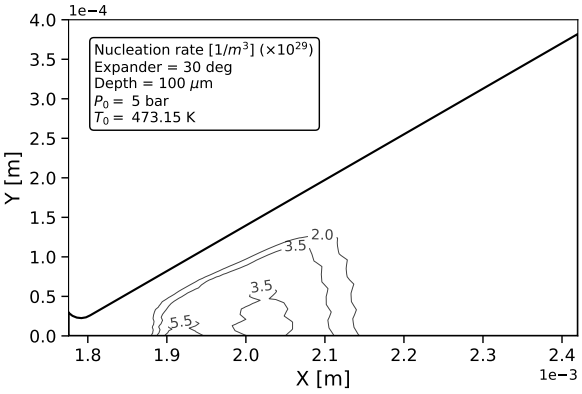

(f) Nucleation rate - 5 bar

FIGURE 7.4: Isolines of supersaturation ratios and nucleation rates at pressures of 1-5 bar

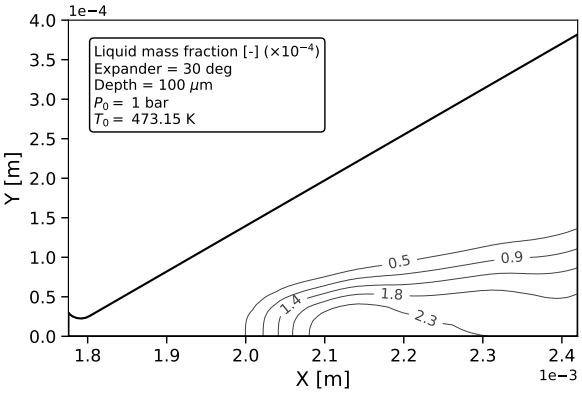

(a) Liquid mass fraction - 1 bar

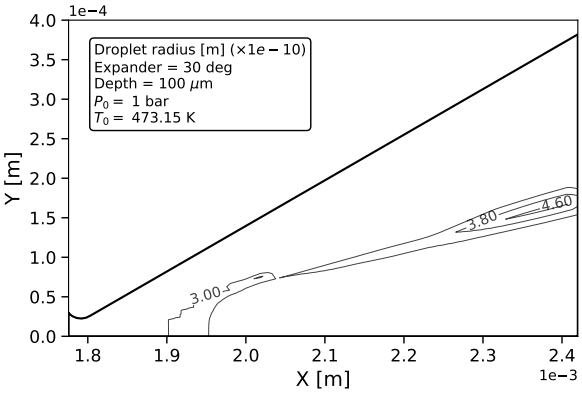

(b) Mean droplet radius - 1 bar

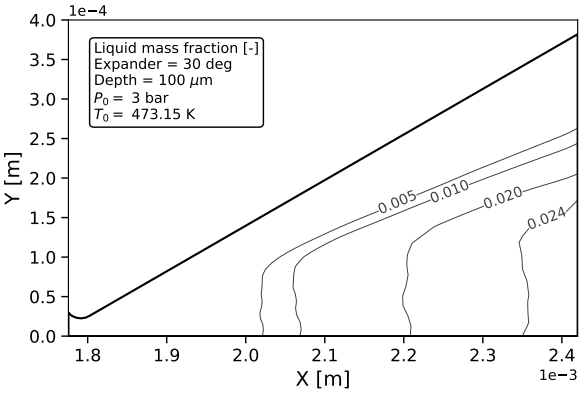

(c) Liquid mass fraction - 3 bar

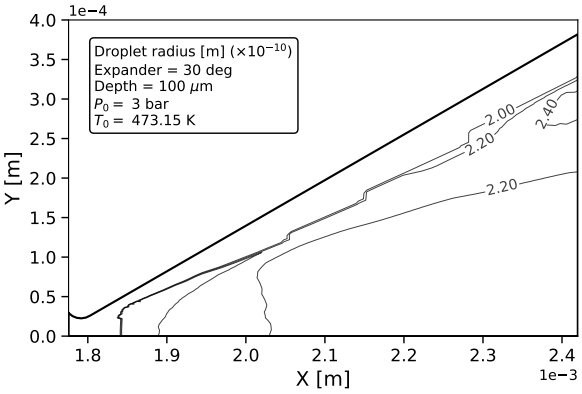

(d) Mean droplet radius - 3 bar

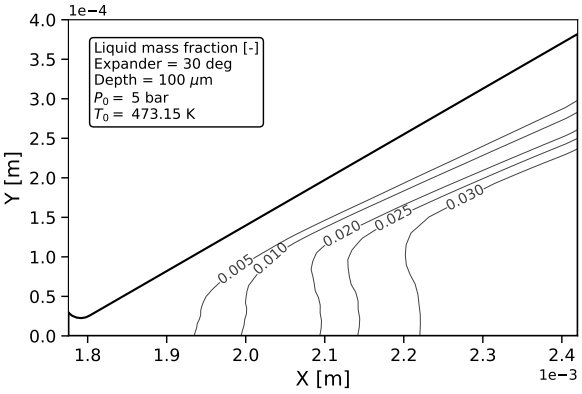

(e) Liquid mass fraction - 5 bar

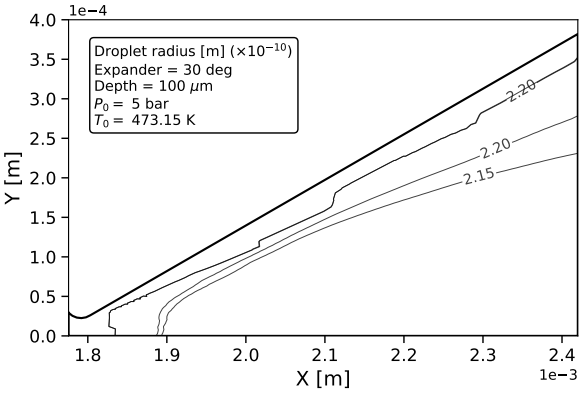

(f) Mean droplet radius - 5 bar

FIGURE 7.5: Isolines of liquid mass fractions and droplet radii at pressures of 1-5 bar

7.2 Effect of stagnation temperature

Examining the influence of varying the stagnation temperature (473, 573, 673 K) is particularly interesting, as it would be expected that raising its value is the most effective approach for avoiding the onset of condensation. The most notable findings emerging from Figs. 7.8 - 7.10 are the following:

- The higher stagnation temperature in the 573 K case obviously leads to a higher temperature in the expander, but that actually appears to encourage the nucleation of clusters at approximately the size of a dimer, relative to the baseline 473 K case (Figs. 7.10b and 7.10d). Even so, the condensation results in very small mass fractions (10^{-5}) and its impact on the flow was found to be practically non-existent. The reason why the mass fractions are so low in this case has to do with the fact that the liquid mass generation rate is dependent on the nucleation rate of new droplets and the interfacial surface area of existing droplets (Eqn. 5.39). The nucleation rate is observably lower in the 573 K case. The droplet surface area follows a simular trend, as there is a smaller number of droplets being generated and no substantial growth follows.
- The 673 K case exhibits no condensation whatsoever (which is why no relevant results are given). Fig. 7.8f shows that only a small portion of the expander flowfield will drop below 300 K (down to roughly 285 K), while the pressure in the same region (not shown in these results) is at roughly 7.5 kPa. Interestingly, examining a typical phase diagram of water (e.g., Fig. 2.4 in Sec. 2.5.2) shows the flow will still become supersaturated and enter what would have normally been the liquid region, even at this high stagnation temperature. The supersaturation ratio, however, is very low ($S \approx 6$), therefore no condensation ensues in the short timeframe the flow spends in the nozzle.

It is interesting that the 573 K case results in the nucleation of physically plausible liquid clusters, whereas the 473K one does not. One would expect that a lower stagnation temperature would encourage condensation. Physically, the cause can eventually be traced to the difference in the degree of supersaturation between the two cases, although there is also a numerical aspect to it. To help illustrate this, it is helpful to make an example calculation.

Recall from Ch. 5 the basic expressions for the critical radius r_c and associated nucleation rate J; the relation between the droplet radius and the liquid mass fraction Y and droplet number N; as well as the fact that N is directly related to J via the source term in its conservation equation and, similarly, Y is related to J, N, r. Briefly, these are listed below.

$$J = q_c \frac{\rho_g^2}{\rho_l} \sqrt{\frac{2\sigma}{\pi m^3}} exp\left(-\frac{4\pi\sigma}{3k_B T_g} r_c^2\right) \quad \& \quad r_c = \frac{2\sigma}{\rho_L R T_g ln(S)}$$

$$N \sim f(J) \quad \& \quad Y \sim f(N, J, r) \quad \& \quad r = \frac{3Y}{4\pi\rho_L N}$$

For the sake of the calculation, we select a typical control volume in the domain along the nozzle centerline in the expander. We wish to focus on the nucleation phenomena, so we assume that the effect of convection in the volume is equilibrated, such that any substantial change in the droplet number and other properties in the cell over time results only due to the condensation. The conservation law for N then reduces to simply $dN/dt = J$. To simplify things, we will also further assume that since the droplet only spends an almost infinitesimally small amount of time in the cell, the effect of droplet growth can be neglected, such that the liquid mass fraction varies only as a function of droplet nucleation. Then, the conservation equation for Y also reduces to simply $dY/dt = \rho_l J \frac{4}{3}\pi r_c^3$. It is also reasonable to assume that, all other factors being equal, a higher stagnation temperature will result in a higher temperature in the expander, at locations featuring the same static pressure for both nozzles.

For the calculation, a static pressure in the control volume of 6 kPa is assumed, a value typical in these nozzles. Consulting Figs. 7.8b and 7.8d, it may also be assumed that the temperatures along the centerline near the nozzle exits are roughly 210 K and 230 K, respectively. For the sake of brevity the detailed calculations are skipped, but using the above relations and the thermodynamics of Ch. 4 one finds for $T = 230\,\text{K}$ a supersaturation ratio $S \approx 443$ and nucleation rate $J \approx 9 \times 10^{26}$ droplets/m^3/s; for $T = 210\,\text{K}$, $S \approx 4900$ and $J \approx 7 \times 10^{29}$ droplets/m^3/s. It can be seen that a difference of just 20 K in that range causes a stark offset in the nucleation rate of three orders of magnitude. While a portion of this is due to the fact that the surface tension differs by about 5% between the two cases, the main driver behind the offset actually turns out to be the variation of saturation pressure with temperature.

Fig. 7.6 depicts the variation of the saturation pressure with temperature for $T \leq 273\,\text{K}$, as given in Ch. 4 by Eqn. 4.51. What can be seen is that the variation is very rapid (essentially exponential) and, at the lower temperature end, an offset of just 20 K is already enough to cause a difference of an order of magnitude (from the order of 1 to the order of 10) to the value of the saturation pressure (and, by extension, to the supersaturation ratio for a given local static pressure).

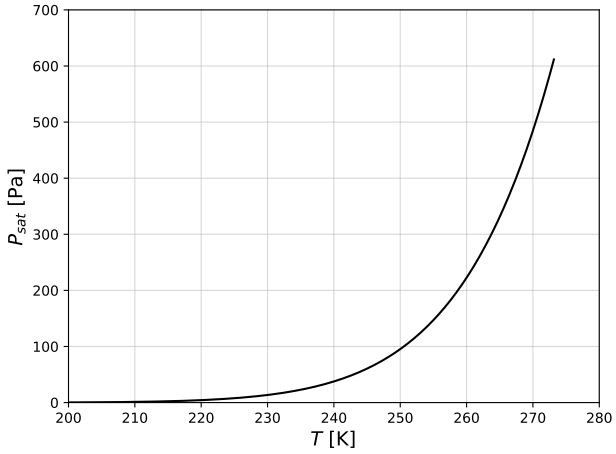

FIGURE 7.6: Variation of the water vapour saturation pressure with the local temperature, for $T \leq 273\,\text{K}$. The saturation curve is given by Eqn. 4.51.

Over a given interval dt, this difference in nucleation rates will yield a corresponding offset in the droplet number N and liquid mass fraction Y between the two cases. Such an offset will also cause the liquid generation rate to be substantially smaller by orders of magnitude for the 573 K, as was mentioned in the beginning of this discussion and and can be observed in Figs. 7.10a and 7.10c. And here is where the numerical artefact stemming from the assumption of a monodisperse droplet distribution comes into effect: we have assumed all droplets have the same size, given by an average radius $r = \left(\frac{3Y}{4\pi\rho_L N}\right)^{1/3}$. Since N and Y scale comparably due to their direct dependence on J, the resulting radii have similar values both for the 473 K and the 573 K cases (in the range of 2-3 $\times\ 10^{-10}$ m), with the latter case featuring a value higher by about 20%. In reality, it is likely the droplets come at an array of sizes and, since the resulting values are very near the minimum physical limit, it may be that a substantially less amount of condensation would actually take place, as a portion of the vapour that now appears to condense would actually not be able to form droplets. Still, as was previously mentioned, the liquid mass fraction for the 573 K is extremely low and its effect on the flow negligible. So, while locally the conditions may marginally encourage the emergence of physically stable droplets despite the increase in temperature, in the global picture a higher stagnation temperature actually helps eliminate the macroscopic impact of condensation.

The main conclusion to be drawn from this example calculation is that the subtle uncertainties involved in the model (in terms of the assumptions made, the thermodynamics, the nucleation physics) can shift the outcome on the occurence or not of condensation in either direction, when the resulting

liquid clusters are so close to the physically meaningful size threshold. That is why also results with radii slightly smaller than 2.75×10^{-10} m have been included in this work.

In view of the above, from a design perspective, it would be desirable for the designer to be able to predict what the minimum stagnation temperature is to avoid condensation in the nozzle altogether, for given nozzle conditions/expected performance. Doing this accurately is rather difficult due to the complex physics, many variables and the uncertainty that are inherently involved in any condensation model, as has perhaps become clear from the discussion above. The development of an analytical model for the prediction of the point of onset of condensation[2] has received widespread attention in condensation literature and still no method has comprehensively achieved this goal, despite the fact that the proposed models are often quite involved. Examples of notable works the reader may refer to are those of Huang and Young (1996) and, more recently, Azzini et al. (2018). A simpler method, which however gives a very conservative estimate, is to employ quasi-1D isentropic flow theory. By utilising the well-known isentropic relations:

$$T_0 = T \cdot \left(1 + \frac{\gamma - 1}{2} M^2\right)$$

$$P_0 = P \cdot \left(1 + \frac{\gamma - 1}{2} M^2\right)^{\frac{\gamma}{\gamma - 1}}$$

and the relation of the saturation temperature as a function of the local pressure given in Sec. 4.5.2 by Eqn. 4.33, it is possible to compute the minimum stagnation temperature required to avoid supersaturation (and, hence, condensation) in the nozzle, for a selected stagnation pressure and nozzle exit Mach number. A plot of this variation for $P_0 = 1$, 3 and 5 bar is shown in Fig. 7.7, for an indicative range of Mach numbers that may be expected at the exit of a supersonic micronozzle. A value of $\gamma = 1.33$ has been used. It can be seen that the required temperature increases with stagnation pressure for a given exit Mach number. It can also be seen that the required temperature is already rather high (≥ 600 K) in the exit Mach number range 2.5-3.5 , a range which is quite common in supersonic (micro)nozzles. It is emphasized again that this estimate is very conservative, perhaps unnecessarily so, for at least the following reasons:

- Quasi-1D isentropic flow theory does not account for the heat input from the planar wall and therefore most likely underpredicts both the flow pressure and temperature at the nozzle exit. So, the calculation may show that the flow may reach saturation when it, in reality, would actually not, which may in turn lead the designer to choose an unnecessarily high stagnation temperature.
- The above methodology aims at eliminating condensation by avoiding supersaturation altogether. But as has become clear by now, the rapid cooling rates allow the flow to dive deeply into the supersaturated region without condensation occuring. Therefore, in reality the design is likely to be able to afford a lower stagnation temperature that gives thermodynamic room to the flow to become supersaturated without (significantly) condensing, as is shown in the 573 K and 673 K cases above.
- The actual average Mach number at the nozzle exit will almost certainly be lower than predicted by ideal rocket theory for a given pressure/temperature ratio, due to the obstruction of the flow by the boundary layers and the heat input from the wall.

Even so, the method is convenient if one is after a rough first estimate. For more elaborate methods, the afore-mentioned cited works and others similar to them are to be consulted. It appears from the results above, however, that for a flowcase as convoluted as the ones in the present micronozzles, the necessity for a detailed numerical simulation and/or experiment may be unavoidable, should the

[2] Often referred to in literature as the "Wilson point", after Charles Thomson Rees Wilson, a Scottish pioneer in water condensation studies.

designer need to be highly confident about whether condensation occurs or not, but at the same time keep the stagnation temperatures as low as possible.

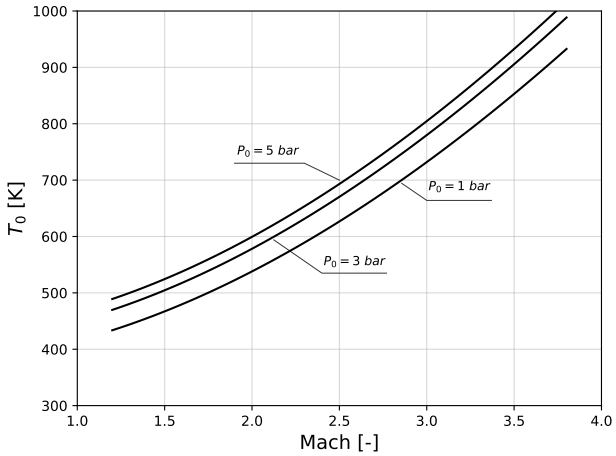

FIGURE 7.7: Variation with exit Mach number of the minimum stagnation temperature required to avoid supersaturation in the nozzle, for selected values of stagnation pressure, according to quasi-1D isentropic theory

It is important to realise that while increasing the stagnation temperature has a favourable effect towards eliminating nucleation, it actually decelerates the flow and has a substantially adverse effect on the macroscopic performance of the nozzle. Comparing the Mach and temperature contours in Fig. 7.8 of the 473 K and 573 K cases shows that, even though in the latter the supersonic core initially accelerates to slightly higher Mach numbers, it eventually decelerates and the temperature increases again by the time the flow has reached the exit. In the 673 K case, the heat flux from the wall is so high that the flow exhibits lower Mach numbers relative to its 473 K counterpart throughout the flowfield. The subsonic layer (delineated by the M = 1 contour) grows thicker and the temperature barely drops below 300 K even in the region of highest expansion. It turns out that the increased heat input from the walls is substantial enough to raise the pressure to a degree that overshadows the effect of the expansion.

The macroscopic impact of these phenomena is given in Table 7.2, in terms of the thrust, specific impulse and specific impulse efficiency. In addition to the above points, it is also interesting to note that the thicker boundary layers resulting from the higher heat flux at the wall are reflected on the specific impulse: while the thrust drops with increasing temperature, the specific impulse increases, because the thickening of the subsonic layers and the generally decelerating flow reduces the mass flux at the nozzle exit. Even so, the fact remains that globally the performance deteriorates, as is shown by the decreasing impulse efficiency.

Table 7.2: Variation of macroscopic performance with stagnation temperature

Parameter [Unit]	473 K	573 K	673 K
Thrust [mN]	1.72	1.67	1.62
Specific Impulse [s]	105.22	114.28	122.16
Sp. Impulse Efficiency [-]	0.902	0.890	0.878

These findings are consistent with those of Louisos and Hitt (2012), who performed an extensive investigation of the effects of heat transfer on 3D micronozzle flows and found that the thrust consistently scales at inverse proportion with the wall temperature. In this regard, it is interesting to make a comparison with ideal rocket theory predictions. If it is assumed that the static temperature varies only slightly from the stagnation value T_0 at the inlet of a quasi-1D, isentropic, chocked nozzle flow of

an ideal gas, then the exhaust velocity and mass flow can be related to the temperature as (Sutton and Biblarz, 2017):

$$U_e = \sqrt{\frac{2\gamma}{\gamma - 1} R T_0 \left[1 - \left(\frac{p_e}{p_i} \right)^{(\gamma-1)/\gamma} \right]}$$

$$\dot{m} = \frac{p_0 A_t}{\sqrt{R T_0}} \cdot \sqrt{\gamma \cdot \left(\frac{1+\gamma}{2} \right)^{\frac{1+\gamma}{1-\gamma}}}$$

where A_t is the nozzle throat area and $\frac{p_e}{p_i}$ is the ratio of static pressures at the exit (e) and inlet (i). The expression shows that increasing the stagnation temperature has no practical effect on the thrust force $F_T = \dot{m} U_e$, as the mass flow scales in inverse proportion to $\sqrt{T_0}$ while the velocity in direct proportion to it. This is in contrast with the results here. The reason, of course, is that the high surface-to-volume ratio of the micronozzle and the elevated wall temperatures render this flowcase neither inviscid nor adiabatic and serves to illustrate why the classical ideal rocket theory is of limited relevance in inferring performance trends for this type of systems.

In summary, it is shown that while the raising the flow temperature has a generally beneficial effect in eliminating nucleation, it comes at a notable expense in performance. What has become apparent in the analysis so far is that the baseline case of a 30 deg expander and 3 bar stagnation pressure is not impacted by condensation phenomena at a stagnation temperature of 473 K. In view of this, it would be advisable that, unless other system requirements demand it, the stagnation temperature is kept at that value or some value near it.

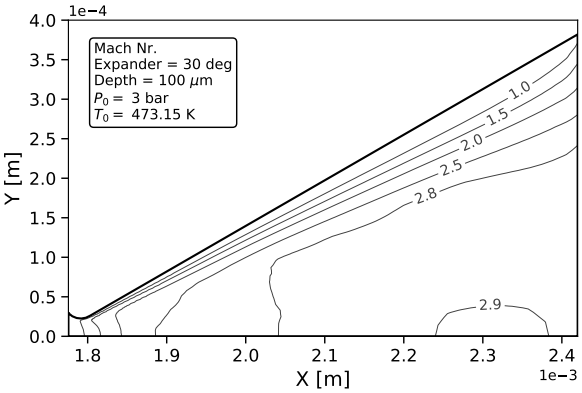

(a) Mach - 473 K

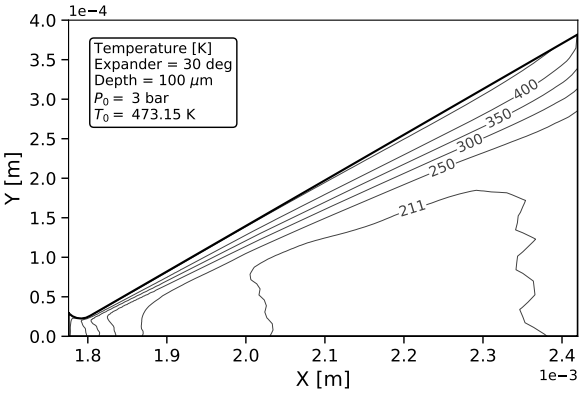

(b) Temperature - 473 K

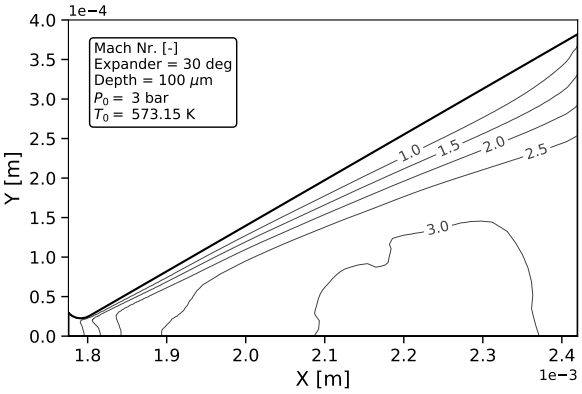

(c) Mach - 573 K

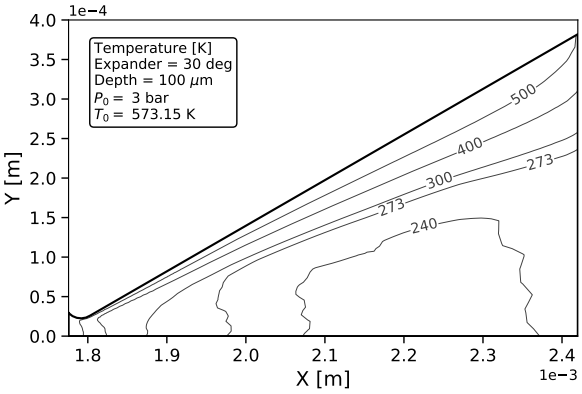

(d) Temperature - 573 K

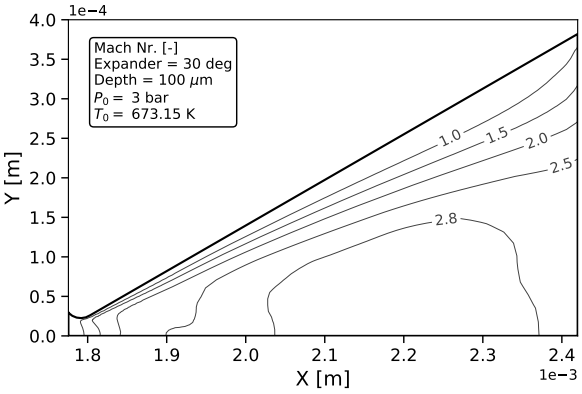

(e) Mach - 673 K

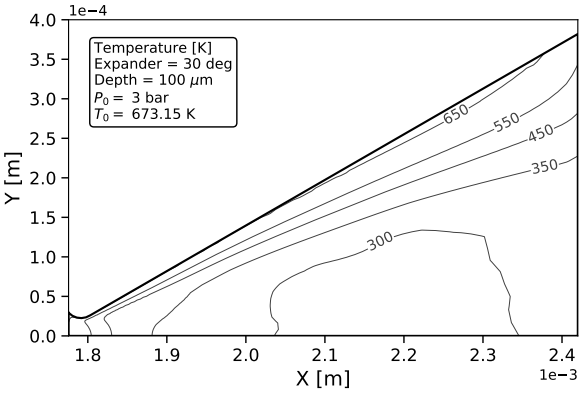

(f) Temperature - 673 K

FIGURE 7.8: Isolines of Mach number and temperature at stagnation temperatures of 473-673 K

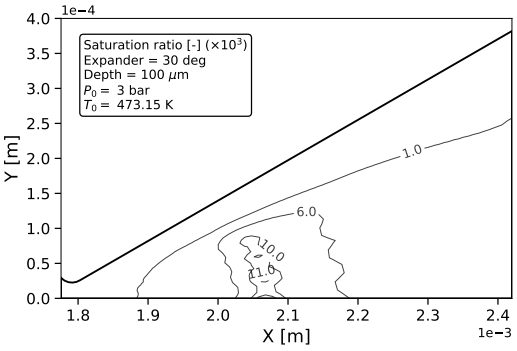

(a) Supersaturation ratio - 473 K

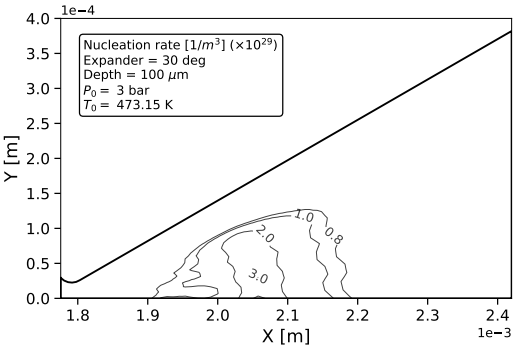

(b) Nucleation rate - 473 K

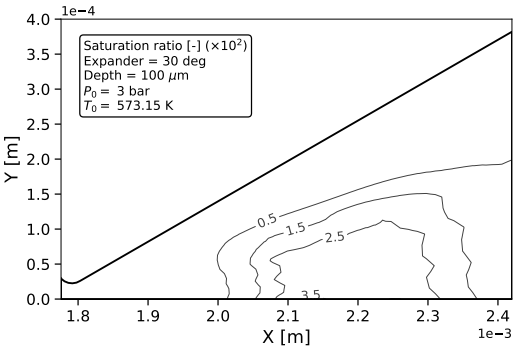

(c) Supersaturation ratio - 573 K

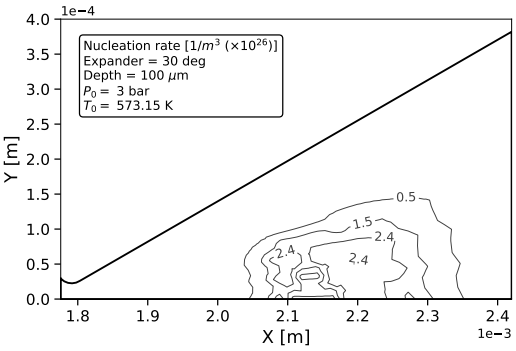

(d) Nucleation rate - 573 K

FIGURE 7.9: Isolines of supersaturation ratios and nucleation rates at stagnation temperatures of 473-673 K

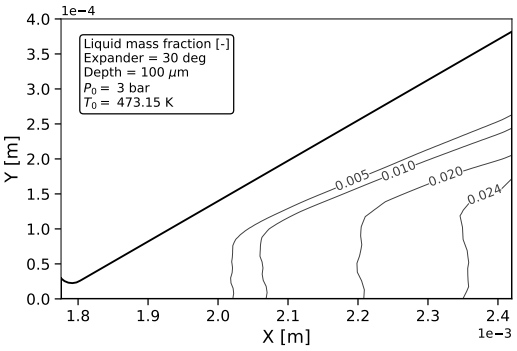

(a) Liquid mass fraction - 473 K

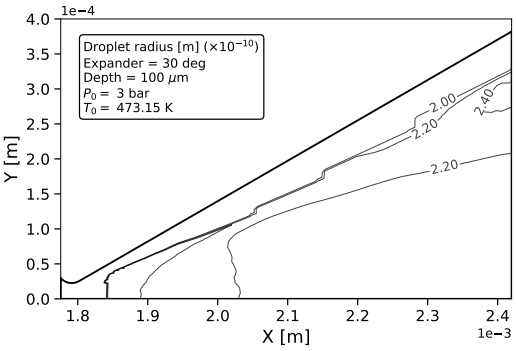

(b) Mean droplet radius - 473 K

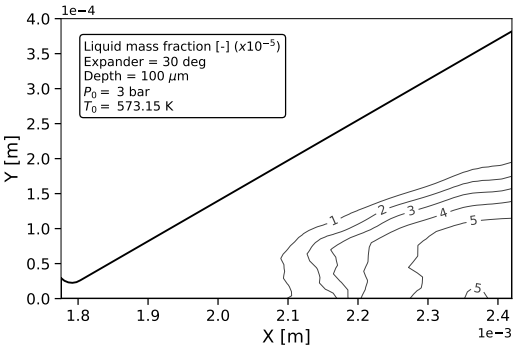

(c) Liquid mass fraction - 573 K

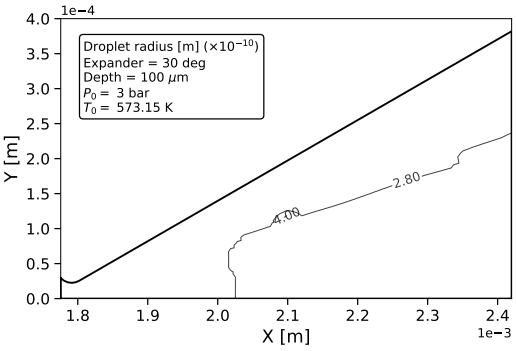

(d) Mean droplet radius - 573 K

FIGURE 7.10: Isolines of liquid mass fractions and droplet radii at stagnation temperatures of 473-673 K

7.3 Effect of expander angle

The expander angle is varied between 15, 30 and 45 degrees to assess what influence the expansion rate has on the results. Similarly to previous cases, contours for Mach number and temperature, saturation rate and nucleation, liquid fraction and droplet radius are given in Figs. 7.11 - 7.13.

It is can be seen that the expansion rate has a competing influence with the temperature effects from the wall that were described in the previous section. The 15 deg case exhibits the lesser expansion of the three, but also has the longest expander section. As a result, not only is the Mach number lower but also the heat flow from the wall is given more time to manifest in the flow. It is observed in Figs. 7.11a and 7.11b that already roughly half-way through the 15 deg conical section, the expansion is essentially halted and the Mach number and temperature drops by about 25 % by the nozzle exit. It is reasonable to assume that in this particular case, the pressure rise due to heat input in the flow is further augmented by the fact that some small degree of condensation takes place, with clusters in the size of a dimer or a trimer appearing at mass fraction in the vicinity of 1%.

Expectedly, as the angle is increased, these effects are alleviated. However, they are not eliminated. Even in the 45 deg angle case, it can be seen in Figs. 7.11e and 7.11f that the flow does not accelerate unhindered until the nozzle exit and the region of the highest Mach number is quickly slowed down to lower values.

The increased expansion rate that results from increasing the expander angle drives the flow further into non-equilibrium before any nucleation starts. This is evident in Figs. 7.12b, 7.12d and 7.12f, where progressively larger supersaturation ratios are recorded with increasing angle. As expected, this also induces higher nucleation rates. Even so, the resulting mass fractions are not large, no more than roughly 3 % and the droplet radii remain small, at the vicinity of the smallest physical size or below it. This indicates that, similarly to the baseline case, nucleation will either not occur or, if it does, it will have a mostly negligible impact. In the case of the 45 deg expansion, for instance, which exhibits the most intense nucleation and largest droplet sizes, it was found that the thrust rises from roughly 1.67 mN to 1.7mN (between the droplet-free and nominal case), a difference of about 1.2%. In the 15 deg case, the same difference is less than 0.2%. The mechanisms behind this are the same as described in Sec. 7.1.

Some indicative performance estimates are given in Table 7.3, for the reader's reference. It is notable that the nozzle with the 30deg expander seems to be an optimum between the three cases, with all three performance metrics being at a maximum in that setting. This is in agreement with past observations in literature (Louisos et al., 2008) and reflects the fact that that angle seems to strike a balance between avoiding excessive interference from the boundary layers at the wall, but also keeping expansion losses due to the opening angle contained. For the tabulated results, recall that the theoretical specific impulse is computed according to quasi-1D theory, which is not concerned with expander angles (when the expansion ratio stays unchanged), hence its value is the same for all three nozzles (at roughly 116.63 s).

Table 7.3: Variation of macroscopic performance with expander angle

Parameter/Angle [Unit]	15 deg	30 deg K	45 deg
Thrust [mN]	1.65	1.72	1.62
Specific Impulse [s]	101	105.22	122.16
Sp. Impulse Efficiency [-]	0.866	0.902	0.878

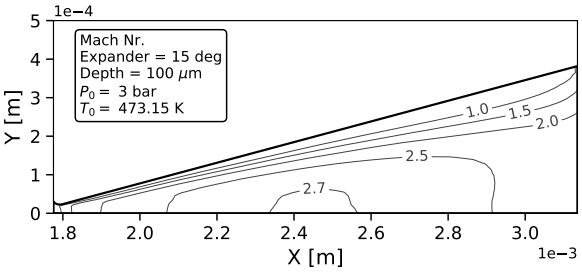

(a) Mach - 15 deg

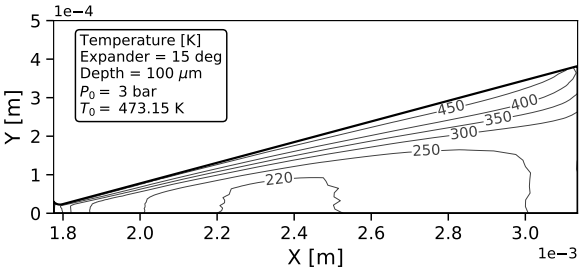

(b) Temperature - 15 deg

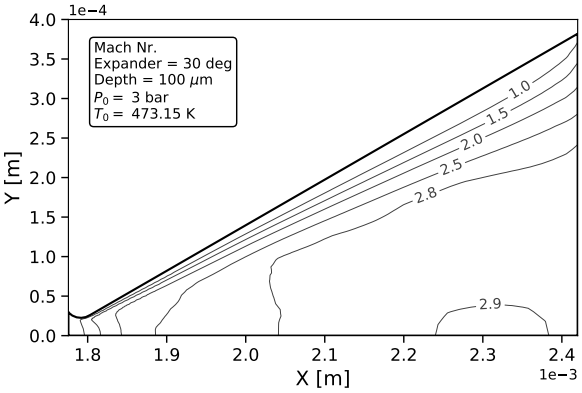

(c) Mach - 30 deg

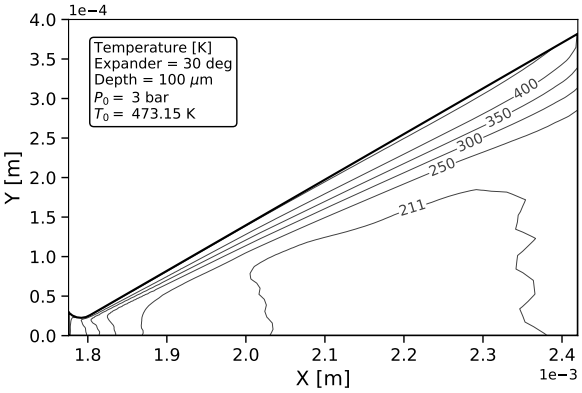

(d) Temperature - 30 deg

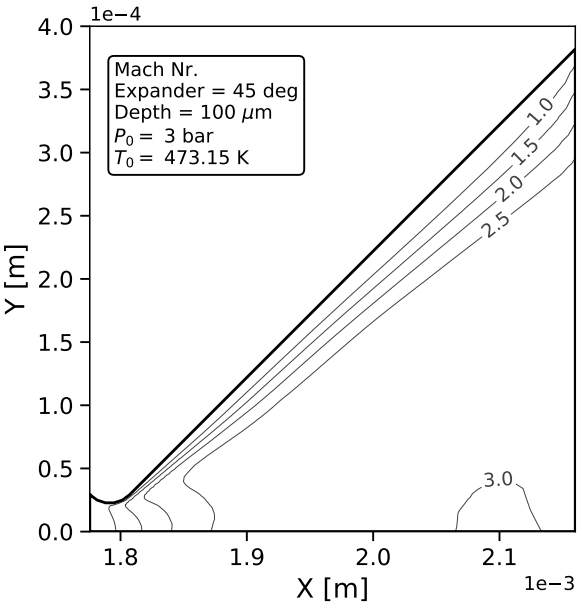

(e) Mach - 45 deg

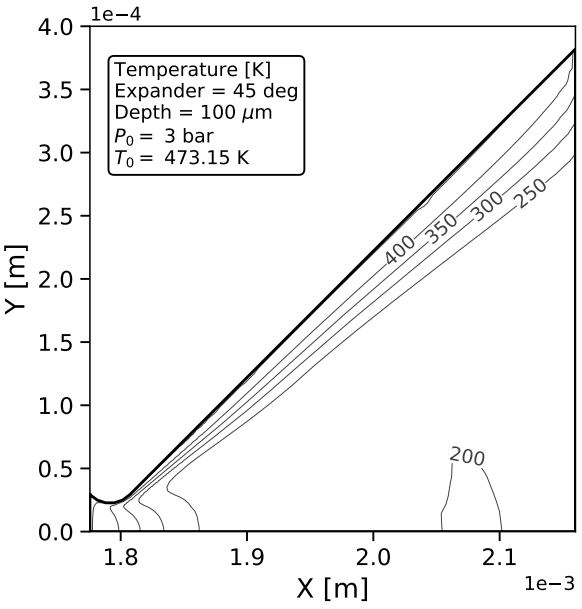

(f) Temperature - 45 deg

FIGURE 7.11: Isolines of Mach number and temperature at expander angles of 15-45 deg

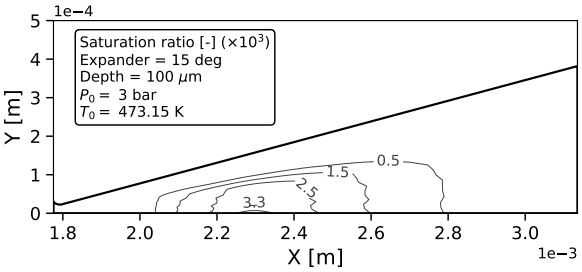

(a) Supersaturation ratio - 15 deg

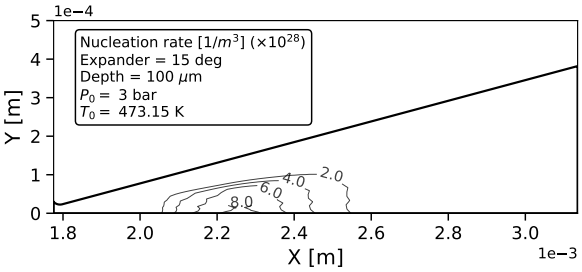

(b) Nucleation rate - 15 deg

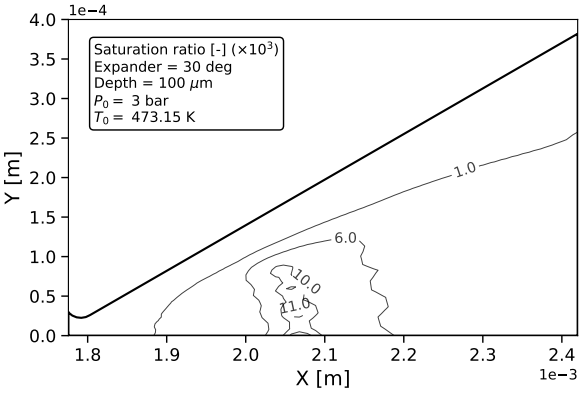

(c) Supersaturation ratio - 30 deg

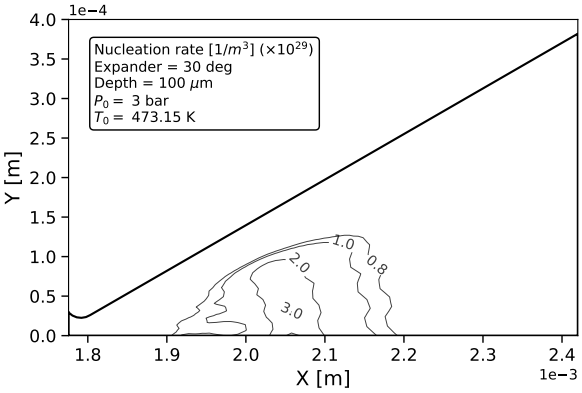

(d) Nucleation rate - 30 deg

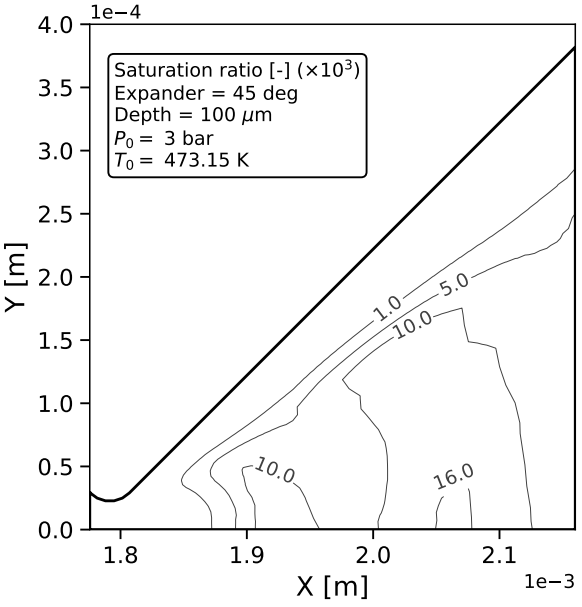

(e) Supersaturation ratio - 45 deg

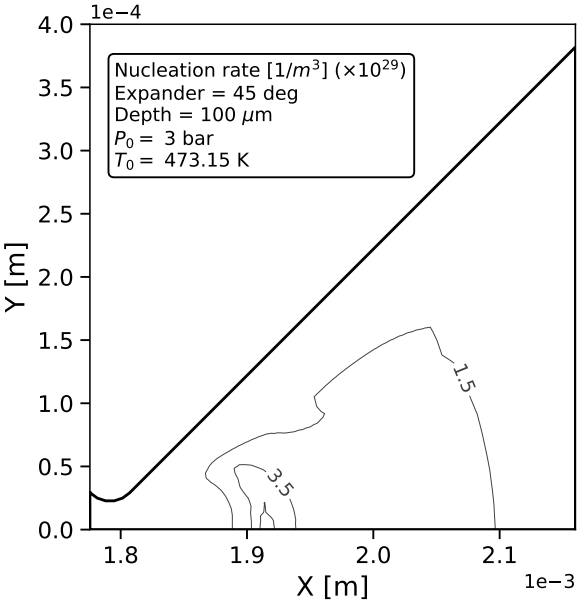

(f) Nucleation rate - 45 deg

FIGURE 7.12: Isolines of supersaturation ratios and nucleation rates at expander angles of 15-45 deg

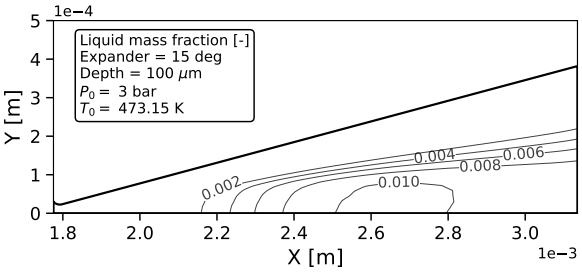

(a) Liquid mass fraction - 15 deg

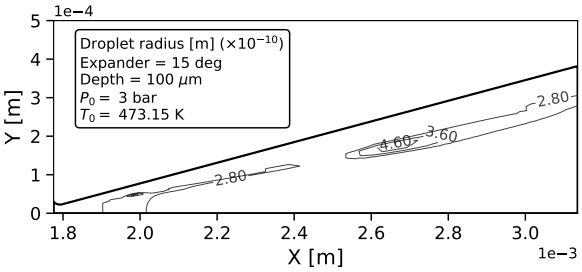

(b) Mean droplet radius - 15 deg

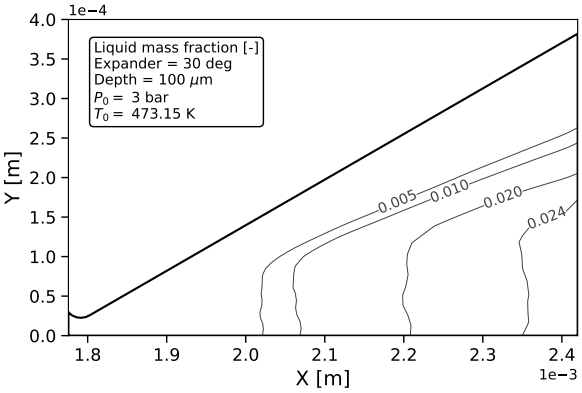

(c) Liquid mass fraction - 30 deg

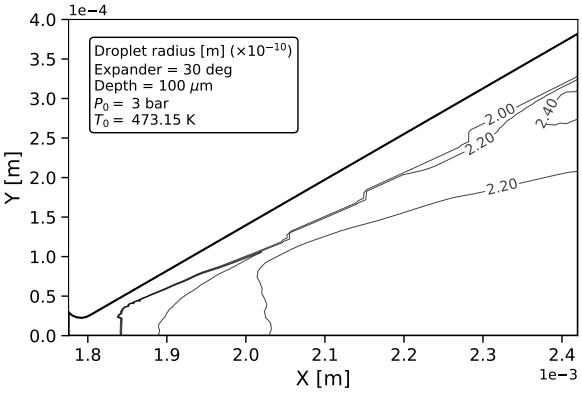

(d) Mean droplet radius - 30 deg

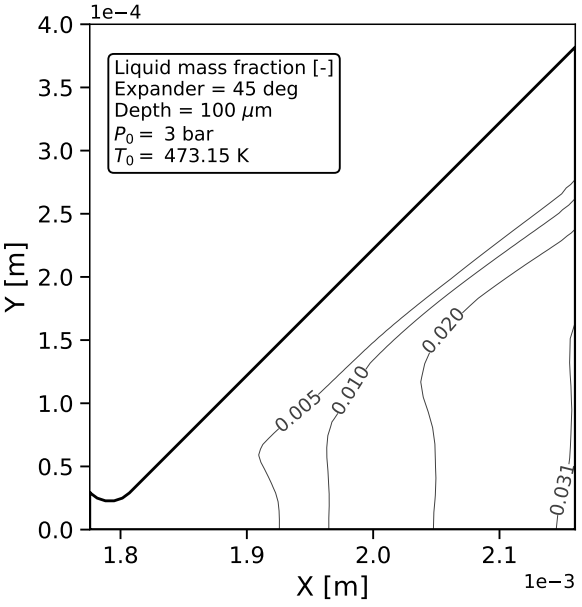

(e) Liquid mass fraction - 45 deg

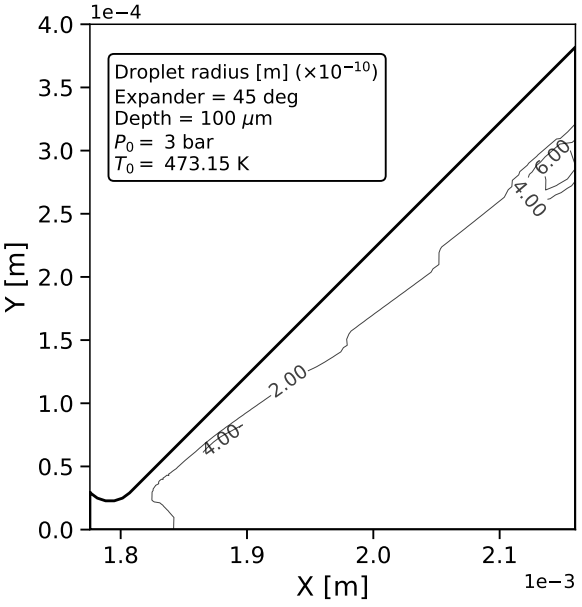

(f) Mean droplet radius - 45 deg

FIGURE 7.13: Isolines of liquid mass fractions and droplet radii at expander angles of 15-45 deg

7.4 Effect of nozzle depth

Sec. 7.2 clearly demonstrated that the stagnation temperature has a dominant effect on the flow, primarily as it is assumed the wall is fixed at that temperature. It was shown it has a conflicting effect, in the context of this work, where - if raised sufficiently high - it can be helpful in effectively eliminating the prospect of any condensation, but simultaneously degrading the micronozzle's performance. One may then reasonably wonder what happens if the contribution from the planar wall is reduced. This is the purpose of this last results-oriented section in this work, where the nozzle depth is doubled to 200 µm and the influence of that is assessed.

The results are presented in Figs. 7.14 - 7.15. It becomes readily clear that the planar wall has a most decisive effect on the internal flowfield. As the depth is increased, the core of the flow is distanced from the wall's thermal boundary layer and a larger portion of it can expand undisturbed. Unlike the results shown so far, the core of the flow attains a maximum Mach number and temperature and persists at those values until the nozzle exit, virtually unperturbed by the heat influences noted in the previous cases. However, it also becomes clear that despite the reduced thermal effects and the extra volume available for the expansion to develop, the core Mach number is actually substantially lower than in the 100 µm case, by more than 10%. Similarly, the temperature of the core is several tens of degrees higher, with the majority of the expander staying above 273 K, as opposed to previous cases where it was near 200 K. These observations hint at a substantial presence of condensation.

Indeed, Figs. 7.15c and 7.15d show that vapour molecules collapse to liquid water en mass, with mass fractions in excess of 20% and radii substantially larger than in previous cases, almost in the order of 10^{-9} m. It must be noted, the liquid mass fraction is so high that it in fact exceeds the validity range of this model. Recall it was assumed in Ch. 5 that the liquid mass fraction does not exceed 0.1, such that interactions between the droplets and their effect on the flow can be ignored. Even so, these results are still explored, as they provide a good indication of how a decreased wall influence gives room for condensation to significantly impact the nozzle flow.

A comparison between the flow with condensation and the hypotherical one without, given in Table 7.4, is instructive in pointing out the effects. Both parameters exhibit notable behaviours. In this case, the thrust is lower than in the droplet-free case, which is in constrast to the trends observed in the comparisons of the previous sections. On the contrary, the specific impulse is lower in the droplet-free case.

Table 7.4: Comparison of the macroscopic performance between the condensed and condensation-free flow cases for the 200 µm-deep micronozzle ($P_0 = 3$ bar, $T_0 = 473$ K, Expander angle = 30 deg)

Parameter [Unit]	Two-phase	Gaseous	Offset
Thrust [mN]	3.45	3.65	-5%
Specific Impulse [s]	115.68	110	+5%

To address these particularities, we take a more detailed look at the flow topology. Fig. 7.16 presents contours of pressure, temperature, velocity and Mach number on the plane of the nozzle exit. The properties have been plotted on 1/4th of the exit plane and can be extended to the full geometry by symmetry. The left hand side of each plot shows the properties for a simulation with the condensation model switched off (a hypothetical situation of purely gaseous steam, for comparison purposes only) and the right side depicts the nominal case. Some interesting observations can be made.

The pressure is distinctly higher (by roughly 500Pa in the regions shown) in the condensation case, as expected due to the release of latent heat. The temperature exhibits less uniform behaviour. Near the core of the flow, where also the condensation mainly takes place, there is a very sharp difference

in temperature: the condensation case stays entirely above 270 K, while the droplet-free case plummets to lower than 160 K. This serves to indicate just how much heat a condensation at such mass fractions may release. Away from the core and close to the walls, however, the temperatures of the two cases converge to similar values, with the condensation case being hotter only by a few degrees. It appears that the thermal energy released is mostly expedited at heating the extremely cold vapour in the immediate vicinity of the droplets. Its effect is less apparent near the walls, where the flow is already elevated to a very high temperature via the wall's much larger heat input and is therefore not particularly influenced by the incoming heat. It should also be understood that since the flow near the walls is moving at a much lower velocity, the mass flux is also lower. The majority of the gaseous mass is being convected by the supersonic core (which is also colder) and it is there where most of the heat generated is consumed.

A result that is somewhat puzzling is the velocity's response to the condensation. Rather than dropping as would be expected following the temperature increase, the velocity in the condensation case is actually slightly higher, by a few metres per second, than its droplet free counterpart. The velocities converge to practically equal values in the directions of the walls. This behaviour is in contrast both with how supersonic flows are generally known to respond to heat addition (Louisos and Hitt, 2012) and with the observations made in Sec. 5.9, which are typical of supersonic nozzle condensation. To understand the reasons behind these discrepancies it is helpful to look at the internal flow topology from yet one more perspective.

Fig. 7.17 portrays the evolution of the pressure, temperature, density and velocity along the nozzle centerline, from the nozzle throat to the nozzle exit, for both the condensed and droplet-free case. There are a few things to unpack here. The first observation confirms what is also shown in Figs. 7.15c and 7.15d, namely that the condensation initiates almost immediately downstream of the nozzle exit. It can be seen that the pressure starts rising at that location and deviates from the droplet free case until the nozzle exit. Stark is the difference between the tempereratures of the two cases, as was also earlier observed at the nozzle outlets. The behaviour of the velocity curves is particularly interesting, since it shows that initially the velocity in the condensed case responds as expected: i.e., it experiences a dip and a local decrease in slope (a sign of deceleration) as a result of the heat release and the subsequent pressure rise. A short distance downstream, however, it continues accelerating and in fact overtakes the velocity of the droplet-free case, eventually resulting in the higher exit velocity that was observed earlier. One last notable observation is that the condensation-free case experiences a local pressure and temperature increase, a bump, roughly half-way through the expander, which results in a respective dip in the velocity: a local deceleration. A similar behaviour is noted in the condensed case, albeit to a much lesser extent.

The combination of the above observations indicates that when condensation does substantially occur in the flow, it enters a complex interaction mechanism with the viscous and heat transfer effects that anyway characterise a micronozzle's flowfield. The local dip in velocity in the droplet-free case is frequently observed in studies of the internal flow topology in micronozzles with hot walls (Alexeenko et al., 2006; Moríñigo and Hermida-Quesada, 2009). It is the result of the fact that the boundary layers that have been rapidly building along the wall downstream of the throat are locally impeding the flow, before the effect of the expansion becomes dominant enough to overcome their influence and encourage the flow to keep accelerating. When condensation occurs, the sharp increase in pressure originating from the central core of the flow serves to slightly suppress the boundary layers at the wall. This is also clear in Fig. 7.16a, where it can be seen that the sonic boundary is thinner along the walls for the condensed case. So, even though at the onset of condensation the flow does temporarily slow down, eventually the suppressed boundary layers allow more room for it to expand and also subtract less momentum due to viscous effects. The condensed case goes on to expand at a faster rate than its droplet-free counterpart and the velocity attains a higher value until the exit.

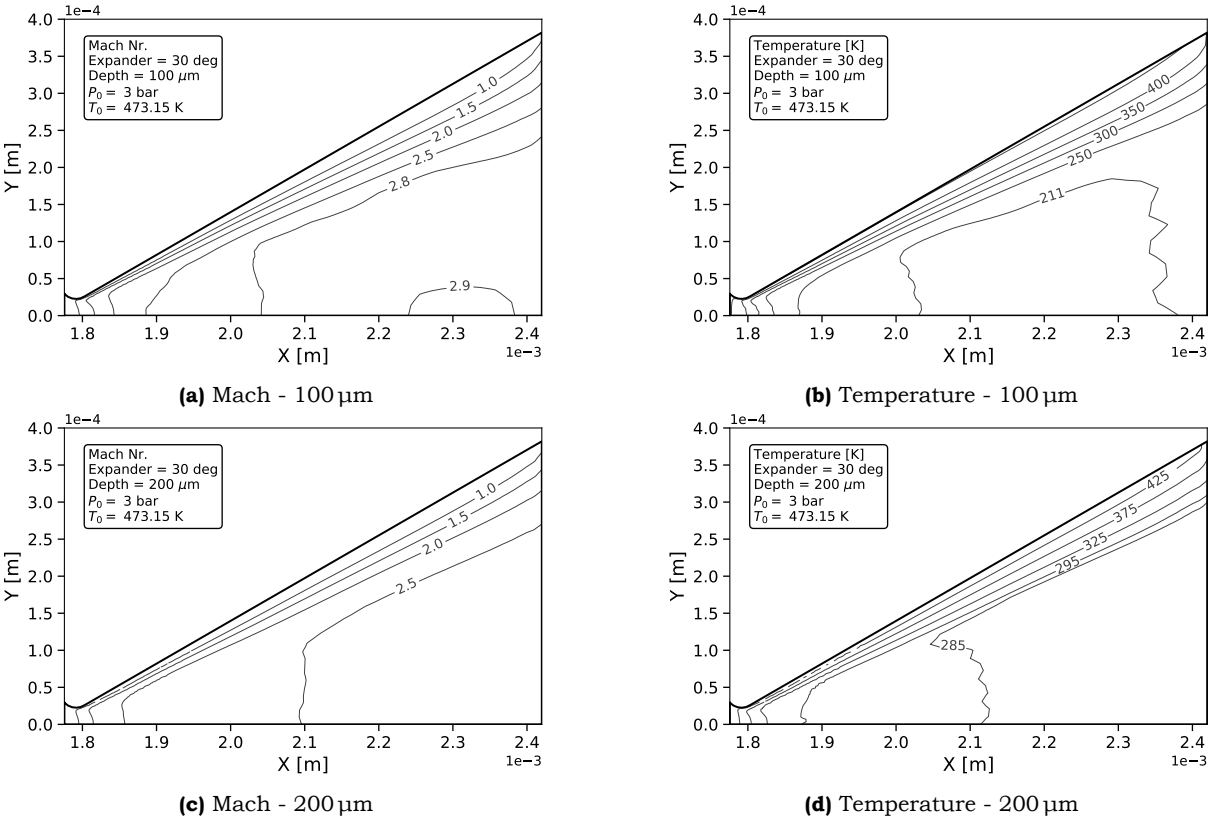

(a) Mach - 100 µm

(b) Temperature - 100 µm

(c) Mach - 200 µm

(d) Temperature - 200 µm

FIGURE 7.14: Isolines of liquid mass fractions and droplet radii at nozzle depths of 100-200 µm

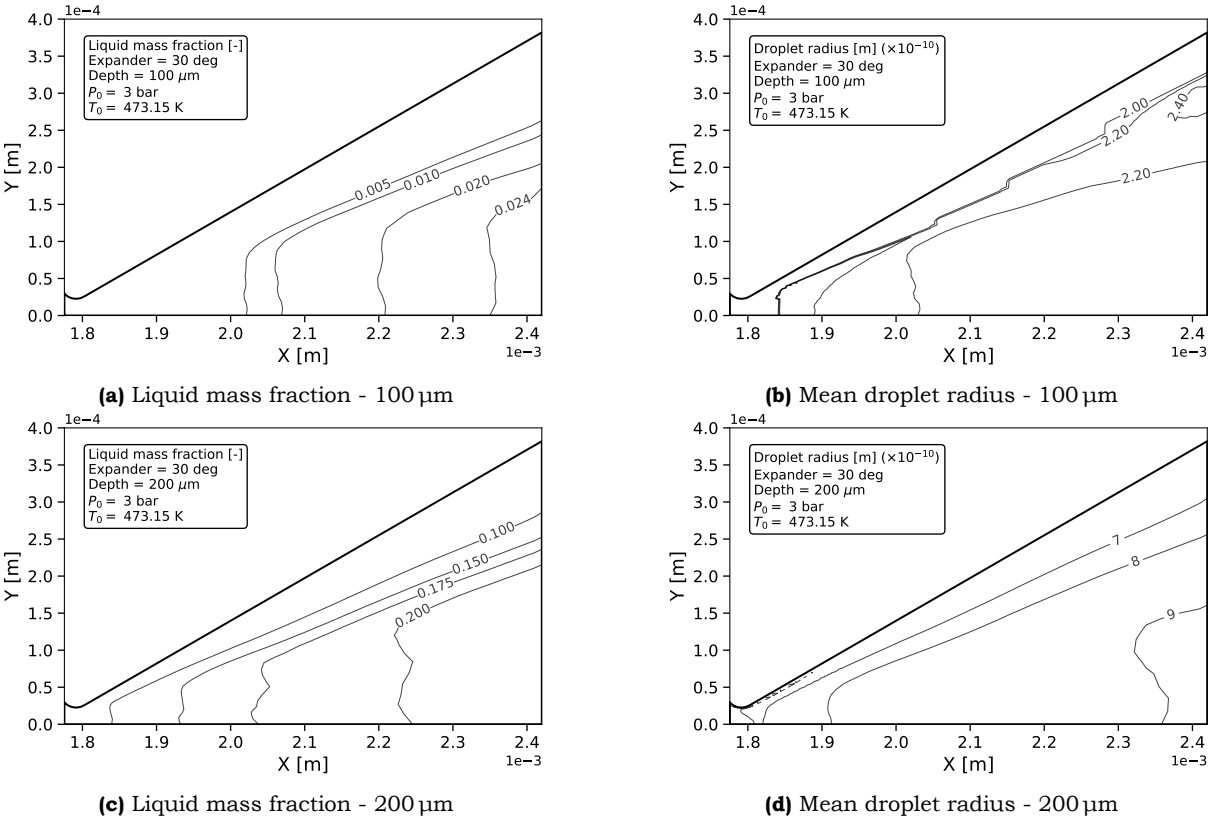

(a) Liquid mass fraction - 100 µm

(b) Mean droplet radius - 100 µm

(c) Liquid mass fraction - 200 µm

(d) Mean droplet radius - 200 µm

FIGURE 7.15: Isolines of liquid mass fractions and droplet radii at nozzle depths of 100-200 µm

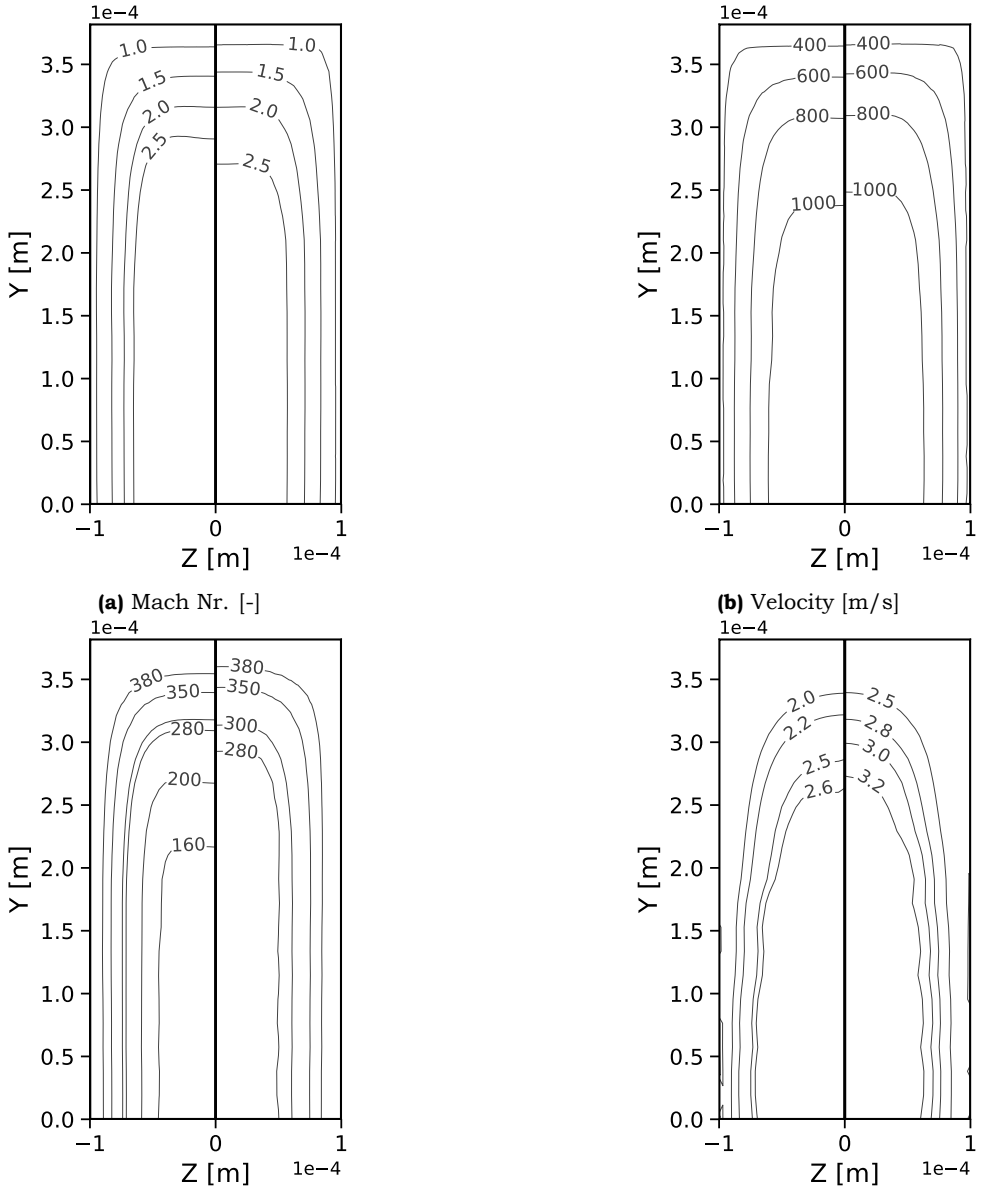

(a) Mach Nr. [-]

(b) Velocity [m/s]

(c) Temperature [K]

(d) Pressure [Pa] (x 1000)

FIGURE 7.16: Comparison of a selection of properties between the cases with and without condensation along the nozzle exit cross-section of the 200 µm-deep micronozzle ($P_0 = 3$ bar, $T_0 = 473$ K, Expander angle = 30 deg). By symmetry, only a quarter of the exit cross section is shown. In each instance, the droplet free case is on the left half and the case with condensation on the right half.

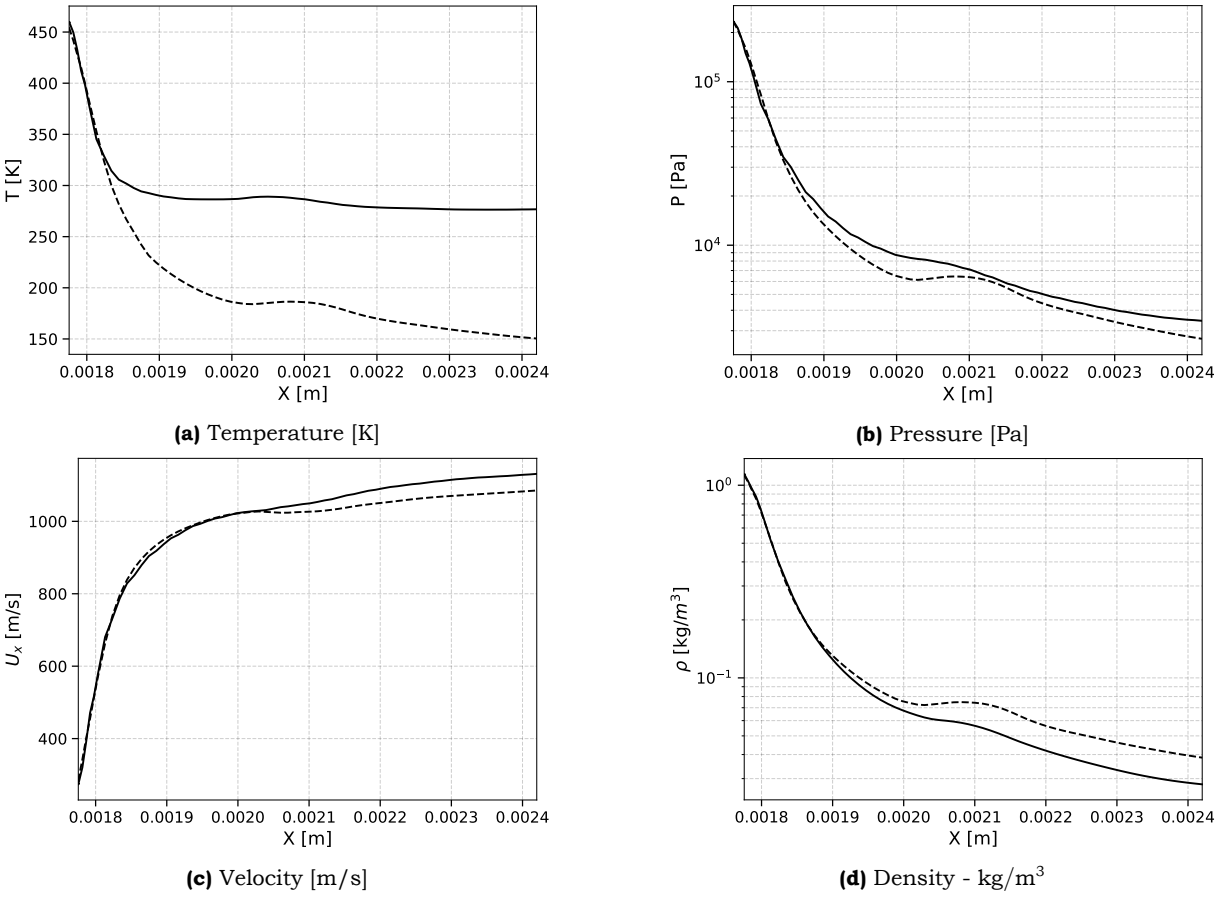

(a) Temperature [K]

(b) Pressure [Pa]

(c) Velocity [m/s]

(d) Density - kg/m^3

FIGURE 7.17: Flow properties for the 200 µm-deep nozzle along the centerline, from the throat to the exit. The dotted lines correspond to prely gaseous flow, for comparison.

As a last remark the 200 µm nozzle has a specific impulse efficiency of 0.99, as opposed to roughly 0.9 of the 100 µm case. This is an expected result, as 1) the extra depth provides a better approximation to the quasi-1D assumption and partially alleviates viscous losses and 2) the energy released by condensation provides an increment in acceleration by the mechanism described above. Of course, this is not predicted by ideal rocket theory, which is why the efficiency has almost reached unity.

7.5 Summary of macroscopic performance

The macroscopic performance values for the micronozzle cases examined in this work are summarised in Table 7.5, for the reader's reference. The table is divided into a left and a right half, with the condensation model's results listed on the left and the purely gaseous case presented on the right, for comparison. The baseline case is re-introduced in every subcategory of the table, to visually aid comparison between the cases.

Table 7.5: Overview of the macroscopic performance metrics for the micronozzle cases examined in this work

	Two-phase model			**Single-phase model**		
	F_T [mN]	**I_{sp} [s]**	**$n_{I_{sp}}$ [-]**	**F_T [mN]**	**I_{sp} [s]**	**$n_{I_{sp}}$ [-]**
Baseline						
$P_0 = 3$ bar, $T_0 = 473$ K, $\theta_{exp} = 30$ deg, $depth = 100$ µm	1.72	105.22	0.902	1.72	105.09	0.901
Stagnation pressure						
1 bar	0.503	97.08	0.832	0.507	97.07	0.832
3 bar	1.72	105.22	0.902	1.72	105.09	0.901
5 bar	2.95	107.74	0.924	2.99	107.1	0.918
Stagnation temperature						
473 K	1.72	105.22	0.902	1.72	105.09	0.901
573 K	1.67	114.28	0.890	1.67	114.28	0.890
673 K	1.62	122.16	0.878	1.62	122.16	0.878
Expander angle						
15 deg	1.65	101.00	0.866	1.646	101.6	0.871
30 deg	1.72	105.22	0.902	1.72	105.09	0.901
45 deg	1.69	104.40	0.895	1.708	104.17	0.893
Nozzle depth						
100 µm	1.72	105.22	0.902	1.72	105.09	0.901
200 µm	3.45	115.68	0.992	3.65	110.0	0.943

Part V

Conclusions and Recommendations

CHAPTER 8

Conclusions

This work set out on the objective to implement a numerical model that would be used to examine whether the phenomenon of metastable condensation - common in supersonic nozzles operating on superheated steam - is a probable occurence during the operation of the water-fed, micropropulsion-oriented nozzles developed at TU Delft for microsatellite applications. The model was compiled in three sequential steps: an existing compressible solver was supplemented with slip conditions to capture the mild degrees of rarefaction in the supersonically expanding flow; a thermodynamic model for the real-gas behaviour was assembled; and a model for the determination of the generation of new clusters was then built upon the compressible solver. The likelihood and impact of condensation was then examined for selected nozzle geometries featuring expander angles of 15-45 deg, depths of 100-200 μm and stagnation pressures and temperatures of 1-5 bar and 473-673 K respectively.

The main conclusion to be drawn is that condensation is in fact a likely scenario, especially as the nozzle depth is increased. It is, however, not necessarily a consequential one: it was shown that in most instances the effect on macroscopic performance is either negligible or no more than roughly 2%. The only exception has been the deeper micronozzle, which indeed saw a deterioration in performance of 5% or more. In a more general sense, one further concludes that assessing the impact of condensation on this type of nozzles is not as straightforward as in their large-scale counterparts and it is difficult to note consistent trends. If it does occur, the phenomenon will enter a complex interaction mechanism with the heat supplied from the walls, the viscous layers developing on these walls and the degree to which the expansion can overcome either or both. While in conventional scale nozzles the occurence of the phenomenon typically guarantees a reduction in thrust and efficiency, here there is no consistent trend and the nature of the influence depends on the extent to which the release of latent heat can match in severity the rest of the phenomena inside the micronozzles.

It is now possible to address the research questions that were postulated at the start of this work.

RQ1: Does condensation ensue within the operational envelope of the micronozzles of interest?

It was shown the condensation process is typically divided into a nucleation phase, during which droplets first spontaneously emerge out of the vapour and a subsequent growth phase. The results indicate that nucleation is a likely phenomenon in nearly all instances when the stagnation temperature is at 473 K, even when the depth is relatively shallow (100 μm). However, the droplets are afforded only a miniscule amount of time to grow before they exit the nozzle, hence the phase of growth is not significant and the droplets often stay (approximately) at the size at which they nucleated. The situation is different when the nozzle depth is increased. The nucleation then takes place so far upstream in the nozzle (almost at the throat), that the droplets grow nearly an order of magnitude by the time they exit the nozzle, which also results in substantially more latent heat being released. So, condensation does often ensue, but is largely limited to the nucleation phase.

RQ2: How is the potential onset of condensation affected by the stagnation conditions (pressure and temperature) in the nozzle?

In the case of the stagnation pressure, it has been noted that changing the value from the baseline 3 bar in either direction will act to encourage nucleation, albeit in different ways. A lower total pressure

will decrease the inertia of the flow in the expander, leading to higher pressures there, which establish a favourable pressure/temperature combination for the onset of nucleation. Instead, increasing the total pressure results in faster expansion and higher supersaturation, which may result in larger mass factions condensing to liquid. In both instances, however, the macroscopic effect was small, in the vicinity of 1% or less.

Raising the stagnation temperature to 300 °C or more generally serves to eliminate condensation altogether. However, the resulting heat flux into the flow tends to have an adverse effect on the micronozzle's performance, decreasing both its thrust output and its specific impulse efficiency. So, one has to trade off whether any gains from the elimination of the small amounts of nucleation are worth the losses resulting from increasing the temperature.

In any case, it should be understood that the occurence of condensation is not simply a function of either the pressure or the temperature separately, but of both at the same time. Therefore, its occurence will depend on the particular combination of the two conditions that results in the nozzle expander.

RQ3: How is the potential onset of condensation affected by the nozzles' geometry in terms of their expander opening angle and their depth?

For both geometric parameters, their use as a means to control the onset of condensation is in conflict with improvements in the nozzle condensation-free performance. It was found that increasing the expander angle helps reduce the likelihood of nucleation, but results in higher expansion losses for the velocity. Similarly, the results implied that it is suggested to keep the nozzle as shallow as possible to prevent extensive condensation by exploiting the high wall temperatures, but that will in turn result in significant viscous losses. Generally, a geometry with a 30-deg expander and a 100 μm depth appears to provide the best compromise between the various effects.

RQ4: If condensation does ensue, does it have a substantial impact on the nozzles' macroscopic performance (thrust and specific impulse)? And if so, what is that impact?

In most instances, the effect is negligible or rather small, within less than 2% in thrust, specific impulse and specific impulse efficiency. An exception was the deeper 200 μm nozzle, that exhibited changes of at least 5%, an estimate that is likely to be worse in reality, as effects that have been neglected turned out to play a role in this case (high mass factions mean the droplet inertial effects and cross-droplet interactions must be accounted for). The nature of the impact seems not to be consistent and instead depends on the severity of the condensation occurence. It was found that in instances where only limited condensation occurs (mass fractions of 1-2% or less), a small increment is added to the thrust, as a result of the fact that the momentum is relatively unaffected but the pressure rises at the nozzle exit. Inversely, in the deeper nozzle that saw extensive condensation, the thrust dropped markedly. The specific impulse followed the opposite trends, for similar reasons.

RQS: Eventually, should the prospect of condensation be a design consideration in the future? If so, what design choices are recommended?

Whether the impact of condensation is substantial or not will depend on the eventual mission implementation of the thruster and the answer to this research question is likely to differ depending on the requirements of a given mission. The effect on performance usually did not exceed 1-2%. If the mission's operational requirements are insensitive to this level of variation in performance, this needs not be a concern. This changes if the nozzle geometries are less shallow, as it was shown that increasing the depth can induce severe phase change.

For instance, a CubeSat or PicoSat that has a generic mission goal, such as the technology demonstration of onboard systems, is unlikely to be concerned with a 1% increment in thrust. However, for a satellite carrying an optical payload or similar technology with a positioning and/or pointing requirement, a 1-2% change integrated over the impulse of a thrusting maneouvre could accummulate to a

substantial offset and could be a matter of concern.

Regarding a suggested design choice, it has actually turned out to be difficult to provide consistent guidelines, as the measures that would be advisable for eliminating condensation often affect other aspects of the nozzle's performance negatively. From the perspective of the nozzle geometry, it appears that a 30-deg expander angle strikes a good balance in simultaneously containing interference from the wall boundary layers and expansion losses, while offering some room for selecting stagnation conditions suitable for the mission at hand without the impact of condensation being very significant. The nozzle depth should be kept as shallow as possible, but this should be traded off against viscous losses. Concerning the stagnation conditions, it was found that the stagnation temperature should ideally be as high as possible, but this has to be traded off against losses from thermal interferences, as well as performance considerations such as the desired specific impulse. A recommendation will not be made here for the stagnation pressure, as this is a primary driver behind the thruster's system performance as a whole and therefore is almost fully mission dependent.

CHAPTER 9

Recommendations for future work

The numerical investigations performed in this work and the ensuing results point at directions that future work could take. In a numerical work that has involved so many different aspects and assumptions, there are a lot of things one could recommend exploring further. However, rather than focusing on such details, here 6 main recommendations are given on general aspects that the author feels must be addressed in the near future for a complete characterisation of the micronozzles' performance.

Recommendation 1: Eventually, experimental work is needed to assess or disprove the assumptions made in this work and their effect on the validity of the results. Among the many simplifications made here, the two most consequential ones were likely to assume that the wall follows the stagnation temperature and that the ambient pressure is at 30 Pa. Will the flight-certified nozzle eventually be made by silicon or will a different material affect the rate of heat conduction? Is it really that the cooler gas has no time to affect the temperature of the wall? Could the thermal state of the nozzle in space, prior to operation (for instance, exposed to the sun or not), affect how quickly the heater elevates the wall temperature and alter the heat input to the flow?

Similar points can be made in the case of the ambient pressure. In the spectrum of deep vacuum pressures, a value of 30 Pa is rather high. If the steam expands against real vacuum, then the expansion rate is even faster and the nozzle flow will more closely approximate that of a free-jet expansion. The water vapour will be driven even deeper into non-equilibrium and the expander temperatures will likely be even lower. Does condensation still occur, then? Or is it that now the expansion is far too fast for anything substantial to take place?

These and other questions can only be conclusively answered experimentally.

Recommendation 2: The results of this work pertaining to the influence of the wall temperature could perhaps be a matter of concern. Ongoing experimental work in the TU Delft micropropulsion group currently seems to be pursuing progressively higher stagnation temperatures for the thruster. But it has been shown here and in past works that (if the assumption of the wall staying close to the stagnation value is correct) this actually has a distinctly negative impact on the nozzle's performance (in terms of thrust). Possibly in tandem with the previous point, future work should focus on a more detailed examination of the wall's thermal response to the activation of the heating element and the impact on the performance should be evaluated accordingly.

Recommendation 3: The present work only addressed the steady state portion of the thruster's operation. It is certainly interesting, perhaps even necessary, to show what happens during the transient phases as well. There have been works in literature (e.g., by Louisos and Hitt (2011b)) that have demonstrated the micronozzle flow behaviour can be drastically different during the start-up and shutdown, when the Reynolds numbers are low and the heat transients prevalent. It would be useful to have an impression on whether this works (un)favourably for the phase transition of the superheated steam.

Recommendation 4: The results of the present work imply that although condensation/freezing may not take place inside the nozzle itself, it will most likely take place in the immediate vicinity of its exit.

The products, droplets or fragments of ice, could be harmful to nearby surfaces (solar panels, optics, electronics, etc) and this is likely to be an important systems engineering consideration. So, perhaps it is warranted that future work focuses on the analysis of the nozzle's exhaust plume and its potential for contaminating sensitive spacecraft components.

Recommendation 5: Hybrid NS-DSMC simulations: Virtually every numerical examination of micronozzle performance in literature follows the same pattern: either a Navier-Stokes model is used at the expense of accuracy because insufficient computational resources are available for the more realistic stochastic approaches; or, if a particle-based tool is used, only a very limited range of cases are examined, due precisely to its computational costs. Perhaps it is time for the department to start looking into the prospect of a hybrid solver that would merge the two approaches or any other like them and make use of the best of both worlds. A decade or two ago, the development of such tools may have seemed like an insurmountably complex and uncertain task. Nowdays, however, there is a substantial amount of literature and past work that can facilitate the effective and timely execution of this task. Such a numerical tool would allow the micropropulsion group to run accurate estimations of performance at virtually any operational condition. It would also provide the possibility to verge beyond the limits of the nozzle geometry itself and assess such effects as the diffusion of its plume, interaction with nearby surfaces, etc. Perhaps the effort would be worth it in the near future, possibly as part of a PhD project or similar.

Having delineated possible future outlooks via the recommendations above, this work has reached its end.

Bibliography

Abraham, O. (1981). Gasdynamics of very small laval nozzles. *Physics of Fluids*, 24(6):1017. DOI: 10.1063/1.863493.

Alexeenko, A. A., Fedosov, D. A., Gimelshein, S. F., Levin, D. A., and Collins, R. J. (2006). Transient heat transfer and gas flow in a MEMS-based thruster. *Journal of Microelectromechanical Systems*, 15(1):181–194. DOI: 10.1109/JMEMS.2005.859203.

Amann-Winkel, K., Böhmer, R., Fujara, F., Gainaru, C., Geil, B., and Loerting, T. (2016). Colloquium: Water's controversial glass transitions. *Reviews of Modern Physics*, 88(1). DOI: 10.1103/revmodphys.88.011002.

Arkilic, E. B., Breuer, K. S., and Schmidt, M. A. (2001). Mass flow and tangential momentum accommodation in silicon micromachined channels. *Journal of Fluid Mechanics*, 437:29–43. DOI: 10.1017/s0022112001004128.

Arlemark, E., Markelov, G., and Nedea, S. (2012). Rebuilding of Rothe's nozzle measurements with OpenFOAM software. *Journal of Physics: Conference Series*, 362:012040. DOI: 10.1088/1742-6596/362/1/012040.

Azzini, L., Pini, M., and Colonna, P. (2018). Semi-analytical model for the prediction of the wilson point for homogeneously condensing steam flows. *International Journal of Heat and Fluid Flow*, 70:1–14. DOI: 10.1016/j.ijheatfluidflow.2018.01.004.

Bakhtar, F. and Piran, M. (1979). Thermodynamic properties of supercooled steam. *International Journal of Heat and Fluid Flow*, 1(2):53–62. DOI: 10.1016/0142-727x(79)90011-0.

Bakhtar, F., Young, J. B., White, A. J., and Simpson, D. A. (2005). Classical nucleation theory and its application to condensing steam flow calculations. *Proceedings of the Institution of Mechanical Engineers, Part C: Journal of Mechanical Engineering Science*, 219(12):1315–1333. DOI: 10.1243/095440605x8379.

Barber, R. W. and Emerson, D. R. (2006). Challenges in modeling gas-phase flow in microchannels: From slip to transition. *Heat Transfer Engineering*, 27(4):3–12. DOI: 10.1080/01457630500522271.

Barschdorff, D., Dunning, W. J., Wegener, P. P., and Wu, B. J. C. (1972). Homogeneous nucleation in steam nozzle condensation. *Nature Physical Science*, 240(103):166–167. DOI: 10.1038/physci240166a0.

Bayt, R. L. (1999). *Analysis, Fabrication and Testing of a MEMS-based Micropropulsion System*. PhD thesis, Aerospace Computational Design Laboratory, Dept. of Aeronautics & Astronautics, Massachusetts Institute of Technology.

Bayt, R. L. and Breuer, K. S. (2000). Fabrication and testing of micron-sized cold-gas thrusters. In *Micropropulsion for Small Spacecraft*, pages 381–397. American Institute of Aeronautics and Astronautics.

Bertolotti, F. P. (1998). The influence of rotational and vibrational energy relaxation on boundary-layer stability. *Journal of Fluid Mechanics*, 372:93–118. DOI: 10.1017/s0022112098002353.

Bhattacharya, S., Lutfurakhmanov, A., Hoey, J. M., Swenson, O. F., Mahmud, Z., and Akhatov, I. S. (2013). Aerosol flow through a converging-diverging micro-nozzle. *Nonlinear Engineering - Modeling and Application*, 2(3-4):103–112. DOI: 0.1515/nleng-2013-0020.

Bird, G. A. (1994). *Molecular Gas Dynamics and the Direct Simulation of Gas Flows*. Oxford University Press Inc, New York, USA, 1st edition. ISBN: 0-19-856195-4.

Blondel, F. (2014). *Couplages instationnaires de la vapeur humide dans les écoulements de turbines à vapeur (in French)*. PhD thesis, Ecole Centrale de Lyon.

Bobbert, C., Schütte, S., Steinbach, C., and Buck, U. (2002). Fragmentation and reliable size distributions of large ammonia and water clusters. *The European Physical Journal D*, 19(2):183–192. DOI: 10.1140/epjd/e20020070.

Bondarev, A. E. and Kuvshinnikov, A. E. (2018). Analysis of the accuracy of OpenFOAM solvers for the problem of supersonic flow around a cone. In *Lecture Notes in Computer Science*, pages 221–230. Springer International Publishing.

Cen, J. W. and Xu, J. L. (2010). Performance evaluation and flow visualization of a MEMS based vaporizing liquid micro-thruster. *Acta Astronautica*, 67(3-4):468–482. DOI: 10.1016/j.actaastro.2010.04.009.

Cervone, A., Mancas, A., and Zandbergen, B. (2015). Conceptual design of a low-pressure micro-resistojet based on a sublimating solid propellant. *Acta Astronautica*, 108:30–39. DOI: 10.1016/j.actaastro.2014.12.003.

Cervone, A., Zandbergen, B., Guerrieri, D. C., De Athayde Costa de Silva, M., Krusharev, I., and van Zeijl, H. (2017). Green micro-resistojet research at delft university of technology: new options for cubesat propulsion. *CEAS Space Journal*, 9(1):111–125. DOI: 10.1007/s12567-016-0135-3.

Chase, M. W. (1998). *NIST-JANAF Thermochemical Tables*. American Institute of Physics, Berlin, 4th edition. ISBN: 9781563968310.

Christou, C. and Dadzie, S. K. (2018). On the numerical simulation of rarefied gas flows in microchannels. *Journal of Physics Communications*, 2(3):035002. DOI: 10.1088/2399-6528/aab066.

Chung, C. H., Kim, S. C., Stubbs, R. M., and De Witt, K. J. (1995). Low-density nozzle flow by the direct simulation Monte Carlo and continuum methods. *Journal of Propulsion and Power*, 11(1):64–70. DOI: 10.2514/3.23841.

Collins, F. C. (1955). Time lag in spontaneous nucleation due to non□steady state effects. *Zeitschrift fur Elektrochemie*. DOI: 10.1002/bbpc.19550590515.

Cooper, J. R. (2007). Revised Release on the IAPWS Industrial Formulation 1997 for the Thermodynamic Properties of Water and Steam. Technical report, International Association for the Properties of Water and Steam. IAPWS R7-97(2012).

Courtney, W. G. (1962a). Kinetics of condensation of water vapor. *The Journal of Chemical Physics*, 36(8):2018–2025. DOI: 10.1063/1.1732821.

Courtney, W. G. (1962b). Non-steady-state nucleation. *The Journal of Chemical Physics*, 36(8):2009–2017. DOI: 10.1063/1.1732820.

Crank, J. and Nicolson, P. (1996). A practical method for numerical evaluation of solutions of partial differential equations of the heat-conduction type. *Advances in Computational Mathematics*, 6(1):207–226. DOI: 10.1007/bf02127704.

Crifo, J. F. (1989). Inferences concerning water vapour viscosity and mean free path at low temperatures. *Astronomy and Astrophysics*, 223:365–368.

Dadzie, S. K. and Brenner, H. (2012). Predicting enhanced mass flow rates in gas microchannels using nonkinetic models. *Physical Review E*, 86(3). DOI: 10.1103/physreve.86.036318.

Darbandi, M. and Roohi, E. (2011). Study of subsonic–supersonic gas flow through micro/-nanoscalenozzles using unstructured DSMC solver. *Journal of Microfluidics and Nanofluidics*, 10(2):321–335. DOI: 10.1007/s10404-010-0671-7.

Daucik, K. (2011). Revised Release on the Pressure along the Melting and Sublimation Curves of Ordinary Water Substance. Technical report, International Association for the Properties of Water and Steam. IAPWS R14-08(2011).

Dillman, A. (1989). PhD thesis, Universitat Gottingen, Gottingen, Germany.

Dillmann, A. and Meier, G. E. A. (1991). A refined droplet approach to the problem of homogeneous nucleation from the vapor phase. *The Journal of Chemical Physics*, 94(5):3872–3884. DOI: 10.1063/1.460663.

Dongari, N., Zhang, Y., and Reese, J. M. (2011). Modeling of knudsen layer effects in micro/nanoscale gas flows. *Journal of Fluids Engineering*, 133(7). DOI: 10.1115/1.4004364.

Feder, J., Russell, K., Lothe, J., and Pound, G. (1966). Homogeneous nucleation and growth of droplets in vapours. *Advances in Physics*, 15(57):111–178.

Floriano, M. A. and Angell, C. A. (1990). Surface tension and molar surface free energy and entropy of water to -27.2.degree.c. *The Journal of Physical Chemistry*, 94(10):4199–4202. DOI: 10.1021/j100373a059.

Ford, I. J. (2004). Statistical mechanics of nucleation: A review. *Proceedings of the Institution of Mechanical Engineers, Part C: Journal of Mechanical Engineering Science*, 218(8):883–899. DOI: 10.1243/0954406041474183.

Fransen, M. A. L. J., Sachteleben, E., Hrubý, J., and Smeulders, D. M. J. (2014). On the growth of homogeneously nucleated water droplets in nitrogen: an experimental study. *Experiments in Fluids*, 55(7). DOI: 10.1007/s00348-014-1780-y.

Frenkel, J. (1955). *Kinetic Theory of Liquids*. Dover Publications.

Friedman, A. S. and Haar, L. (1954). High-speed machine computation of ideal gas thermodynamic functions. i. isotopic water molecules. *The Journal of Chemical Physics*, 22(12):2051–2058. DOI: 10.1063/1.1739991.

Ganani, C. (2019). Micronozzle performance: A numerical and experimental study. Master's thesis, Delft University of Technology, Delft, Netherlands.

Gerber, A. and Kermani, M. (2004). A pressure based eulerian–eulerian multi-phase model for non-equilibrium condensation in transonic steam flow. *International Journal of Heat and Mass Transfer*, 47(10-11):2217–2231. DOI: 10.1016/j.ijheatmasstransfer.2003.11.017.

Gerber, A. G. (2002). Two-phase eulerian/lagrangian model for nucleating steam flow. *Journal of Fluids Engineering*, 124(2):465–475. DOI: 10.1115/1.1454109.

Gerber, A. G. (2008). Inhomogeneous multifluid model for prediction of nonequilibrium phase transition and droplet dynamics. *Journal of Fluids Engineering*, 130(3). DOI: 10.1115/1.2844580.

Giorgi, M. G. D. and Fontanarosa, D. (2019a). A novel quasi-one-dimensional model for performance estimation of a vaporizing liquid microthruster. *Aerospace Science and Technology*, 84:1020–1034. DOI: 0.1016/j.ast.2018.11.039.

Giorgi, M. G. D. and Fontanarosa, D. (2019b). Numerical data concerning the performance estimation of a vaporizing liquid microthruster. *Data in Brief*, 22:307–311. DOI: 10.1016/j.dib.2018.12.013.

Giorgi, M. G. D., Fontanarosa, D., and Ficarella, A. (2018). Modeling viscous effects on boundary layer of rarefied gas flows inside micronozzles in the slip regime condition. In *73rd Conference of the Italian Thermal Machines Engineering Association (ATI 2018)*, volume 148, pages 838–845. Energy Procedia. DOI: 10.1115/IMECE2014-37612.

Gokcen, T. and Maccormack, R. (1989). Nonequilibrium effects for hypersonic transitional flows using continuum approach. In *27th Aerospace Sciences Meeting*. American Institute of Aeronautics and Astronautics. DOI: 10.2514/6.1987-1115.

Gokcen, T., Maccormack, R., and Chapman, D. (1987). Computational fluid dynamics near the continuum limit. In *8th Computational Fluid Dynamics Conference*. American Institute of Aeronautics and Astronautics. DOI: 10.2514/6.1987-1115.

Greenfield, B., Louisos, W. F., and Hitt, D. L. (2018). Impact of dilute multiphase flow in supersonic micronozzles. *Journal of Spacecraft and Rockets*, 56(1):190–199. DOI: 10.2514/1.A34215.

Greenshields, C. J. and Reese, J. M. (2012). Rarefied hypersonic flow simulations using the navier–stokes equations with non-equilibrium boundary conditions. *Progress in Aerospace Sciences*, 52:80–87. DOI: 10.1016/j.paerosci.2011.08.001.

Greenshields, C. J., Weller, H. G., Gasparini, L., and Reese, J. M. (2009). Implementation of semi-discrete, non-staggered central schemes in a colocated, polyhedral, finite volume framework, for high-speed viscous flows. *International Journal for Numerical Methods in Fluids*, pages n/a–n/a.

Guerrieri, D. C., Silva, M. A. C., Cervone, A., and Gill, E. (2017a). Selection and characterization of green propellants for micro-resistojets. *Journal of Heat Transfer*, 139(10):9 pages. DOI: 10.1115/1.4036619.

Guerrieri, D. C., Silva, M. A. C., van Zeijl, H., Cervone, A., and Gill, E. (2017b). Fabrication and characterization of low pressure micro-resistojets with integrated heater and temperature measurement. *Journal of Micromechanics and Microengineering*, 27(12):10 pages. DOI: 10.1115/1.4036619.

Gyarmathy, G. (1976). *Condensation in Flowing Steam*. Hemisphere Publishing Corporation - A von Karman Institute Book.

Gyarmathy, G. and Meyer, H. (1965). *Spontane Kondesation*. VDI-Verlag, Dusseldorf, Germany.

Hacker, P. T. (1951). Experimental values of surface tension of supercooled water. Technical report, Lewis Flight Propulsion Laboratory, National Advisory Committee for Aeronautics. Technical Note: 2510.

Hadjiconstantinou, N. G. (2003). Comment on cercignani's second-order slip coefficient. *Physics of Fluids*, 15(8):2352–2354. DOI: 10.1063/1.1587155.

Handle, P. H., Loerting, T., and Sciortino, F. (2017). Supercooled and glassy water: Metastable liquid(s), amorphous solid(s), and a no-man's land. *Proceedings of the National Academy of Sciences*, 114(51):13336–13344. DOI: 10.1073/pnas.1700103114.

Haris, P. A. and Ramesh, T. (2014). Numerical simulation of superheated steam flow in a micronozzle. *Applied Mechanics and Materials*, 592-594:1677–1681. DOI: 10.4028/www.scientific.net/AMM.592-594.1677.

Hasini, H., Zamri, M., and Abd., N. (2012). Numerical modeling of wet steam flow in steam turbine channel. In *Mechanical Engineering*. InTech. DOI: 10.5772/37394.

Hill, P. G. (1966). Condensation of water vapour during supersonic expansion in nozzles. *Journal of Fluid Mechanics*, 25(3):593–620. DOI: 10.1017/s0022112066000284.

Holten, V., Bertrand, C. E., Anisimov, M. A., and Sengers, J. V. (2012). Thermodynamics of supercooled water. *The Journal of Chemical Physics*, 136(9):094507. DOI: 10.1063/1.3690497.

Hric, V. and Halama, J. (2015). Numerical solution of transonic wet steam flow in blade-to-blade cascade with non-equilibrium condensation and real thermodynamics. *EPJ Web of Conferences*, 92:02025. DOI: 10.1051/epjconf/20159202025.

Hrubý, J., Vinš, V., Mareš, R., Hykl, J., and Kalová, J. (2014). Surface tension of supercooled water: No inflection point down to -25 °c. *The Journal of Physical Chemistry Letters*, 5(3):425–428. DOI: 10.1021/jz402571a.

Huang, L. and Young, J. B. (1996). An analytical solution for the wilson point in homogeneously nucleating flows. *Proceedings of the Royal Society of London. Series A: Mathematical, Physical and Engineering Sciences*, 452(1949):1459–1473. DOI: 10.1098/rspa.1996.0074.

Huber, M. L., Perkins, R. A., Laesecke, A., Friend, D. G., Sengers, J. V., Assael, M. J., Metaxa, I. N., Vogel, E., Mareš, R., and Miyagawa, K. (2009). New international formulation for the viscosity of H2O. *Journal of Physical and Chemical Reference Data*, 38(2):101–125. DOI: 10.1063/1.3088050.

Hughes, F. R., Starzmann, J., White, A. J., and Young, J. B. (2015). A comparison of modeling techniques for polydispersed droplet spectra in steam turbines. *Journal of Engineering for Gas Turbines and Power*, 138(4). DOI: 10.1115/1.4031389.

Ivanov, M., Markelov, G., and Gimelshein, S. (1998). Statistical simulation of reactive rarefied flows - numerical approach and applications. In *7th AIAA/ASME Joint Thermophysics and Heat Transfer Conference*. AIAA/ASME. DOI: 10.2514/6.1998-2669.

Ivanov, M., Markelov, G., Ketsdever, A., and Wadsworth, D. (1999). Numerical study of cold gas micronozzle flows. In *37th Aerospace Sciences Meeting and Exhibit*. American Institute of Aeronautics and Astronautics. DOI: 10.2514/6.1999-166.

Jansen, R., Gimelshein, S., Zeifman, M., and Wysong, I. (2009). First-principles Monte-Carlo simulation of homogeneous condensation in atomic and molecular plumes. In *Proceedings of the 41st AIAA Thermophysics Conference*, San Antonio, TX, USA. AIAA. Paper 2009-3745.

Johnson, A., Wright, J., Nakao, S., Merkle, C., and Moldover, M. (2000). The effect of vibrational relaxation on the discharge coefficient of critical flow venturis. *Flow Measurement and Instrumentation*, 11(4):315–327. DOI: 10.1016/s0955-5986(00)00004-2.

Johnson, A. N., Merkle, C. L., Moldover, M. R., and Wright, J. D. (2006). Relaxation effects in small critical nozzles. *Journal of Fluids Engineering*, 128(1):170–176. DOI: 10.1115/1.2137346.

Kantrowitz, A. (1951). Nucleation in very rapid vapor expansions. *The Journal of Chemical Physics*, 19(9):1097–1100. DOI: 10.1063/1.1748482.

Kashchiev, D. (1969). Solution of the non-steady state problem in nucleation kinetics. *Surface Science*, 14(1):209–220. DOI: 10.1016/0039-6028(69)90055-7.

Keenan, J. H., Keyes, F. G., Hill, P. G., and Moore, J. G. (1969). *Steam Tables: Thermodynamic Properties of Water, Including Vapor, Liquid and Solid Phases*. John Wiley and Sons, Inc, New York, NY, USA.

Kelton, K. F., Greer, A. L., and Thompson, C. V. (1983). Transient nucleation in condensed systems. *The Journal of Chemical Physics*, 79(12):6261–6276. DOI: 10.1063/1.445731.

Kim, Y. J., Wyslouzil, B. E., Wilemski, G., Wölk, J., and Strey, R. (2004). Isothermal nucleation rates in supersonic nozzles and the properties of small water clusters. *The Journal of Physical Chemistry A*, 108(20):4365–4377. DOI: 10.1021/jp037030j.

Kraposhin, M., Bovtrikova, A., and Strijhak, S. (2015). Adaptation of kurganov-tadmor numerical scheme for applying in combination with the PISO method in numerical simulation of flows in a wide range of mach numbers. *Procedia Computer Science*, 66:43–52. DOI: 10.1016/j.procs.2015.11.007.

Kudryavtsev, A., Shershnev, A., and Rybdylova, O. (2018). Numerical simulation of aerodynamic focusing of particles in supersonic micronozzles. *International Journal of Multiphase Flow*, 114:207–218. DOI: 10.1016/j.ijmultiphaseflow.2019.03.009.

Kundt, A. and Warburg, E. (1875). Ueber reibung und wärmeleitung verdünnter gase. *Annalen der Physik und Chemie*, 155(10):337; 525.

Kurganov, A. and Petrova, G. (2007). A second-order well-balanced positivity preserving central-upwind scheme for the saint-venant system. *Communications in Mathematical Sciences*, 5(1):133–160. DOI: 10.4310/cms.2007.v5.n1.a6.

Lai, D. S. and Kandambi, J. R. (1993). Generation of monodisperse droplets by spontaneous condensation of flow in nozzles. Technical report, Case Western Reserve University, Department of Mechanical and Aerospace Engineering. NASA Technical Report: CR-192356.

Lamanna, G. (2000). *On nucleation and droplet growth in condensing nozzle flows*. PhD thesis, TechnischeUniversiteit Eindhoven. DOI: 10.6100/IR539104.

Lambert, J. D. (1977). *Vibrational and Rotational Relaxation in Gases*. Oxford University Press.

Landolt, H. and Börnstein, R. (1960). *Zahlenwerte und Funktionen aus Physik, Chemie, Astronomie, Geophysik und Technik*, volume 2. Springer, Berlin.

Lemmer, K. (2017). Propulsion for cubesats. *Acta Astronautica*, 134:231–243. DOI: 10.1016/j.actaastro.2017.01.048.

Leomanni, M., Garulli, A., Giannitrapani, A., and Scortecci, F. (2017). Propulsion options for very low Earth orbit microsatellites. *Acta Astronautica*, 133:444–454. DOI: 10.1016/j.actaastro.2016.11.001.

Levchenko, I., Bazaka, K., Ding, Y., Raitses, Y., Mazouffre, S., Henning, T., Klar, P. J., Shinohara, S., Schein, J., Garrigues, L., Kim, M., Lev, D., Taccogna, F., Boswell, R. W., Charles, C., Koizumi, H., Shen, Y., Scharlemann, C., Keidar, M., and Xu, S. (2018). Space micropropulsion systems for Cubesats and small satellites: From proximate targets to furthermost frontiers. *Applied Physics Reviews*, 5(1):011104. DOI: 10.1063/1.5007734.

Lockerby, D. A., Reese, J. M., and Gallis, M. A. (2005). Capturing the knudsen layer in continuum-fluid models of nonequilibrium gas flows. *AIAA Journal*, 43(6):1391–1393. DOI: 10.2514/1.13530.

Lofthouse, A. J., Scalabrin, L. C., and Boyd, I. D. (2008). Velocity slip and temperature jump in hypersonic aerothermodynamics. *Journal of Thermophysics and Heat Transfer*, 22(1):38–49. DOI: 10.2514/1.31280.

Lopez-Echeverry, J. S., Reif-Acherman, S., and Araujo-Lopez, E. (2017). Peng-Robinson equation of state: 40 years through cubics. *Fluid Phase Equilibria*, 447:39–71. DOI: 10.1016/j.fluid.2017.05.007.

Louisos, W. F., Alexeenko, A. A., Hitt, D. L., and Zilic, A. (2008). Design considerations for supersonic micronozzles. *International Journal of Manufacturing Research*, 3(1):80–113. DOI: 10.1504/IJMR.2008.016453.

Louisos, W. F. and Hitt, D. L. (2008). Viscous effects on performance of two-dimensional supersonic linear micronozzles. *Journal of Spacecraft and Rockets*, 45(4):706–715. DOI: 10.2514/1.33434.

Louisos, W. F. and Hitt, D. L. (2010). Assessing the potential for condensation in supersonic micro nozzle flows. In *10th AIAA/ASME Joint Thermophysics and Heat Transfer Conference*, number AIAA 2010-5059. AIAA/ASME. DOI: 10.2514/6.2010-5059.

Louisos, W. F. and Hitt, D. L. (2011a). Analysis of transient flow in supersonic micronozzlers. *Journal of Spacecraft and Rockets*, 48(2):303–311. DOI: 10.2514/1.51027.

Louisos, W. F. and Hitt, D. L. (2011b). Analysis of transient flow in supersonic micronozzles. *Journal of Spacecraft and Rockets*, 48(2):303–311.

Louisos, W. F. and Hitt, D. L. (2012). Viscous effects on performance of three-dimensional supersonic micronozzles. *Journal of Spacecraft and Rockets*, 49(1):51–58. DOI: 10.2514/1.53026.

Louisos, W. F. and Hitt, D. L. (2014). Numerical studies of supersonic flow in bell-shaped micronozzles. *Journal of Spacecraft and Rockets*, 51(2):491–500. DOI: 10.2514/1.A32508.

Manka, A., Pathak, H., Tanimura, S., Wölk, J., Strey, R., and Wyslouzil, B. E. (2012). Freezing water in no-man's land. *Physical Chemistry Chemical Physics*, 14(13):4505. DOI: 10.1039/c2cp23116f.

Manka, A. A., Brus, D., Hyvärinen, A.-P., Lihavainen, H., Wölk, J., and Strey, R. (2010). Homogeneous water nucleation in a laminar flow diffusion chamber. *The Journal of Chemical Physics*, 132(24):244505. DOI: 10.1063/1.3427537.

Marcantonia, L. F. G., Tamagnoa, J. P., and Elaskar, S. A. (2012). High speed flow simulation using OpenFOAM. In *Mecanica Computacional*, volume 31, pages 2939–2959. Asociacion Argentina de Mecanical Computacional.

Marek, R. and Straub, J. (2001). Analysis of the evaporation coefficient and the condensation coefficient of water. *International Journal of Heat and Mass Transfer*, 44(1):39–53. DOI: 10.1016/s0017-9310(00)00086-7.

Maxwell, J. C. (1879). On stresses in rarefied gases arising from inequalities of temperature. *Philosophical Transactions of the Royal Society of London*, 170:231–256. DOI: 10.1098/rstl.1879.0067.

McBride, B. J., Gordon, S., and Reno, M. A. (1993). Coefficients for calculating thermodynamic and transport properties of individual species. Technical report, National Administration of Aeronautics and Astronautics (NASA), Mofett Field, CA, USA. NASA Technical Memorandum 4513.

Mccallum, M. and Hunt, R. (1999). The flow of wet steam in a one-dimensional nozzle. *International Journal for Numerical Methods in Engineering*, 44(12):1807–1821. DOI: 10.1002/(sici)1097-0207(19990430)44:12<1807::aid-nme563>3.0.co;2-z.

McDonald, J. E. (1962). Homogeneous nucleation of vapor condensation. i. thermodynamic aspects. *American Journal of Physics*, 30(12):870–877. DOI: 10.1119/1.1941841.

McDonald, J. E. (1963). Homogeneous nucleation of vapor condensation. II. kinetic aspects. *American Journal of Physics*, 31(1):31–41. DOI: 10.1119/1.1969234.

Mishima, O. (2010). Volume of supercooled water under pressure and the liquid-liquid critical point. *The Journal of Chemical Physics*, 133(14):144503. DOI: 10.1063/1.3487999.

Modesti, D. and Pirozzoli, S. (2017). A low-dissipative solver for turbulent compressible flows on unstructured meshes, with OpenFOAM implementation. *Computers & Fluids*, 152:14–23. DOI: 10.1016/j.compfluid.2017.04.012.

Mohamad, A. A. (2011). *Lattice Boltzmann Method*. Springer London.

Moore, M. J., Walters, P. T., Crane, R. I., and Davidson, B. J. (1973). Predicting the fog-drop size in wet-steam turbines. In *Proceedings of the Conference on Wet Steam 4*, Coventry, UK. Institution of Mechanical Engineers. Paper C37/73.

Moríñigo, J. A. and Hermida-Quesada, J. (2009). Simulation of high-speed flow in μ-rockets for space propulsion applications. In *IUTAM Symposium on Advances in Micro- and Nanofluidics*, pages 175–189. Springer Netherlands.

Morinigo, J. A. and Quesada, J. H. (2010). Solid–gas surface effect on the performance of a MEMS-class nozzle for micropropulsion. *Sensors and Actuators A: Physical*, 62(1):61–71. DOI: 10.1016/j.sna.2010.06.006.

Moses, C. A. and Stein, G. D. (1977). On the growth of steam droplets formed in a Laval nozzle using both static pressure and light scattering measurements. Technical report, Northwestern University, Department of Mechanical and Aerospace Engineering and Astronautical sciences. Report Nr: A034402.

Moses, C. A. and Stein, G. D. (1978a). On the growth of steam droplets formed in a laval nozzle using both static pressure and light scattering measurements. *Journal of Fluids Engineering*, 100(3):311–322. DOI: 10.1115/1.3448672.

Moses, C. A. and Stein, G. D. (1978b). On the growth of steam droplets formed in a laval nozzle using both static pressure and light scattering measurements. *Journal of Fluids Engineering*, 100(3):311–322. DOI: 10.1115/1.3448672.

Mukhopadhyay, A., Xantheas, S. S., and Saykally, R. J. (2018). The water dimer II: Theoretical investigations. *Chemical Physics Letters*, 700:163–175. DOI: 10.1016/j.cplett.2018.03.057.

Murphy, D. M. and Koop, T. (2005). Review of the vapour pressures of ice and supercooled water for atmospheric applications. *Quarterly Journal of the Royal Meteorological Society*, 131(608):1539–1565. DOI: 10.1256/qj.04.94.

Nikitin, E. E. and Troe, J. (2008). 70 years of Landau–Teller theory for collisional energy transfer. Semiclassical three-dimensional generalizations of the classical collinear model. *Phys. Chem. Chem. Phys.*, 10(11):1483–1501. DOI: 10.1039/b715095d.

Nishii, K., Koizumi, H., and Komurasaki, K. (2019). Experimental characterization of nozzle performance at low reynolds numbers for water resistojet thrusters. In *AIAA Propulsion and Energy 2019 Forum*. American Institute of Aeronautics and Astronautics. DOI: 10.2514/6.2019-4244.

Ostwald, W. (1897). Studien über die bildung und umwandlung fester körper. *Zeitschrift für Physikalische Chemie*, 22U(1).

Pearl, J. M., Louisos, W. F., and Hitt, D. L. (2014). Viscous effects on performance of linear plug micronozzles. In *Proceedings of the ASME 2014 International Mechanical Engineering Congress and Exposition*, pages 732–735. ASME. DOI: 10.1115/IMECE2014-37612.

Pearl, J. M., Louisos, W. F., and Hitt, D. L. (2017). Thrust calculation for low-reynolds-number micronozzles. *Journal of Spacecraft and Rockets*, 54(1):287–298. DOI: 10.2514/1.A33535.

Perrot, P. (1998). *A to Z of Thermodynamics*. Oxford University Press. ISBN: 9781305534094.

Petrova, T. (2014). Revised Release on Surface Tension of Ordinary Water Substance. Technical report, International Association for the Properties of Water and Steam. IAPWS R1-76(2014).

Probstein, R. F. (1951). Time lag in the self-nucleation of a supersaturated vapor. *The Journal of Chemical Physics*, 19(5):619–626. DOI: 10.1063/1.1748303.

Put, F. (2003). *Numerical Simulation of Condensation in Transonic Flows*. PhD thesis, University of Twente. ISBN90-365-1948-9.

Rebeiz, G. M. (2003). *RF MEMS: Theory, Design and Technology*. John Wiley & Sons, Inc.

Reisel, J. R. (2015). *Principles of Engineering Thermodynamics, SI Edition*. Cengage Learning. ISBN: 9781305534094.

Rothe, D. E. (1970). Electron beam measurements of gas densities and rotational temperatures in viscous nozzle flow. Technical report, National Administration of Aeronautics and Astronautics, New York, NY, USA. NASA-CR-116247.

Rothe, D. E. (1971). Electron-beam studies of viscous flow in supersonic nozzles. *AIAA Journal*, 9(5):804–811. DOI: 10.2514/3.6279.

San, O., Bayraktar, I., and Bayraktar, T. (2009). Size and expansion ratio analysis of micro nozzle gas flow. *International Communications in Heat and Mass Transfer*, 36(5):402–411. DOI: 10.1016/j.icheatmasstransfer.2009.01.021.

Schlichting, H. (1979). *Boundary Layer Theory*. McGraw-Hill, New York, NY, USA, 7th edition. Translated from the original ”Grenzschicht-Thoerie” in German.

Sharaf, M. A. and Dobbins, R. A. (1982). A comparison of measured nucleation rates with the predictions of several theories of homogeneous nucleation. *The Journal of Chemical Physics*, 77(3):1517–1526. DOI: 10.1063/1.443932.

Sharipov, F. (2011). Data on the velocity slip and temperature jump on a gas-solid interface. *Journal of Physical and Chemical Reference Data*, 40(2):023101. DOI: 10.1063/1.3580290.

Shen, C. (2005). *Rarefied Gas Dynamics: Fundamentals, Simulations and Micro-flows*. Springer, Berlin, Germany, 1st edition. ISBN: 3-540-23926-X.

Silva, E., Rojas-Cardenas, M., and Deschamps, C. J. (2016). Experimental analysis of velocity slip at the wall for gas flows of nitrogen, R134a, and R600a through a metallic microtube. *International Journal of Refrigeration*, 66:121–132. DOI: 10.1016/j.ijrefrig.2016.02.006.

Silva, M. A. C., Guerrieri, D. C., Cervone, A., and Gill, E. (2018a). A review of MEMS micropropulsion technologies for cubesats and pocketqubes. *Acta Astronautica*, 143:234–243. DOI: 10.1016/j.actaastro.2017.11.049.

Silva, M. A. C., Guerrieri, D. C., Cervone, A., and Gill, E. (2018b). A review of MEMS micropropulsion technologies for cubesats and pocketqubes. *Acta Astronautica*, 143:234–243. DOI: 10.1016/j.actaastro.2017.11.049.

Silva, M. A. C., Guerrieri, D. C., van Zeijl, H., Cervone, A., and Gill, E. (2017). Vaporizing liquid microthrusters with integrated heaters and temperature measurement. *Sensors and Actuators A: Physical*, 265:261–274. DOI: 10.1016/j.sna.2017.07.032.

Smoluchowski, R. M. (1898). Ueber wärmeleitung in verdünnten gasen. *Annalen der Physik*, 300(1):101–130. DOI: 10.1002/andp.18983000110.

Span, R., Lemmon, E. W., Jacobsen, R. T., Wagner, W., and Yokozeki, A. (2000). A reference equation of state for the thermodynamic properties of nitrogen for temperatures from 63.151 to 1000 k and pressures to 2200 MPa. *Journal of Physical and Chemical Reference Data*, 29(6):1361–1433.

Starzmann, J., Hughes, F. R., Schuster, S., White, A. J., Halama, J., Hric, V., Kolovratník, M., Lee, H., Sova, L., Šťastný, M., Grübel, M., Schatz, M., Vogt, D. M., Patel, Y., Patel, G., Turunen-Saaresti, T., Gribin, V., Tishchenko, V., Gavrilov, I., Kim, C., Baek, J., Wu, X., Yang, J., Dykas, S., Wróblewski, W., Yamamoto, S., Feng, Z., and Li, L. (2018). Results of the international wet steam modeling project. *Proceedings of the Institution of Mechanical Engineers, Part A: Journal of Power and Energy*, 232(5):550–570. DOI: 10.1177/0957650918758779.

Stein, W. B. and Alexeenko, A. A. (2011). Plug-annular micronozzles: A new prospect for microthrusters. *Journal of Propulsion and Power*, 27(6):1259–1265. DOI: 10.2514/1.B34043.

Strey, R., Wagner, P. E., and Viisanen, Y. (1994). The problem of measuring homogeneous nucleation rates and the molecular contents of nuclei: Progress in the form of nucleation pulse measurements. *The Journal of Physical Chemistry*, 98(32):7748–7758. DOI: 10.1021/j100083a003.

Strobach, P. (2010). The fast quartic solver. *Journal of Computational and Applied Mathematics*, 234(10):3007–3024. DOI: 10.1016/j.cam.2010.04.015.

Sutherland, W. (1893). The viscosity of gases and molecular force. *Philosophical Magasine Series 5*, 36(23):507–531. DOI: 10.1080/14786449308620508.

Sutton, G. P. and Biblarz, O. (2017). *Rocket Propulsion Elements*. John Wiley & Sons, Hoboken, NJ, USA, 9th edition. ISBN: 9781118753651.

Tang, Y., Sandoughsaz, A., Owen, K. J., and Najafi, K. (2018). Ultra deep reactive ion etching of high aspect-ratio and thick silicon using a ramped-parameter process. *Journal of Microelectromechanical Systems*, 27(4):686–697.

Tanimura, S., Wyslouzil, B. E., and Wilemski, G. (2010). CH3CH2OD/D2O binary condensation in a supersonic laval nozzle: Presence of small clusters inferred from a macroscopic energy balance. *The Journal of Chemical Physics*, 132(14):144301. DOI: 10.1063/1.3360304.

Torre, F. L., Kenjeres, S., Kleijn, C. R., and Moerel, J. L. P. A. (2010). Effects of wavy surface roughness on the performance of micronozzles. *Journal of Propulsion and Power*, 26(4):655–662. DOI: 10.2514/1.44828.

Torre, F. L., Kenjereš, S., Moerel, J. L., and Kleijn, C. R. (2011). Hybrid simulations of rarefied supersonic gas flows in micro-nozzles. *Computers and Fluids*, 49(1):321–322. DOI: 10.1016/j.compfluid.2011.06.008.

Tropea, C., Yarin, A. L., and Foss, J. F. (2007). Microfluidics: The no-slip boundary condition. In of Experimental Fluid Mechanics, H., editor, *Handbook of Experimental Fluid Mechanics*, Springer Handbooks, chapter 19, pages 1219–1239. Springer, Berlin, Germany. DOI: 10.1007/978-3-540-30299-5.

Tsien, H. S. (1946). Superaerodynamics, mechanics of rarefied gases. *Journal of the Aeronautical Sciences*, 13(12):653–664. DOI: 10.2514/8.11476.

van Albada, G. D., van Leer, B., and Roberts, W. W. (1997). A comparative study of computational methods in cosmic gas dynamics. In *Upwind and High-Resolution Schemes*, pages 95–103. Springer Berlin Heidelberg.

van Leer, B. (1979). Towards the ultimate conservative difference scheme. v. a second-order sequel to godunov's method. *Journal of Computational Physics*, 32(1):101–136. DOI: 10.1016/0021-9991(79)90145-1.

van Wees, T., Hanselaar, C., Jansen, E., Cervone, A., Zandbergen, B., and van Zeijl, H. (2016). Design, fabrication, testing and modeling of a vaporizing liquid micro-propulsion system. In *ESA Space Propulsion 2016 Conference*, number SPC2016_3124914. European Space Agency.

Versteeg, H. K. and Malalasekera, W. (2007). *An Introduction to Computational Fluid Dynamics - The Finite Volume Method*. Pearson Education Limited, Essex, England, 2nd edition. ISBN: 978-0-13-127498-3.

Viisanen, Y., Strey, R., and Reiss, H. (1993). Homogeneous nucleation rates for water. *The Journal of Chemical Physics*, 99(6):4680–4692. DOI: 10.1063/1.466066.

Vincenti, W. G. and Kruger, C. H. (1967). *Introduction to Physical Gas Dynamics*. John Wiley & Sons, Inc, New York, USA, 1st edition. ISBN: 0-88275-309-6.

Volmer, M. (1939). Kinetics of Phase Formation. Technical report, Technishe Hogesschule Berlin. Translated by the US Intelligence Department, AMC, from the original in German: ”Kinetik der Phasenbildung”.

Vukalovitch, M. P. (1958). *Thermodynamic Properties of Water and Steam*. State publishing-house of scientific technical literature concerning mechanical engineering ”MASHGIS” and Nationally owned publishing house ”Veb Verlag Technic”, Moscow and Berlin.

Wagner, W., Cooper, J. R., Dittmann, A., Kijima, J., Kretzschmar, H.-J., Kruse, A., Mares˘, R., Oguchi, K., Sato, H., Sto¨cker, I., S˘ifner, O., Takaishi, Y., Tanishita, I., Tru¨benbach, J., and Willkommen, T. (2000). The IAPWS industrial formulation 1997 for the thermodynamic properties of water and steam. *Journal of Engineering for Gas Turbines and Power*, 122(1):150–184. DOI: 10.1115/1.483186.

Wagner, W. and Pruss, A. (1993). International equations for the saturation properties of ordinary water substance. revised according to the international temperature scale of 1990. addendum to j. phys. chem. ref. data 16, 893 (1987). *Journal of Physical and Chemical Reference Data*, 22(3):783–787.

Wagner, W. and Pruß, A. (2002). The IAPWS formulation 1995 for the thermodynamic properties of ordinary water substance for general and scientific use. *Journal of Physical and Chemical Reference Data*, 31(2):387–535. DOI: 10.1063/1.1461829.

Wakeshima, H. (1954). Time lag in the self-nucleation. *The Journal of Chemical Physics*, 22(9):1614–1615. DOI: 10.1063/1.1740475.

Warming, R. F. and Beam, R. M. (1976). Upwind second-order difference schemes and applications in aerodynamic flows. *AIAA Journal*, 14(9):1241–1249. DOI: 10.2514/3.61457.

Wegener, P. and Mack, L. (1958). Condensation in supersonic and hypersonic wind tunnels. In *Advances in Applied Mechanics*, pages 307–447. Elsevier. DOI: 10.1016/s0065-2156(08)70022-x.

Wegener, P. P. (1954). Water vapor condensation process in supersonic nozzles. *Journal of Applied Physics*, 25(12):1485–1491. DOI: 10.1063/1.1702369.

Wegener, P. P. (1975). Nonequilibrium flow with condensation. *Acta Mechanica*, 21(1-2):65–91. DOI: 10.1007/bf01172829.

Wegener, P. P. and Wu, B. J. (1977). Gasdynamics and homogeneous nucleation. *Advances in Colloid and Interface Science*, 7(1):325–417. DOI: 10.1016/0001-8686(77)85008-2.

White, A. J. and Young, J. B. (1993). Time-marching method for the prediction of two-dimensional, unsteady flows of condensing steam. *Journal of Propulsion and Power*, 9(4):579–587. DOI: 10.2514/3.23661.

Wölk, J. and Strey, R. (2001). Homogeneous nucleation of H2O and D2O in comparison: the isotope effect†. *The Journal of Physical Chemistry B*, 105(47):11683–11701. DOI: 10.1021/jp0115805.

Wyslouzil, B. E. and Wölk, J. (2016). Overview: Homogeneous nucleation from the vapor phase—the experimental science. *The Journal of Chemical Physics*, 145(21):211702. DOI: 10.1063/1.4962283.

Xu, K., He, X., and Cai, C. (2008). Multiple temperature kinetic model and gas-kinetic method for hypersonic non-equilibrium flow computations. *Journal of Computational Physics*, 227(14):6779–6794. DOI: 10.1016/j.jcp.2008.03.035.

Young, J. B. (1982). Spontaneous condensation of steam in supersonic nozzles. *Physicochemical Hydrodynamics (PCH)*, (3):57–82. ISSN 0191-9059.

Young, J. B. (1988). An equation of state for steam for turbomachinery and other flow calculations. *Journal of Engineering for Gas Turbines and Power*, 110(1):1–7. DOI: 10.1115/1.3240080.

Young, J. B. (1992). Two-dimensional, nonequilibrium, wet-steam calculations for nozzles and turbine cascades. *Journal of Turbomachinery*, 114(3):569–579. DOI: 10.1115/1.2929181.

Zhao, W., Chen, W., and Agarwal, R. K. (2014). Formulation of a new set of simplified conventional burnett equations for computation of rarefied hypersonic flows. *Aerospace Science and Technology*, 38:64–75. DOI: 10.1016/j.ast.2014.07.014.

Zhong, J., Zeifman, M. I., Levin, D. A., and Gimelshein, S. F. (2005). Direct Simulation Monte Carlo Modeling of Homogenous Condensation in Supersonic Plumes. *AIAA Journal*, 43(8):1784–1796. DOI: 10.2514/1.9566.